

TECHNISCHE UNIVERSITÄT MÜNCHEN

TUM School of Engineering and Design

Computational Multiphysics Modeling with Smoothed Particle Hydrodynamics and Finite Elements

Sebastian Leonhard Fuchs

Vollständiger Abdruck der von der TUM School of Engineering and Design der Technischen Universität München zur Erlangung des akademischen Grades eines

Doktors der Ingenieurwissenschaften (Dr.-Ing.)

genehmigten Dissertation.

Vorsitzender: Prof. Dr. techn. Peter Mayr

Prüfer der Dissertation:

1. Prof. Dr.-Ing. Christian J. Cyron
2. Assoc. Prof. Alessio Gizzi, Ph.D.
3. Prof. Dr.-Ing. Wolfgang A. Wall

Die Dissertation wurde am 21.06.2021 bei der Technischen Universität München eingereicht und durch die Fakultät für Maschinenwesen am 28.09.2021 angenommen.

Abstract

For decades, limited computing power has been a major bottleneck for large scale in-silico studies of complex multiphysics problems. Today, advanced processor architectures provide the required computational resources to enable sophisticated analyses of such problems. Nevertheless, the development of efficient computational approaches that are required to model relevant physical phenomena, remains challenging and far from trivial. This is aggravated by the fact that a variety of multiphysics applications in science and engineering, in particular, in some areas of biomechanics, are governed by complex physical phenomena, such as multiphase flow, dynamic phase transitions, geometrically complex and continually changing interface topologies, and fluid-structure interaction (FSI) problems.

This thesis presents accurate, robust, and computationally efficient numerical formulations for multiphysics problems of the aforementioned kind using smoothed particle hydrodynamics (SPH) and the finite element method (FEM) as discretization schemes. SPH in particular, as a mesh-free scheme and due to its Lagrangian nature, is well suited for applications involving multiphase flow, phase transitions, and complex interface topologies.

The major scientific contributions of this thesis can be summarized as follows: A high-performance computational framework is developed that enables large scale analyses of multiphysics applications involving SPH and the FEM. This computational framework establishes the basis for two methodological novelties. First, a numerical formulation for the solution of FSI problems in which the fluid domain is spatially discretized using SPH and the structural domain using the FEM is introduced. The proposed formulation enables an accurate representation of fluid quantities nearby strongly curved and deformable interface topologies. Second, a numerical formulation for highly dynamic motions of arbitrarily-shaped rigid bodies embedded in a multiphase flow is presented. Herein, SPH is applied for the spatial discretization of all involved domains. Thus, rigid bodies are resolved as clusters of particles. Thermal conduction and reversible phase transitions between fluid and solid rigid bodies is considered.

Altogether, both formulations present powerful tools for advanced studies of multiphysics problems. Of its numerous possible applications, mesoscale melt pool modeling in metal powder bed fusion additive manufacturing (PBFAM) processes and the digestion of food in the human stomach are chosen as exemplary problems in this thesis. However, the groundwork for more sophisticated studies on these complex phenomena is laid and the transfer of the presented methods to other highly relevant multiphysics applications is possible.

Zusammenfassung

Begrenzte Rechenleistung stellte jahrzehntlang einen wesentlichen Engpass für detaillierte in-silico Studien komplexer Multiphysik-Probleme dar. Heute sind mit modernen Prozessorarchitekturen die erforderlichen Ressourcen vorhanden, um anspruchsvollere Analysen solcher Probleme zu ermöglichen. Dennoch bleibt die Entwicklung effizienter numerischer Methoden, die zur Modellierung der relevanten physikalischen Phänomene erforderlich sind, eine große Herausforderung und ist alles andere als trivial. Dies wird erschwert durch die Tatsache, dass eine Vielzahl von Multiphysik-Anwendungen in Wissenschaft und Technik, insbesondere in einigen Bereichen der Biomechanik, von komplexen physikalischen Phänomenen wie Mehrphasenströmungen, dynamischen Phasenübergängen, geometrisch komplexen Grenzflächentopologien und Fluid-Struktur-Interaktionsproblemen (FSI) geprägt sind.

In dieser Arbeit werden robuste und effiziente numerische Methoden für die Simulation von Multiphysik-Problemen der oben genannten Art unter Verwendung von Smoothed Particle Hydrodynamics (SPH) und der Methode der Finiten Elemente (FEM) entwickelt. Insbesondere SPH ist als netzfreie Methode und aufgrund seiner Lagrangeschen Betrachtungsweise hervorragend geeignet für Anwendungen mit Mehrphasenströmungen, Phasenübergängen und komplexen Grenzflächentopologien.

Die wichtigsten wissenschaftlichen Beiträge dieser Arbeit lassen sich wie folgt zusammenfassen: Es wurde eine hocheffiziente Simulationsumgebung unter Einbeziehung von SPH und FEM entwickelt, welche aufwändige Studien von Multiphysik-Anwendungen ermöglicht. Diese Simulationsumgebung bildet die Grundlage für zwei methodische Neuerungen. Erstens wird eine numerische Formulierung für die Lösung von FSI-Problemen eingeführt, bei der die Fluid-domäne mit SPH und die Strukturdomäne mit der FEM räumlich diskretisiert wird. Die vorgeschlagene Formulierung ermöglicht eine genaue Darstellung von Fluidgrößen in der Nähe stark gekrümmter und deformierbarer Grenzflächen. Zweitens wird eine numerische Formulierung zur Simulation der Bewegung von beliebig geformten Starrkörpern in einer Mehrphasenströmung vorgestellt, wobei SPH zur räumlichen Diskretisierung aller beteiligten Domänen verwendet wird. Folglich sind die Starrkörper als Verbund von Partikeln voll aufgelöst. Außerdem werden Wärmeleitung und reversible Phasenübergänge in Form von Schmelzen und Erstarren berücksichtigt.

Insgesamt stellen beide Formulierungen wirkungsvolle Werkzeuge für fortgeschrittene Studien von Multiphysik-Problemen dar. Von den zahlreichen möglichen Anwendungsfeldern werden in dieser Arbeit die Modellierung des Schmelzbades in der additiven pulverbettbasierten Fertigung sowie die Modellierung der Verdauung im menschlichen Magen als beispielhafte Probleme betrachtet. Die Grundlage für anspruchsvollere Studien zu diesen komplexen Phänomenen ist damit gelegt. Darüber hinaus ist die Anwendung der vorgestellten Methoden auf andere hochrelevante Multiphysik-Anwendungen möglich.

Danksagung

Die vorliegende Dissertation ist im Rahmen meiner Tätigkeit als wissenschaftlicher Mitarbeiter am Lehrstuhl für Numerische Mechanik der Technischen Universität München in den Jahren von 2016 bis 2021 entstanden. Dieser Zeitraum war für mich geprägt von den mit der Promotion verbundenen Anstrengungen und Entbehrungen. Dieser Zeitraum war aber vor allem auch reich an schönen Momenten, die ich gemeinsam mit den Personen, die mich umgeben haben, erleben durfte. Daher ist es mir wichtig, all diesen Personen meinen herzlichen Dank auszusprechen und ihren Anteil am Gelingen dieser Arbeit zu würdigen.

Allen voran möchte ich mich bei meinem Doktorvater Prof. Dr.-Ing. Christian J. Cyron für das in mich gesetzte Vertrauen, die mir gewährten Freiheiten und die wissenschaftliche Betreuung bedanken. An meinen Zweitprüfer Assoc. Prof. Alessio Gizzi, Ph.D., vom Università Campus Bio-Medico di Roma möchte ich für die fachliche Kooperation im Magen-Projekt die Worte *grazie mille* richten. Ferner danke ich meinem Dritprüfer Prof. Dr.-Ing. Wolfgang A. Wall für die erfahrene Unterstützung in allen wissenschaftlichen Belangen sowie die Möglichkeit, auch nach dem Ruf meines Doktorvaters an die Technische Universität Hamburg, als Teil der verbliebenen Emmy Noether-Nachwuchsgruppe an seinem Lehrstuhl forschen zu können. Ich bedanke mich bei Prof. Dr. techn. Peter Mayr für die Übernahme des Vorsitzes der Prüfungskommission sowie bei Frau Renata Nagl für ihre Unterstützung in allen organisatorischen Belangen.

Ein großer Dank gebührt all jenen Kollegen am Lehrstuhl, die sich mit Partikelmethode beschäftigt haben. Eine besondere Erwähnung verdienen hierbei Georg Hammerl und Niklas Fehn für geleistete wissenschaftliche Vorarbeit sowie Jonas Eichinger und Martin Kronbichler für geführte Diskussionen über effiziente Datenstrukturen und parallele Programmierkonzepte. Einen wesentlichen Anteil am Gelingen meiner Dissertation hatte Christoph Meier. Aus anfangs wöchentlichen transatlantischen Gesprächen hat sich im Laufe der Zeit eine fruchtbare Zusammenarbeit am Lehrstuhl entwickelt. Seine Begeisterung für die Wissenschaft wirkt ansteckend und lässt einen bei fachlichen Problemen stets neuen Mut schöpfen. Im Magen-Projekt habe ich die vertrauensvolle Zusammenarbeit mit meinem Kollegen Sebastian Brandstätter als äußerst bereichernd in Erinnerung. Hier sind zwei verschiedene Charaktere aufeinandergetroffen, die im Laufe der Zeit die Stärken des Anderen zu schätzen gelernt haben. Des Weiteren sei all meinen Kollegen im Admin-Team gedankt für den kollektiven Einsatz bei diversen Netzwerk- oder Rechnerproblemen. Außerdem richtet sich mein Dank an alle Studierenden mit denen ich in den vergangenen Jahren in verschiedensten Projekten zusammengearbeitet habe.

Neben der großartigen Arbeitsatmosphäre am Lehrstuhl schätze ich aber vor allem den sozialen Zusammenhalt unter den Kollegen. Im Laufe der Jahre haben sich so bei verschiedensten Aktivitäten wahre Freundschaften entwickelt. Die allmorgendliche Kaffeetunde hat immer für einen unterhaltsamen Start in den Tag gesorgt und bei diversen Feierabendbieren wurden mehr oder weniger philosophische Fragen diskutiert. Auch der Sport ist am Lehrstuhl nicht zu kurz gekommen. Allen Mitgliedern des LNM Pro Racing Teams danke ich für unzählige Speichersee-Klassiker, selbst erlittene oder provozierte Hungerraste, die Begleitung ins nächste Krankenhaus, sowie gemeinsam bestrittene Arber, Rosenheimer und Öztaler Radmarathons. Den Boulderern sei gedankt für gemeinsame Stunden in staubigen Hallen und motivierende Zusprüche im Antlitz des bevorstehenden Topgriffes oder Sturzes. Den Fußballern am Lehrstuhl bleiben wohl nur meine verpassten Torchancen und Tritte an Sprunggelenke in Erinnerung. Besonders bedanken möchte ich mich bei meinem langjährigen Bürokollegen Johannes Kremheller sowie bei den

Kollegen Sebastian Brandstätter, Jonas Eichinger, Carolin Geitner und Christoph Schmidt. Vielen Dank für die gemeinsame Zeit, für fachliche und oft auch nicht-fachliche Gespräche, und noch so vieles mehr.

Zu guter Letzt richtet sich mein Dank von ganzem Herzen an meine Freunde und vor allem an meine Familie. Ihr habt mich immer in meinem Handeln bekräftigt, mir das Vertrauen geschenkt und den nötigen Rückhalt gegeben.

Rosenheim, im Dezember 2021

Sebastian L. Fuchs

Contents

1	Introduction	1
1.1	Research objectives	1
1.2	Computational methods	4
1.3	Contributions and accomplishments	5
1.4	Outline	6
2	Governing equations and numerical methods	9
2.1	Instationary Navier-Stokes equations for fluid flow	9
2.2	Spatial discretization via smoothed particle hydrodynamics	10
2.2.1	Approximation of field quantities via a smoothing kernel	10
2.2.2	Discretization of the domain with particles	11
2.2.3	Consistency properties of standard smoothing kernels	12
2.2.4	Uniform initial particle spacing in the domain	13
2.3	Modeling fluid flow via weakly compressible smoothed particle hydrodynamics	14
2.3.1	Smoothed density field via summation	14
2.3.2	Discretization of the momentum equation	14
2.3.3	Equation of state	15
2.3.4	Boundary conditions	15
2.3.5	Explicit velocity-Verlet time integration scheme	17
2.4	Nonlinear initial boundary value problem of structural mechanics	17
2.5	Modeling deformable structures via the finite element method	18
2.5.1	Principle of virtual work	18
2.5.2	Discretization in space and time	19
2.6	Parallel computational framework	20
2.6.1	Spatial decomposition of the computational domain	20
2.6.2	Surface coupling of the particle field with a volume mesh	22
2.7	Numerical examples of fluid flow problems	23
2.7.1	Poiseuille and Couette flow	24
2.7.2	Shear-driven cavity flow	25
2.7.3	Three-dimensional Rayleigh-Taylor instability	26
3	Summary of publications	29
3.1	Paper A	30
3.2	Paper B	32
4	Discussion and conclusion	35
	Bibliography	48

A Full texts of publications **49**

A.1 Paper A 51

A.2 Paper B 83

1 Introduction

A variety of applications in science and engineering, in particular, in some areas of biomechanics, are characterized by multiphase flow and dynamic phase transitions, or by fluid-structure interaction phenomena subject to large interface deformations, and may thus be classified as so-called multiphysics problems. While nowadays numerical simulations are considered as a common tool to investigate standard engineering problems, the development of advanced computational approaches to model the aforementioned class of multiphysics problems is still challenging and far from trivial. One reason for this may certainly result from the fact, that "a multiphysics system consists of more than one component governed by its own principle(s) for evolution or equilibrium, typically conservation or constitutive laws" [1]. Most commonly, pursuing a bottom-up approach, this requires combining individual components to form the big picture of a comprehensive computational multiphysics model. For a considerable time, computational capabilities have been the limiting factor for studies of multiphysics problems at a large scale. However, recently advanced processor architectures with increased computing power are available, and thus, open up new possibilities and pave the way for more sophisticated studies of multiphysics problems.

Against this background, this cumulative thesis is devoted to the development of novel computational approaches for multiphysics applications in the fields of engineering and biomechanics. To this end, this chapter presents two research projects of the author and colleagues in the fields of engineering and biomechanics, defines the relevant physical phenomena to be considered in a computational model, and motivates the development of novel computational approaches to investigate this class of multiphysics problems. In addition, an overview of the author's contributions and accomplishments within the presented research projects is given and the publications which form the core of this cumulative thesis are stated. Finally, this chapter concludes with a short outline of the remainder of this cumulative thesis.

1.1 Research objectives

In the following, two research projects of the author and colleagues are briefly presented. The first research project resides in the field of biomechanics and aims at the development of a computational multiphysics model of the human stomach. The second research project in the field of engineering is, among others, concerned with the development of a mesoscale melt pool model in metal powder bed fusion additive manufacturing (PBFAM) processes.

Multiphysics modeling of the human stomach

Mathematical and computational modeling of the human stomach constitutes an emerging field of biomechanics that requires to address several complex phenomena as, e.g., gastric electro-

physiology, solid mechanics of the gastric wall, and fluid mechanics of the digesta. This trend is reflected by the increasing amount of literature recently published in this field. However, for the sake of brevity, it is abstained from giving a detailed literature review herein, referring the reader to [2] instead. The ultimate goal of this research project is the development of a computational multiphysics model of the human stomach to

- allow for in-silico studies of the complex interplay between the different physiological parameters governing the mechanics of the stomach and the digestion of food, and
- examine the relation between gastric mechanics and gastric disorders and pathologies.

Modeling of biological systems naturally requires deep knowledge and understanding of its essential structure and functioning. To this end, a brief introduction into the anatomy and the physiology of the human stomach is given in the following, with the purpose to identify the key components of a comprehensive multiphysics model.

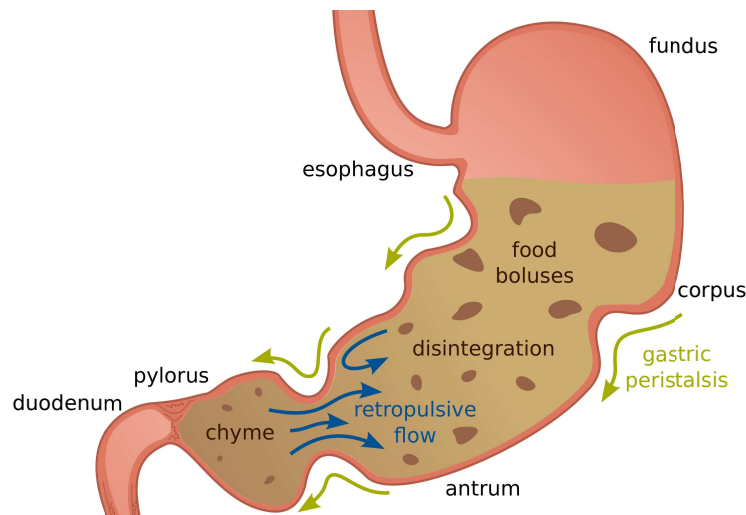


Figure 1.1: Schematic representation of a human stomach with gastric peristalsis and retropulsive flow mixing and grinding the digesta into chyme.

The human stomach is a J-shaped muscular bag, that constitutes a vital organ of the gastrointestinal tract, and mainly consists of three anatomical regions, namely the fundus, the corpus, and the antrum. The physiology of the human stomach can be categorized into gastric motility patterns, that are gastric accommodation, gastric peristalsis, and gastric emptying. After ingestion of food through the mouth and the esophagus, the stomach stores the digesta, that is diluted with gastric juice, in the fundus. To increase the storage capacity while maintaining a low intragastric pressure [3], the tension of smooth muscle in the gastric wall of the fundus decreases, i.e., the fundus relaxes. This is also called gastric accommodation and results in an increase in volume of up to 1500 mL in the fed state, compared to the initial 25 mL of volume in the fasted state [4]. The digesta in the lumen of the postprandial stomach is characterized by a multiphasic nature consisting of gastric juice, chyme, and solid food boluses [2]. During gastric peristalsis, larger food boluses are mechanically as well as chemically disintegrated into chyme upon absorption of gastric juice [5]. Gastric peristalsis is characterized by so-called antral contraction waves

(ACWs), i.e., ring-shaped contraction and relaxation of smooth muscle in the gastric wall controlled by electric slow waves. The ACWs are initiated at the pacemaker region and propagate along the greater curvature towards the pylorus [6], while mixing and grinding the digesta in the corpus and antrum. At low viscosity of the digesta, that is after dilution with gastric juice, typical intragastric fluid motion can be observed in the form of retroulsive flow through the circular constrictions of the gastric wall caused by the ACWs [7–9]. For the purposes of illustration, a schematic representation of a human stomach with gastric peristalsis and resulting retroulsive flow that are mixing and grinding the digesta into chyme, is given in Figure 1.1. Finally, during gastric emptying the chyme is pushed from the antrum through the pylorus into the duodenum and a normal smooth muscle tension is restored in the gastric wall of the fundus [10].

In conclusion, recapitulating the anatomy and physiology of the human stomach with a focus on gastric motility, allows to define the following key components [2] of a computational multi-physics model of the human stomach: gastric electrophysiology, solid mechanics of the gastric wall, and fluid mechanics of the digesta. Coupling all these individual components following a bottom-up approach to form the big picture of a comprehensive multiphysics model of the human stomach still remains one of the greatest challenges in the field and is part of ongoing research.

Mesoscale melt pool modeling in metal PBFAM processes

In metal PBFAM processes, such as, e.g., selective laser melting (SLM) or electron beam melting (EBM), a laser or electron beam is utilized as a local heat source to melt and fuse a granular metal powder, layer per layer, to finally form a complex structural part. In consequence, metal PBFAM opens up entirely new opportunities in product design and manufacturing, e.g., in medical technology or aerospace engineering [11]. However, the overall metal PBFAM process is affected by several physical phenomena on different length scales, and due to this complexity still not completely understood. In addition, high-production costs as well as low production rates characterize the metal PBFAM process. This is where physic-based modeling and predictive simulation of metal PBFAM processes has the potential

- to shed light on governing process physics, e.g., melt pool thermo-hydrodynamics, and
- to give insights on optimal processing conditions, e.g., to maintain process stability and to prevent the creation of defects.

Thus, it can help to improve processing hardware, strategies, and materials [12]. An overview of several recent modeling approaches of the powder bed, the melt pool, and the solidified structural part on different length scales while considering important physical phenomena in metal PBFAM is given in [12]. In the following, the focus is set on mesoscale melt pool modeling in metal PBFAM processes. For the sake of brevity, no detailed literature review is provided herein, instead the interested reader is referred to [11–13].

For the purposes of illustration, Figure 1.2 gives a schematic representation of a melt pool in a metal PBFAM process putting the spotlight on several relevant physical phenomena, which are briefly described in the following. A laser beam moves over a thin layer of granular metal powder and heats up metal powder particles located beneath. Once the melting temperature at the surface of the metal powder particles is exceeded, localized melting into a liquid metal phase

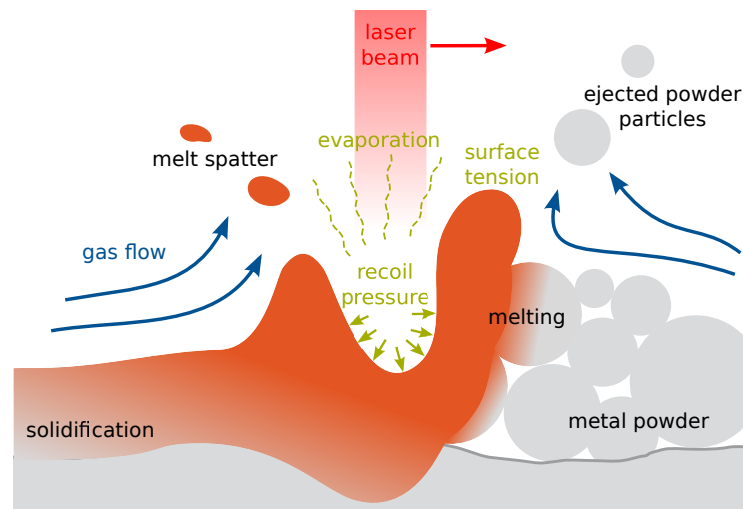


Figure 1.2: Schematic representation of a melt pool in a metal PBFAM process with melting of granular metal powder to liquid metal due to a laser beam heat source, evaporation-induced effects, temperature-induced surface tension forces, and solidification (adapted from [11]).

occurs along with the formation of a so-called melt pool. Due to the movement of the laser beam a (continuous) melt track lags behind the position of the laser beam until the liquid metal cools down and resolidifies. Altogether, melt pool thermo-hydrodynamics is dominated by strong temperature-dependent surface tension, wetting, and capillary forces, that dynamically reshape the formed melt pool [14, 15]. Besides, evaporation of melt takes place in case the boiling temperature is exceeded [16]. Additionally, this induces a gas flow and high recoil pressure forces further influencing melt pool thermo-hydrodynamics. Recoil pressure forces may evoke the formation of so-called keyholes and thus, in combination with gas flow eventually lead to spatter of melt drops or metal powder grains being ejected away [11, 17, 18]. Naturally, the aforementioned effects influence the process stability in metal PBFAM and (negatively) affect the quality of the solidified structural part.

In sum, mesoscale melt pool modeling in metal PBFAM processes requires to consider multiple phases (i.e., a solid metal, a liquid metal, and a gaseous phase), reversible phase transitions in the form of melting and solidification, temperature-induced surface tension and wetting forces as well as capillary forces, and evaporation-induced recoil pressure forces.

1.2 Computational methods

In conclusion, the aforementioned multiphysics applications, that are, the development of a computational multiphysics model of the human stomach, and the development of a mesoscale melt pool model in metal PBFAM processes, are, among others, characterized by multiphase flow, (reversible) phase transitions, and geometrically complex and continually changing interface topologies. In addition, fluid-structure interaction (FSI) phenomena, e.g., subject to large interface deformations, often play an essential role. However, these phenomena can not be captured sufficiently by the most commonly applied mesh- or grid-based approaches without substantial methodological and computational efforts. By contrast, the method of smoothed particle

hydrodynamics (SPH) offers some promising advantages. SPH is a mesh-free discretization scheme that was independently introduced by Gingold and Monaghan [19] and Lucy [20] in the year 1977, initially to study astrophysical problems. However, since then SPH has gained increasing importance in other fields of computational fluid dynamics (CFD), and also, e.g., in computational solid dynamics (CSD). Due to its Lagrangian nature and mesh-free character, SPH is particularly suitable for multiphysics problems involving multiphase flow, dynamic phase transitions, and continually changing interface topologies subject to large deformations, and, in consequence, very appropriate for a wide range of applications in both engineering and biomechanics. For these reasons, SPH is selected as discretization scheme for the fluid and undeformable solid phases. In contrast, the deformable structures are, as most commonly done in engineering, discretized using the finite element method (FEM), thereby profiting from the method's advantages in this use case, e.g., high accuracy compared to other methods, straightforward application of boundary conditions, etc. To this end, a robust and efficient coupling scheme for SPH and the FEM is required. To summarize, this thesis proposes novel computational approaches for multiphysics applications in the fields of engineering and biomechanics using SPH and the FEM. The focus is set on modeling of complex fluids, e.g., including multiple phases and dynamic phase transition, and its coupling with deformable structures. Accordingly, an introduction into viscous fluid flow and structural mechanics, and its numerical solution using SPH and the FEM is given in Chapter 2.

1.3 Contributions and accomplishments

This section highlights the author's contributions and accomplishments within the multiphysics applications as presented in Section 1.1, and defines the publications which form the core of this cumulative thesis. To this end, an overview of the author's publications [2, 6, 12, 21–23] is given in Figure 1.3. The two publications illustrated in the orange box (and listed below) form the major accomplishments of this cumulative thesis, along with the content presented in Chapter 2, and are in the remainder of this thesis denoted as [Paper A](#) [21] and [Paper B](#) [22]:

- S. L. Fuchs, C. Meier, W. A. Wall, and C. J. Cyron. A novel smoothed particle hydrodynamics and finite element coupling scheme for fluid-structure interaction: The sliding boundary particle approach. *Computer Methods in Applied Mechanics and Engineering*, 383:113922, 2021
- S. L. Fuchs, C. Meier, W. A. Wall, and C. J. Cyron. An SPH framework for fluid-solid and contact interaction problems including thermo-mechanical coupling and reversible phase transitions. *Advanced Modeling and Simulation in Engineering Sciences*, 8(1):15, 2021

A brief summary of the major accomplishments presented in this cumulative thesis is given in the following:

- A high-performance SPH framework is developed and implemented in the in-house parallel multiphysics research code BACI (Bavarian Advanced Computational Initiative) [24]. The details including the mathematical description, the numerical formulation, and the computational framework as well as numerical examples for the purposes of validation are presented in Chapter 2.

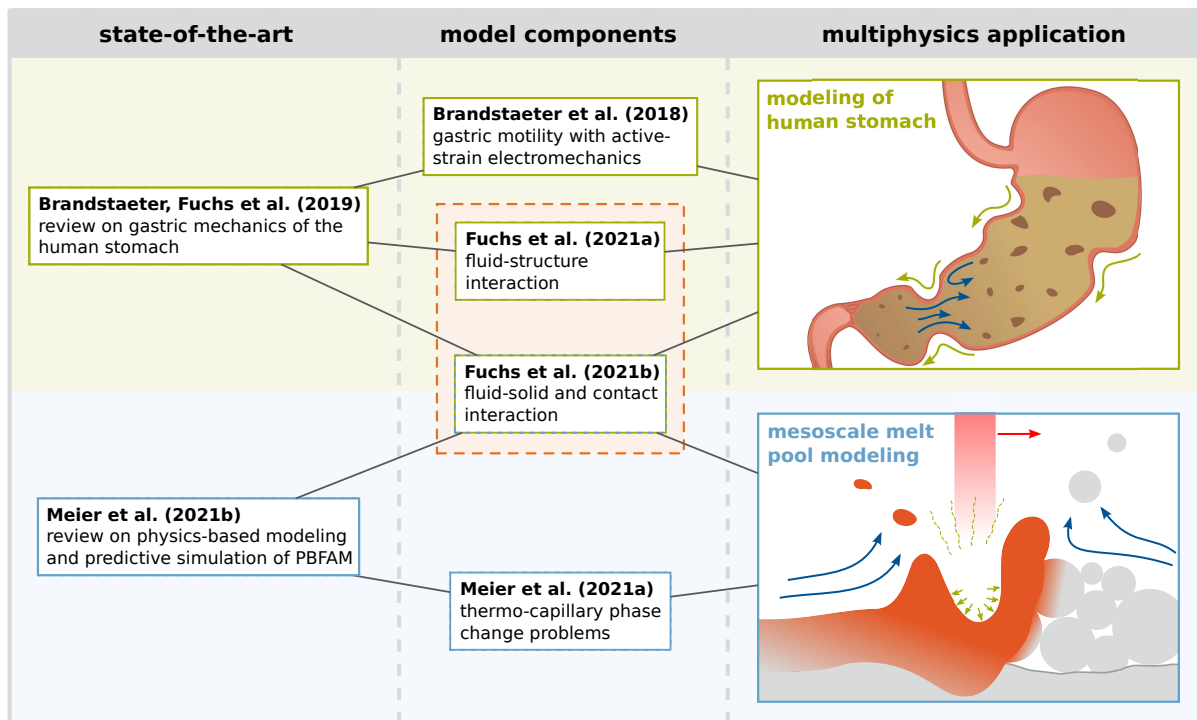


Figure 1.3: Overview of the author's publications [2, 6, 12, 21–23] within the research projects.

- In [Paper A \[21\]](#), the novel sliding boundary particle approach to achieve an accurate representation of fluid quantities close to strongly curved and deformable interface topologies when using SPH as the discretization scheme for the fluid domain is proposed.
- Furthermore, [Paper A \[21\]](#) introduces an SPH and FEM coupling scheme for FSI problems that are characterized by large deformations of the domain.
- Finally, a computational approach for fluid-solid and contact interaction problems including thermo-mechanical coupling and reversible phase transitions using SPH is presented in [Paper B \[22\]](#).

A summary of the publications [Paper A \[21\]](#) and [Paper B \[22\]](#) is given in [Chapter 3](#) along with the author's individual contributions. The full texts of these publications are reprinted in [Appendix A](#).

1.4 Outline

The remainder of this thesis consist of three main parts: First, an introduction into viscous fluid flow and structural mechanics, and its numerical solution using SPH and the FEM is given in [Chapter 2](#). This includes presenting the mathematical descriptions and the numerical formulations along with the computational framework applied within this thesis. For validation purposes, the accuracy and robustness of the numerical formulation and the efficiency and scalability of the parallel computational framework are demonstrated examining several numerical examples

including a strong scaling analysis. A brief summary of the publications [Paper A \[21\]](#) and [Paper B \[22\]](#) (full texts reprinted in [Appendix A](#)) which form the core of this cumulative thesis, is given in [Chapter 3](#) along with the author's individual contributions. Finally, [Chapter 4](#) concludes this thesis with a brief discussion and outlines perspectives for future research.

2 Governing equations and numerical methods

This chapter gives an introduction into viscous fluid flow and structural mechanics, and its numerical solution using the method of smoothed particle hydrodynamics and the finite element method. After briefly presenting the mathematical descriptions, the focus is set on the numerical formulations and the parallel computational framework as applied within this cumulative thesis. Accordingly, the remainder of this chapter is structured as follows: Section 2.1 presents the instationary Navier-Stokes equations in space-continuous form. The fundamentals of SPH are briefly recapitulated in Section 2.2, followed by a weakly compressible SPH formulation for modeling fluid flow in Section 2.3. Section 2.4 presents the nonlinear initial boundary value problem of structural mechanics in local material form. The principals of the FEM for structural mechanics are given in Section 2.5. Next, the details on the parallel computational framework with a focus on an efficient particle neighbor pair detection and a parallel load distribution strategy are provided in Section 2.6. Finally, the accuracy of the formulation and the efficiency of the parallel computational framework are demonstrated in Section 2.7 examining several numerical examples of fluid flow problems in two and three dimensions. Note that parts of this chapter are adapted from the author's publications: [Paper A](#) [21], [Paper B](#) [22], and [23].

2.1 Instationary Navier-Stokes equations for fluid flow

At each time $t \in [0, T]$ the fluid domain Ω^f with the fluid boundary $\Gamma^f = \partial\Omega^f$ is considered. In general, the fluid domain Ω^f may consist of multiple (liquid and gas) phases, however, for ease of notation, it will not be distinguished between different fluid phases in the following. The fluid domain is governed by the instationary Navier-Stokes equations in the domain Ω^f , which consist in convective form of the mass continuity equation and the momentum equation

$$\frac{d\rho^f}{dt} = -\rho^f \nabla \cdot \mathbf{u}^f \quad \text{in } \Omega^f, \quad (2.1)$$

$$\frac{d\mathbf{u}^f}{dt} = -\frac{1}{\rho^f} \nabla p^f + \mathbf{f}_\nu + \mathbf{b}^f \quad \text{in } \Omega^f, \quad (2.2)$$

with viscous force \mathbf{f}_ν and body force \mathbf{b}^f each per unit mass. For a Newtonian fluid the viscous force is given as

$$\mathbf{f}_\nu = \nu^f \nabla^2 \mathbf{u}^f, \quad (2.3)$$

with kinematic viscosity ν^f , which is defined as the ratio of dynamic viscosity η^f and fluid density ρ^f as $\nu^f = \eta^f / \rho^f$. The mass continuity equation (2.1) and the momentum equation (2.2)

represent a system of $d + 1$ equations with the $d + 2$ unknowns, velocity \mathbf{u}^f , density ρ^f , and pressure p^f , in d -dimensional space. The system of equations is closed with an equation of state of the form

$$p^f = p^f(\rho^f) \quad (2.4)$$

relating fluid density ρ^f and pressure p^f . The Navier-Stokes equations (2.1) and (2.2) are subject to the following initial conditions

$$\rho^f = \rho_0^f \quad \text{and} \quad \mathbf{u}^f = \mathbf{u}_0^f \quad \text{in} \quad \Omega^f \quad \text{at} \quad t = 0, \quad (2.5)$$

with initial density ρ_0^f and initial velocity \mathbf{u}_0^f . In addition, Dirichlet and Neumann boundary conditions are applied on the fluid boundary Γ^f

$$\mathbf{u}^f = \hat{\mathbf{u}}^f \quad \text{on} \quad \Gamma_D^f \quad \text{and} \quad \mathbf{t}^f = \hat{\mathbf{t}}^f \quad \text{on} \quad \Gamma_N^f, \quad (2.6)$$

with prescribed boundary velocity $\hat{\mathbf{u}}^f$ and boundary traction $\hat{\mathbf{t}}^f$, and the two disjoint subsets Γ_D^f and Γ_N^f for the Dirichlet and Neumann part of the fluid boundary Γ^f , defined as

$$\Gamma^f = \Gamma_D^f \cup \Gamma_N^f \quad \text{and} \quad \Gamma_D^f \cap \Gamma_N^f = \emptyset. \quad (2.7)$$

Remark 2.1 *In the equations (2.1) and (2.2) governing the fluid domain all time derivatives follow the motion of material points, i.e., are material derivatives $\frac{d(\cdot)}{dt} = \frac{\partial(\cdot)}{\partial t} + \mathbf{u} \cdot \nabla(\cdot)$. Accordingly, $\nabla(\cdot)$ denotes derivatives with respect to spatial coordinates.*

2.2 Spatial discretization via smoothed particle hydrodynamics

A promising approach to model complex fluids is given with the method of smoothed particle hydrodynamics. SPH is a mesh-free discretization scheme that was originally and independently of one another introduced by Gingold and Monaghan [19] and Lucy [20] in 1977. While initially intended to study astrophysical problems, SPH gained increasing importance in other fields of CFD since then. Due to its Lagrangian nature, SPH is very well suited for flow problems involving multiple phases, dynamic phase transitions, as well as complex interface topologies. The fundamental concept of SPH is based on the approximation of a field quantity f via a smoothing operation and on the discretization of a domain Ω with discretization points, so-called particles. In the following, the basics of SPH are recapitulated briefly referring the interested reader to the literature [25–30].

2.2.1 Approximation of field quantities via a smoothing kernel

To begin with, a field quantity f on a domain Ω can be expressed exactly in integral form as

$$f(\mathbf{r}) = \int_{\Omega} f(\mathbf{r}') \delta(|\mathbf{r} - \mathbf{r}'|) \, d\mathbf{r}' \quad (2.8)$$

making use of the Dirac delta function $\delta(r)$. Replacing the latter by a so-called smoothing kernel $W(r, h)$, that fulfills certain consistency properties [27, 28], cf. Section 2.2.3, leads to an approximation of the field quantity f in smoothed integral form

$$f(\mathbf{r}) \approx \int_{\Omega} f(\mathbf{r}') W(|\mathbf{r} - \mathbf{r}'|, h) d\mathbf{r}' \quad (2.9)$$

while committing a smoothing error.

2.2.2 Discretization of the domain with particles

In a next step, the domain Ω is filled with discretization points, so-called particles j , each occupying a volume V_j . Thus, the smoothed integral form of field quantity f reduces in discretized form to a summation of contributions from all particles j in the domain Ω , cf. Figure 2.1,

$$f(\mathbf{r}) \approx \sum_j V_j f(\mathbf{r}_j) W(|\mathbf{r} - \mathbf{r}_j|, h) \quad (2.10)$$

adding a discretization error [31]. A straightforward approach in SPH to determine the gradient of a field quantity f follows directly by differentiation of equation (2.10) resulting in

$$\nabla f(\mathbf{r}) \approx \sum_j V_j f(\mathbf{r}_j) \nabla W(|\mathbf{r} - \mathbf{r}_j|, h). \quad (2.11)$$

Note that this (simple) variant for an approximation of the gradient shows some particular disadvantages. Hence, more advanced approximations for gradients are given in the literature [25, 27–29] and will also be applied in the following.

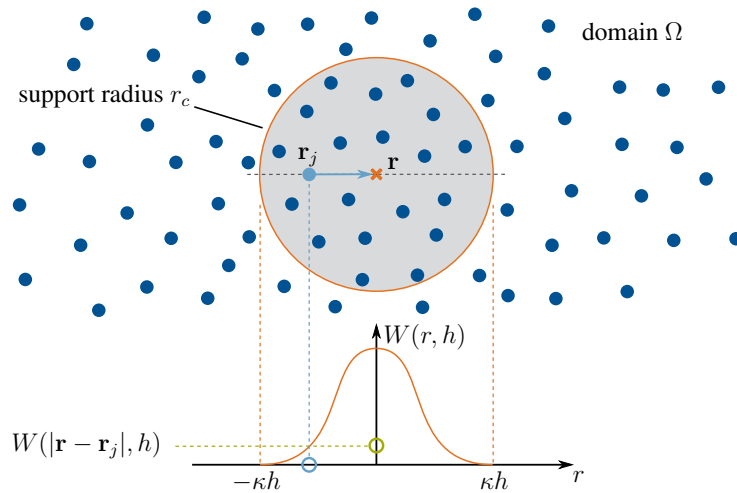


Figure 2.1: Approximation of a field quantity f in the domain Ω via a smoothing kernel $W(r, h)$ with support radius $r_c = \kappa h$ based on discrete field quantities stemming from neighboring particles j .

In sum, the concept of SPH allows to reduce partial differential equations to a system of cou-

pled ordinary differential equations (with as many equations as particles) that is solved in the domain Ω . The transient positions of particles are advected with the velocity resembling the Lagrangian nature of the method. As a result, all field quantities are evaluated at and associated with particle positions, meaning each particle carries its corresponding field quantities. Finally, in a post-processing step the continuous field quantity f is recovered from the discrete field quantities $f(\mathbf{r}_j)$ of particles j in the domain Ω using the approximation (2.10) and the commonly known Shepard filter

$$\hat{f}(\mathbf{r}) \approx \frac{\sum_j V_j f(\mathbf{r}_j) W(|\mathbf{r} - \mathbf{r}_j|, h)}{\sum_j V_j W(|\mathbf{r} - \mathbf{r}_j|, h)}. \quad (2.12)$$

Note that the denominator typically takes on values close to one inside the domain and is mainly relevant for boundary regions with reduced support due to a lack of neighboring particles.

2.2.3 Consistency properties of standard smoothing kernels

The smoothing kernel $W(r, h)$ is a monotonically decreasing, smooth function that depends on a distance r and a smoothing length h . The smoothing length h together with a scaling factor κ define the support radius of the smoothing kernel $r_c = \kappa h$, cf. Figure 2.1. This allows for definition of two typical properties of standard smoothing kernels [32], namely positivity

$$W(r, h) \geq 0 \quad (2.13)$$

and compact support

$$W(r, h) = 0 \quad \text{for } r > r_c. \quad (2.14)$$

In general, all particles in the domain Ω contribute to the SPH approximation of a field quantity f , cf. equation (2.10). However, in practice only the neighboring particles within the support radius r_c need to be considered due to the compact support of the smoothing kernel, cf. Figure 2.1. This property is very beneficial as it reduces the computational effort of the method. In addition, the normalization property

$$\int_{\Omega} W(|\mathbf{r} - \mathbf{r}'|, h) d\mathbf{r}' = 1 \quad (2.15)$$

enables exact interpolation of constant field quantities, while the Dirac delta function property

$$\lim_{h \rightarrow 0} W(r, h) = \delta(r) \quad (2.16)$$

ensures an exact representation of a field quantity f in the limit $h \rightarrow 0$, cf. Section 2.2.1.

Remark 2.2 *In their original work [19] Gingold and Monaghan employed a Gaussian smoothing kernel for the smoothing of field quantities defined as*

$$W(r, h) = \alpha_d e^{-\left(\frac{r}{h}\right)^2} \quad (2.17)$$

with normalization factor α_d given as $\alpha_1 = \frac{1}{\pi^{1/2}h}$, $\alpha_2 = \frac{1}{\pi h^2}$, and $\alpha_3 = \frac{1}{\pi^{3/2}h^3}$ in one-, two-, and three-dimensional space. Note that compact support of the Gaussian smoothing kernel is in the mathematical sense not met for a finite support radius r_c , although, practically applicable as

it approaches zero in a numerical sense [28]. However, this requires a larger support radius r_c resulting in increased computational costs compared to constructed smoothing kernels, e.g., the quintic spline smoothing kernel, cf. Remark 2.3. For this reason, constructed smoothing kernels are often the preferred choice.

Remark 2.3 Within this work, the smoothing of field quantities is carried out using a quintic spline smoothing kernel $W(r, h)$ [28, 33, 34], with smoothing length h and support radius $r_c = \kappa h$ with scaling factor $\kappa = 3$, defined as

$$W(r, h) = \alpha_d \begin{cases} \left(3 - \left(\frac{r}{h}\right)\right)^5 - 6\left(2 - \left(\frac{r}{h}\right)\right)^5 + 15\left(1 - \left(\frac{r}{h}\right)\right)^5, & 0 \leq \left(\frac{r}{h}\right) < 1, \\ \left(3 - \left(\frac{r}{h}\right)\right)^5 - 6\left(2 - \left(\frac{r}{h}\right)\right)^5, & 1 \leq \left(\frac{r}{h}\right) < 2, \\ \left(3 - \left(\frac{r}{h}\right)\right)^5, & 2 \leq \left(\frac{r}{h}\right) < 3, \\ 0, & 3 \leq \left(\frac{r}{h}\right). \end{cases} \quad (2.18)$$

with normalization factor α_d given as $\alpha_1 = \frac{1}{120h}$, $\alpha_2 = \frac{7}{478\pi h^2}$, and $\alpha_3 = \frac{3}{359\pi h^3}$ in one-, two-, and three-dimensional space. A plot of the quintic spline smoothing kernel and its first derivative are given in Figure 2.2.

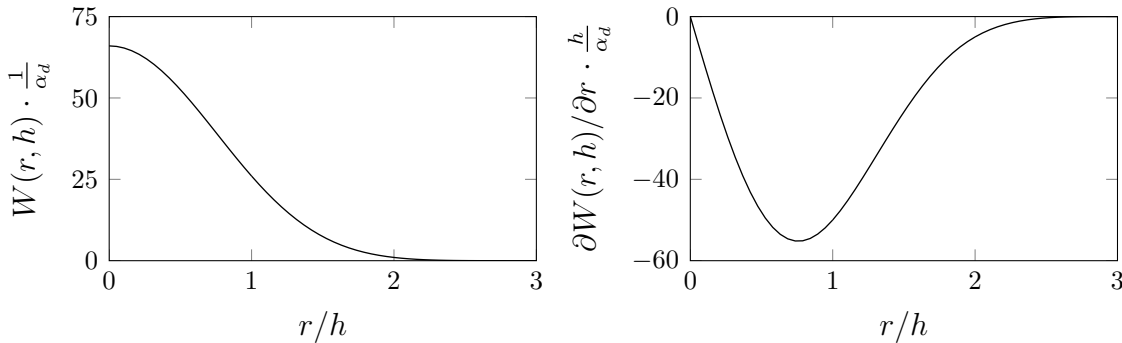


Figure 2.2: Quintic spline smoothing kernel $W(r, h)$ and its first derivative $\partial W(r, h)/\partial r$.

Remark 2.4 In the following, a field quantity f evaluated for particle i at position \mathbf{r}_i is written as $f_i = f(\mathbf{r}_i)$. In addition, the short notation $W_{ij} = W(r_{ij}, h)$ denotes the smoothing kernel evaluated for particle i at position \mathbf{r}_i with neighboring particle j at position \mathbf{r}_j , where $r_{ij} = |\mathbf{r}_{ij}| = |\mathbf{r}_i - \mathbf{r}_j|$ is the absolute distance between particles i and j . Similarly, the derivative of the smoothing kernel with respect to the absolute distance r_{ij} is denoted by $\partial W/\partial r_{ij} = \partial W(r_{ij}, h)/\partial r_{ij}$.

2.2.4 Uniform initial particle spacing in the domain

Within this contribution, the domain Ω is initially filled with particles located on a regular grid with initial particle spacing Δx , thus in d -dimensional space each particle initially occupies an effective volume $V_{eff} = (\Delta x)^d$. Consequently, the mass of a particle is initially assigned using

the reference density ρ_0 of the respective phase and the effective volume V_{eff} . As stated in [33], this approach is quite beneficial as it ensures a consistent initialization of relevant field quantities. Naturally, the choice of the initial particle spacing Δx , together with the smoothing length h of the smoothing kernel, influences the accuracy of SPH. In consequence, for a convergence analysis often the smoothing length h and the ratio $\Delta x/h$ are considered as length scales [31].

Remark 2.5 *Within this work, the smoothing length h of the smoothing kernel $W(r, h)$, cf. Remark 2.3, is set equal to the initial particle spacing Δx . Consequently, in a convergence analysis with decreasing particle spacing Δx the ratio $\Delta x/h$ remains constant [31].*

2.3 Modeling fluid flow via weakly compressible smoothed particle hydrodynamics

The fluid domain governed by the instationary Navier-Stokes equations (2.1) and (2.2) is discretized using smoothed particle hydrodynamics following a weakly compressible approach [27–29]. For modeling fluid flow using SPH, several different formulations each with its own characteristics and benefits can be derived as reflected by the vast amount of literature. The aim of this section is to give an overview of the formulation applied throughout the author’s publications: Paper A [21], Paper B [22], and [23]. For ease of notation, in the following the index $(\cdot)^f$ denoting fluid quantities, as introduced in Section 2.1, is dropped.

2.3.1 Smoothed density field via summation

The density of a particle i is determined via summation of the respective smoothing kernel contributions of all neighboring particles j within the support radius r_c

$$\rho_i = m_i \sum_j W_{ij} \quad (2.19)$$

with mass m_i of particle i . This approach is typically denoted as density summation and results in an exact conservation of mass in the fluid domain, which can be shown in a straightforward manner considering the commonly applied normalization of the smoothing kernel to unity. It shall be noted that the density field may alternatively be obtained by discretization and integration of the mass continuity equation (2.1) [25, 27, 28, 35]. This approach is also denoted as density integration and has advantages when considering free surface flows [36, 37], where naturally regions with reduced support due to a lack of neighboring particles occur. Moreover, density correction schemes, e.g., utilizing a Shepard filter or a moving-least-square interpolation, are proposed in [26, 38, 39].

2.3.2 Discretization of the momentum equation

The momentum equation (2.2) is discretized following [40, 41] including a transport velocity formulation to suppress the problem of tensile instability. The latter will be briefly recapitulated in the following. The transport velocity formulation relies on a constant background pressure p_b

that is applied to all particles and results in a contribution to the particle accelerations for in general disordered particle distributions. However, these additional acceleration contributions vanish for particle distributions fulfilling the partition of unity of the smoothing kernel, thus fostering these desirable configurations. For the sake of brevity, the definition of the modified advection velocity and the additional terms in the momentum equation from the aforementioned transport velocity formulation are not discussed in the following and the reader is kindly referred to the original publication [41]. Altogether, the acceleration $\mathbf{a}_i = d\mathbf{u}_i/dt$ of a particle i results from summation of all acceleration contributions due to interaction with neighboring particles j and a body force \mathbf{b}_i as

$$\mathbf{a}_i = \frac{1}{m_i} \sum_j (V_i^2 + V_j^2) \left[-\tilde{p}_{ij} \frac{\partial W}{\partial r_{ij}} \mathbf{e}_{ij} + \tilde{\eta}_{ij} \frac{\mathbf{u}_{ij}}{r_{ij}} \frac{\partial W}{\partial r_{ij}} \right] + \mathbf{b}_i, \quad (2.20)$$

with volume $V_i = m_i/\rho_i$ of particle i , unit vector $\mathbf{e}_{ij} = \mathbf{r}_i - \mathbf{r}_j/|\mathbf{r}_i - \mathbf{r}_j| = \mathbf{r}_{ij}/r_{ij}$, relative velocity $\mathbf{u}_{ij} = \mathbf{u}_i - \mathbf{u}_j$, and (density-weighted) inter-particle averaged pressure and dynamic viscosity

$$\tilde{p}_{ij} = \frac{\rho_j p_i + \rho_i p_j}{\rho_i + \rho_j} \quad \text{and} \quad \tilde{\eta}_{ij} = \frac{2\eta_i \eta_j}{\eta_i + \eta_j}. \quad (2.21)$$

In the following, the acceleration contribution of a neighboring particle j to particle i is, for ease of notation, denoted as \mathbf{a}_{ij} , where $\mathbf{a}_i = \sum_j \mathbf{a}_{ij} + \mathbf{b}_i$. The above given momentum equation (2.20) exactly conserves linear momentum due to pairwise anti-symmetric particle forces

$$m_i \mathbf{a}_{ij} = -m_j \mathbf{a}_{ji}, \quad (2.22)$$

which can easily be verified considering the property $\partial W/\partial r_{ij} = \partial W/\partial r_{ji}$ of the smoothing kernel.

2.3.3 Equation of state

Following a weakly compressible approach, density ρ_i and pressure p_i of a particle i are linked via the equation of state

$$p_i(\rho_i) = c^2(\rho_i - \rho_0) = p_0 \left(\frac{\rho_i}{\rho_0} - 1 \right) \quad (2.23)$$

with reference density ρ_0 , reference pressure $p_0 = \rho_0 c^2$, and artificial speed of sound c . Note that this commonly applied approach can only capture deviations from the reference pressure, i.e., $p_i(\rho_0) = 0$, and not the total pressure. To limit density fluctuations to an acceptable level, while still avoiding too severe time step restrictions, cf. Section 2.3.5, strategies are discussed in [33] on how to choose a reasonable value for the artificial speed of sound c . Accordingly, in this work the artificial speed of sound c is set allowing an average density variation of approximately 1 %.

2.3.4 Boundary conditions

Modeling boundary (and coupling) conditions using SPH in an accurate and robust manner plays a crucial role and still poses a challenge. This is reflected by the vast amount of literature being

published in this field of research. The purpose of this section is to give an overview of the formulations applied to model boundary conditions within this work. Furthermore, formulations to model coupling conditions for fluid-structure and fluid-solid interaction problems are treated in [Paper A \[21\]](#) and [Paper B \[22\]](#).

Rigid wall boundary conditions

Herein, rigid wall boundary conditions are modeled utilizing boundary particle methods based on fixed layers of particles resembling rigid walls [33, 40, 42]. Consequently, to maintain full support of the smoothing kernel, at least $q = \text{floor}(r_c/\Delta x)$ layers of boundary particles b are placed parallel to the fluid boundary Γ_D^f with a distance of $\Delta x/2$ outside of the fluid domain Ω^f . A boundary particle b contributes to the density summation (2.19) and to the momentum equation (2.20) evaluated for a fluid particle i considered as neighboring particle j . To this end, the respective quantities of boundary particles b are extrapolated from the fluid domain based on a local force balance as described in [40]. For more details the interested reader is referred to the aforementioned literature. For the sake of completeness, it shall be mentioned that several alternative formulations for modeling rigid wall boundaries in SPH are proposed in the literature. Among them are, e.g., penalty-like repulsive force formulations [27, 37, 43], ghost particle formulations [44, 45], or semi-analytical methods considering non-vanishing surface integrals due to missing kernel support [46–49]. For an overview on the advantages and disadvantages of all aforementioned formulations refer to [28, 50–52]. Besides, note that rigid wall boundaries could also be modeled utilizing the sliding boundary particle approach as proposed in [Paper A \[21\]](#).

Remark 2.6 *The floor operator used herein is defined by $\text{floor}(x) := \max \{k \in \mathbb{Z} \mid k \leq x\}$ and returns the largest integer that is less than or equal to its argument x .*

Inflow and outflow boundary conditions

Open boundaries are modeled similar to [53, 54] via defined inflow and outflow zones occupying so-called inflow particles k respectively outflow particles l . Thereby, full support of the interior fluid particles i is maintained for density summation (2.19) and evaluation of the momentum equation (2.20) when evaluating contributions from inflow and outflow particles considered as neighboring particles j . At the inflow, i.e., the Dirichlet boundary, the desired inflow velocity $\hat{\mathbf{u}}$ is prescribed directly to all inflow particles k as $\mathbf{u}_k = \hat{\mathbf{u}}$. The pressure field is extrapolated from the interior fluid particles i to the inflow particles k following

$$p_k = \frac{\sum_i V_i p_i W_{ki}}{\sum_i V_i W_{ki}}. \quad (2.24)$$

At the outflow, i.e., the Neumann boundary, a zero pressure field is prescribed to all outflow particles l following $p_l = 0$. The density field of both inflow and outflow particles is determined from the pressure field with the equation of state (2.23). Finally, to determine consistent velocities \mathbf{u}_l of the outflow particles l , the momentum equation (2.20) is also evaluated for all outflow particles with contributions from fluid, boundary, and outflow particles considered as neighboring particles j , and integrated in time. Alternative formulations to prescribe inflow and outflow boundary conditions, e.g., based on semi-analytical methods, are given in the literature [55, 56].

Periodic boundary conditions

Imposing a periodic boundary condition in a specific spatial direction allows for particle interaction evaluation across opposite domain borders. Moreover, particles leaving the domain on one side are re-injecting on the opposite side. Periodic boundary conditions are commonly applied in SPH modeling of channel or shear flow.

2.3.5 Explicit velocity-Verlet time integration scheme

The (discretized) momentum equation (2.20) is integrated in time applying an explicit velocity-Verlet time integration scheme in kick-drift-kick form [57, 58], also denoted as leapfrog scheme. The velocity-Verlet time integration scheme is known to be of second order accuracy and reversible in time when dissipative effects are absent [27]. In a first kick-step, the accelerations $\mathbf{a}_i^n = (d\mathbf{u}_i/dt)^n$, as determined in the previous time step n , are used to compute the intermediate velocities

$$\mathbf{u}_i^{n+1/2} = \mathbf{u}_i^n + \frac{\Delta t}{2} \mathbf{a}_i^n \quad (2.25)$$

of fluid particles i , where Δt is the time step size. Next, in a drift-step, the positions of fluid particles i are updated to time step $n + 1$ using the intermediate velocities $\mathbf{u}_i^{n+1/2}$ as

$$\mathbf{r}_i^{n+1} = \mathbf{r}_i^n + \Delta t \mathbf{u}_i^{n+1/2}. \quad (2.26)$$

Using the positions \mathbf{r}_i^{n+1} and the intermediate velocities $\mathbf{u}_i^{n+1/2}$, the densities ρ_i^{n+1} and, subsequently, the accelerations \mathbf{a}_i^{n+1} of fluid particles i are computed applying the density summation (2.19) and evaluating the momentum equation (2.20). In a final kick-step, the velocities of fluid particles i at time step $n + 1$ are computed as

$$\mathbf{u}_i^{n+1} = \mathbf{u}_i^{n+1/2} + \frac{\Delta t}{2} \mathbf{a}_i^{n+1}. \quad (2.27)$$

To maintain stability of the explicit velocity-Verlet time integration scheme, the time step size Δt is restricted by the Courant-Friedrichs-Lewy (CFL) condition, the viscous condition, and the body force condition, as

$$\Delta t \leq \min \left\{ 0.25 \frac{h}{c + |\mathbf{u}_{max}|}, 0.125 \frac{h^2}{\nu}, 0.25 \sqrt{\frac{h}{|\mathbf{b}_{max}|}} \right\}, \quad (2.28)$$

with maximum fluid velocity \mathbf{u}_{max} and maximum body force \mathbf{b}_{max} , refer to [33, 41].

2.4 Nonlinear initial boundary value problem of structural mechanics

At each time $t \in [0, T]$ the structural domain Ω^s with the structural boundary $\Gamma^s = \partial\Omega^s$ is considered. In the regime of finite deformations, the structural domain Ω^s is governed by the

balance of linear momentum in the following local material form

$$\rho_0^s \frac{d^2 \mathbf{d}^s}{dt^2} = \nabla_0 \cdot (\mathbf{F}\mathbf{S}) + \rho_0^s \mathbf{b}_0^s \quad \text{in } \Omega^s, \quad (2.29)$$

with the material density ρ_0^s and body force \mathbf{b}_0^s . The structural displacement \mathbf{d}^s are the primary unknowns. The deformation of the structure is described by the deformation gradient $\mathbf{F} = \nabla_0 \mathbf{d}^s$ defining the Green-Lagrange strains $\mathbf{E} = \frac{1}{2}(\mathbf{F}^T \mathbf{F} - \mathbf{I})$. For simplicity, and due to their general applicability in engineering and biomechanics, the second Piola-Kirchhoff stresses \mathbf{S} are chosen to follow from a constitutive relation of the form $\mathbf{S} = \partial \Psi / \partial \mathbf{E}$ based on a hyperelastic strain energy function $\Psi = \Psi(\mathbf{E})$. The partial differential equation (2.29) is subject to the following initial conditions

$$\mathbf{d}^s = \mathbf{d}_0^s \quad \text{and} \quad \frac{d\mathbf{d}^s}{dt} = \frac{d\mathbf{d}_0^s}{dt} \quad \text{in } \Omega^s \quad \text{at } t = 0, \quad (2.30)$$

with initial displacement \mathbf{d}_0^s and initial velocity $d\mathbf{d}_0^s/dt$. Dirichlet and Neumann boundary conditions are applied on the structural boundary Γ^s as

$$\mathbf{d}^s = \hat{\mathbf{d}}^s \quad \text{on } \Gamma_D^s \quad \text{and} \quad (\mathbf{F}\mathbf{S}) \cdot \mathbf{N} = \hat{\mathbf{t}}_0^s \quad \text{on } \Gamma_N^s, \quad (2.31)$$

with prescribed boundary displacement $\hat{\mathbf{d}}^s$, boundary traction $\hat{\mathbf{t}}_0^s$, and outward pointing unit normal vector \mathbf{N} in material configuration. The structural boundary Γ^s is partitioned into the two disjoint subsets Γ_D^s and Γ_N^s defining the Dirichlet and Neumann part as

$$\Gamma^s = \Gamma_D^s \cup \Gamma_N^s \quad \text{and} \quad \Gamma_D^s \cap \Gamma_N^s = \emptyset. \quad (2.32)$$

Remark 2.7 In the equation (2.29) governing the structural domain all time derivatives follow the motion of material points, i.e., are material derivatives $\frac{d(\cdot)}{dt} = \frac{\partial(\cdot)}{\partial t} + \mathbf{u} \cdot \nabla(\cdot)$. Accordingly, $\nabla(\cdot)$ denotes derivatives with respect to spatial coordinates while $\nabla_0(\cdot)$ denotes derivatives with respect to material coordinates.

2.5 Modeling deformable structures via the finite element method

The discretization of the structural domain, governed by the balance of linear momentum (2.29), is based on the finite element method. Since it is not the focus of this work, the basics of the FEM are presented here only very briefly. For further information the interested reader is referred to the literature, e.g., [59–62].

2.5.1 Principle of virtual work

Applying the method of weighted residuals, in the following interpreted as the principle of virtual work, the weak form of the initial boundary value problem for the structural domain can be

obtained as

$$\delta\mathcal{W}^s = \left(\delta\mathbf{d}^s, \rho_0^s \frac{d^2\mathbf{d}^s}{dt^2} \right)_{\Omega^s} + \left(\nabla_0 \delta\mathbf{d}^s, \mathbf{FS} \right)_{\Omega^s} - \left(\delta\mathbf{d}^s, \rho_0^s \mathbf{b}_0^s \right)_{\Omega^s} - \left(\delta\mathbf{d}^s, \hat{\mathbf{t}}_0^s \right)_{\Gamma_N^s} = 0 \quad (2.33)$$

with the variation $\delta\mathbf{d}^s$ of the primary unknown, i.e., the structural displacement \mathbf{d}^s . The variation $\delta\mathbf{d}^s$ is required to be zero on the Dirichlet boundary Γ_D^s in compliance with the Dirichlet boundary condition (2.31). Accordingly, the following trial and test space can be introduced

$$\mathcal{U} = \{ \mathbf{d}^s \mid \mathbf{d}^s \in \mathcal{H}^1(\Omega^s), \mathbf{d}^s(\mathbf{r}^s, t) = \hat{\mathbf{d}}^s(\mathbf{r}^s, t) \text{ on } \Gamma_D^s \}, \quad (2.34)$$

$$\mathcal{V} = \{ \delta\mathbf{d}^s \mid \delta\mathbf{d}^s \in \mathcal{H}^1(\Omega^s), \delta\mathbf{d}^s(\mathbf{r}^s) = 0 \text{ on } \Gamma_D^s \}. \quad (2.35)$$

Herein, $\mathcal{H}^1(\Omega^s)$ denotes the Sobolev space of functions with square-integrable values and first derivatives. Besides, \mathbf{r}^s is the current position of the structural domain. Note that the trial space \mathcal{U} in contrast to the test space \mathcal{V} may depend on the time t . A solution $\mathbf{d}^s \in \mathcal{U}$ of the weak form (2.33) needs to satisfy

$$\delta\mathcal{W}^s = 0 \quad \forall \delta\mathbf{d}^s \text{ in } \mathcal{V}. \quad (2.36)$$

As a result, the weak form (2.33) is equivalent to the strong form of the balance of linear momentum (2.29).

2.5.2 Discretization in space and time

The structural domain Ω^s is approximated by non-overlapping finite elements e with nodes i . Hence, the structural displacement field \mathbf{d}^s is discretized introducing nodal displacements \mathbf{d}_i^s of nodes i . Accordingly, the displacement field is approximated via

$$\mathbf{d}^s(\mathbf{r}^s, t) \approx \sum_j N_j^e(\mathbf{r}^s) \mathbf{d}_j^s(t) \quad (2.37)$$

using Lagrange polynomials N_j^e with compact support inside an element e . Within a Bubnov-Galerkin approach, the same Lagrange polynomials for trial and test functions are employed. Following the iso-parametric concept, the parameter coordinates ξ used for the definition of the shape functions within a standard element geometry are mapped onto the physical coordinates applying the same shape functions also used for the displacement interpolation. With the approximated displacement field (2.37) the weak form (2.33) can be written in terms of the nodal displacements \mathbf{d}_i^s and evaluated elementwise by evaluating the spatial integrals numerically using Gaussian quadrature. The contributions of each element are assembled resulting in a spatially discretized balance of inertia forces, internal forces, and external forces, depending on the nodal displacements \mathbf{d}_i^s and its time derivatives. Subsequently, the semi-discrete form is discretized in time applying a generalized-alpha time integration scheme. Finally, the resulting system of nonlinear equations in residual form is solved for the unknown nodal displacements \mathbf{d}_i^s with a Newton-Raphson scheme.

Remark 2.8 *Within this work, finite elements based on a first-order interpolation are employed.*

However, within the scope of the proposed formulation also finite elements based on a higher-order interpolation could be applied.

2.6 Parallel computational framework

The numerical solution of flow problems, as studied herein, with spatial discretization of the domain via SPH, cf. Section 2.2, requires an efficient parallel computational framework capable of handling systems constituted of a large number of particles. This requires addressing in particular two aspects, namely, an efficient particle neighbor pair detection, and a parallel load distribution strategy, while keeping the communication overhead at an acceptable level. In the literature, several approaches for parallel computational frameworks utilizing particle-based methods have been proposed, e.g., [57, 63–72]. In the present parallel computational framework, a spatial decomposition approach with particle neighbor pair detection utilizing a combination of cell-linked lists and Verlet-lists based on [65] is applied, cf. Section 2.6.1. In addition, the parallel computational framework is extended to enable surface coupling of the particle field with a volume mesh being spatially discretized using the finite element method, cf. Section 2.6.2, in particular with regard to Paper A [21]. Besides, the proposed parallel computational framework supports the motion of rigid bodies that are fully resolved, that is, spatially discretized as clusters of particles, as demonstrated in Paper B [22].

Remark 2.9 *The presented parallel computational framework is implemented in the in-house parallel multiphysics research code BACI (Bavarian Advanced Computational Initiative) [24] taking advantage of third party libraries such as the Message Passing Interface (MPI) [73, 74] for distributed-memory parallel programming, the Trilinos Project [75, 76], and the Zoltan toolkit [77, 78] for partitioning and load balancing. Existing functionality within BACI, especially regarding structural analysis with the FEM, is re-used.*

Remark 2.10 *The proposed concept for an efficient parallel computational framework is applicable not only when using SPH as a discretization scheme, but also for other particle-based methods such as, e.g., the discrete element method (DEM) [79–82], the molecular dynamics (MD) method [69, 83], or the dissipative particle dynamics (DPD) method [84, 85], each with its own problem-specific geometrically limited interaction distance.*

2.6.1 Spatial decomposition of the computational domain

The general idea of the spatial decomposition approach is briefly explained in the following. For detailed information, the interested reader is referred to the original publication [65].

Particle neighbor pair detection

The evaluation of particle interactions in SPH requires knowledge of neighboring particles within a geometrically limited interaction distance, i.e., within the support radius r_c of the smoothing kernel, cf. Section 2.2. Following [65], the computational domain is divided into several cubic cells forming a uniform lattice. Each particle is uniquely assigned to one cell according to its current spatial position, cf. Figure 2.3. This information is stored in so-called cell-linked lists.

The size of the cells r_s is chosen such that the neighboring particles of a particle are either located in the same cell or in adjacent cells. Consequently, to detect all neighboring particles, the cell size r_s is required to be larger than or at least equal to the support radius r_c of the smoothing kernel, i.e., $r_s \geq r_c$. Next, making use of the predefined cell-linked lists, for each particle a Verlet-list is built storing potential neighboring particles within a search radius that is set equal to the cell size r_s , cf. Figure 2.3. The Verlet-list of a particle is valid over time as long as no other particle that was previously located outside the search radius r_s is now located inside the support radius r_c . As a result, this allows to evolve particle positions and to correctly evaluate all particle interactions without the necessity to regularly rebuild the cell-linked lists and the Verlet-lists.

Remark 2.11 *It shall be noted, that generally an optimal size of the search radius r_s , i.e., the cell size r_s , depends on problem-specific parameters. While a search radius r_s close to the support radius r_c requires to rebuild the Verlet-lists more frequently, a larger search radius r_s makes the Verlet-lists contain more potential neighboring particles and increases the communication overhead. Within this work, setting the cell size respectively the search radius to $r_s \approx 1.1 \cdot r_c$ proved to be a good choice balancing the overall computational effort.*

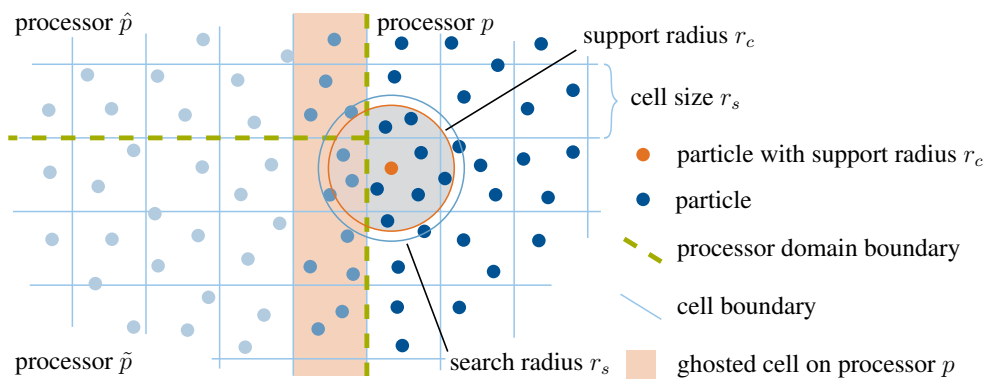


Figure 2.3: Parallel distribution of particles over several processors according to a spatial decomposition approach with particle neighbor pair detection for a single particle with support radius r_c .

Parallel load distribution strategy

Following a spatial decomposition approach, the cells together with assigned particles are distributed over all involved processors, i.e., forming so-called processor domains, cf. Figure 2.3. To keep the computational load balanced between all processors and to minimize the communication overhead, ideally cubic processor domains are defined such that each contains (nearly) the same number of particles. This is achieved via a (coordinate-based) geometric partitioning approach, e.g., based on recursive coordinate bisection [78, 86], considering certain weights assigned to each cells. An adaptive repartitioning strategy ensures that the computational load remains balanced also in the case of large particle movement. The cells occupied by each processor are called owned cells. On each processor the position of particles located in its processor domain, i.e., the position of so-called owned particles, is evolved. Accordingly, this requires the

evaluation of particle interactions of owned particles with their neighboring particles. However, the correct evaluation of particle interactions close to processor domain boundaries requires that each processor has information not only about its owned particles but also about particles in cells adjacent to its processor domain. To this end, each processor is provided full information not only about its own domain but additionally about a layer of ghosted cells (with ghosted particles) around its own domain. Keeping the information about ghosted cells and particles continuously updated requires communication between processors.

Remark 2.12 *To exemplify the cost of communication overhead, consider a perfectly cubic processor domain occupying n_o owned cells. Consequently, assuming one layer of ghosted cells surrounding the processor domain, a total of $n_g = (\sqrt[3]{n_o} + 2)^3 - n_o$ cells are ghosted. That is, the communication overhead scales with the ratio n_g/n_o of ghosted cells n_g to owned cells n_o . Furthermore, the (average) number of particles per cell, and, consequently, also the communication overhead, scale with the ratio $r_c/\Delta x$ of the support radius r_c and the initial particle spacing Δx .*

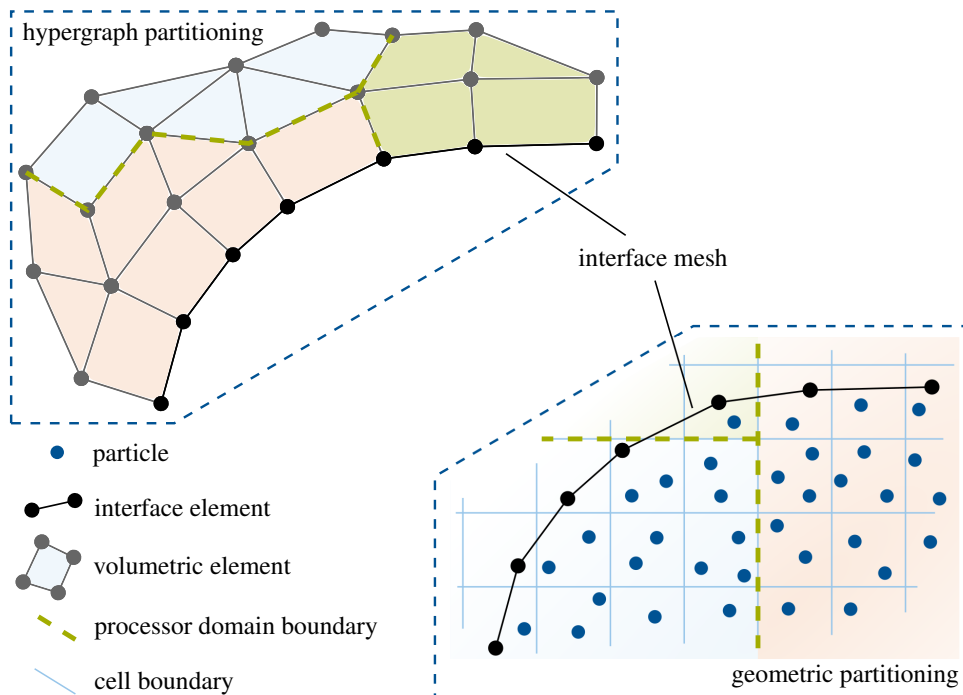


Figure 2.4: Parallel distribution of a volume mesh via a (connectivity-based) hypergraph partitioning approach, and of a particle field via a (coordinate-based) geometric partitioning approach, over several processors with a conforming interface mesh introduced to facilitate the exchange of kinematic and kinetic quantities.

2.6.2 Surface coupling of the particle field with a volume mesh

A numerical formulation for solving FSI problems, where the fluid domain is spatially discretized using SPH and the structural domain using the FEM, is proposed in [Paper A \[21\]](#).

For this purpose, the parallel computational framework is extended to enable surface coupling of the particle field with a volume mesh. In contrast to the particle field, that is distributed to the processors via a (coordinate-based) geometric partitioning approach, the volume mesh is distributed based on a (connectivity-based) hypergraph partitioning approach, e.g., [87, 88], within this parallel computational framework. Accordingly, Figure 2.4 illustrates the concept applied for the parallel distribution of the volume mesh and the particle field over several processors. To facilitate the exchange of kinematic and kinetic quantities between the particle field and the volume mesh, e.g., as required for the evaluation of the surface coupling condition, an extraction of the volume mesh at the surface respectively interface is introduced. A clone of this so-called interface mesh is, along with the particle field, distributed to the processors, cf. Figure 2.5. In a next step, each interface element is assigned to the cells according to a spatial decomposition approach. Consequently, particle to interface element neighbor pair detection can then be performed very similarly as described in Section 2.6.1, i.e., based on a combination of cell-linked lists and Verlet-lists. Finally, it shall be stated that the exchange of kinematic and kinetic quantities of the particle field and the volume mesh at the interface mesh may require communication between processors due to potentially different parallel distribution, cf. Figure 2.4.

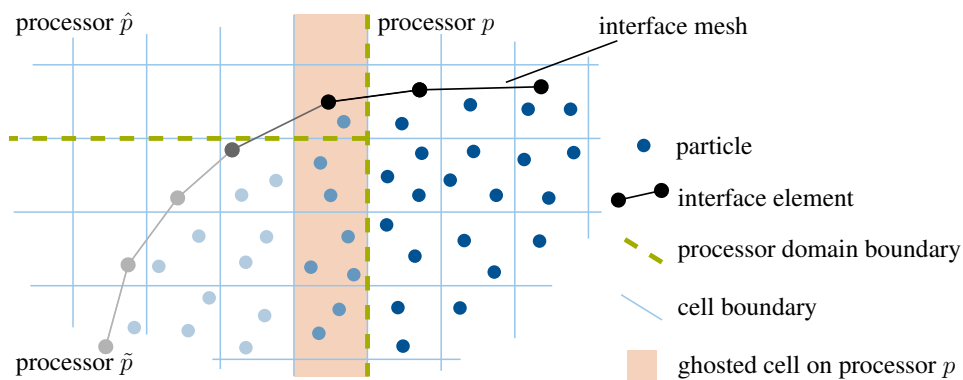


Figure 2.5: Parallel distribution of an interface mesh and particles over several processors according to a spatial decomposition approach.

Remark 2.13 *Note that volume coupling of the particle field with a volume mesh could be realized with the proposed parallel computational framework in a straightforward manner. To reduce the cost of communication, this would require to distribute the volume mesh, along with the particle field, via a (coordinate-based) geometric partitioning approach to the processors.*

2.7 Numerical examples of fluid flow problems

The purpose of this section is to demonstrate the accuracy of the applied formulation and the efficiency of the parallel computational framework examining several numerical examples of fluid flow problems in two and three dimensions. The obtained results are compared to analytical and reference solutions given in the literature both in quantitative and qualitative manner. The parameter values in the numerical examples are given in a consistent set of units and presented in non-dimensional form.

2.7.1 Poiseuille and Couette flow

In the following a Poiseuille and a Couette flow are examined. The obtained results are compared with the analytical solution as given, e.g., in [33]. A rectangular channel of length $L = 0.5$ and height $H = 1.0$ is occupied by a Newtonian fluid with density $\rho^f = 1.0$ and kinematic viscosity $\nu^f = 1.0 \times 10^{-2}$. The coordinate axes \mathbf{e}_x and \mathbf{e}_y are pointing in longitudinal and transversal direction of the channel. Periodic boundary conditions are applied at the left and right end of the channel. No-slip boundary conditions are applied at the bottom and top channel wall. In the case of a Poiseuille flow, a gravitational acceleration of magnitude $|\mathbf{g}| = 0.1$ is acting in positive x -direction set as body force (per unit mass), while in the case of a Couette flow, the top wall of the channel moves with a velocity $u_w = 1.25$ in positive x -direction. The Reynolds number of the problem is given as $Re = u_{max}H/\nu^f = 125$ for both Poiseuille and Couette flow with maximum velocity $u_{max} = 1.25$ as obtained from the analytical solution [33]. For the fluid phase, an artificial speed of sound $c = 12.5$ is chosen, resulting in a reference pressure $p_0 = 156.25$ of the weakly compressible model. The background pressure p_b of the transport velocity formulation is set equal to the reference pressure p_0 . The walls of the box are modeled using boundary particles. The problem is solved for different values of the initial particle spacing Δx for times $t \in [0, 80.0]$ with time step size Δt obeying respective conditions (2.28).

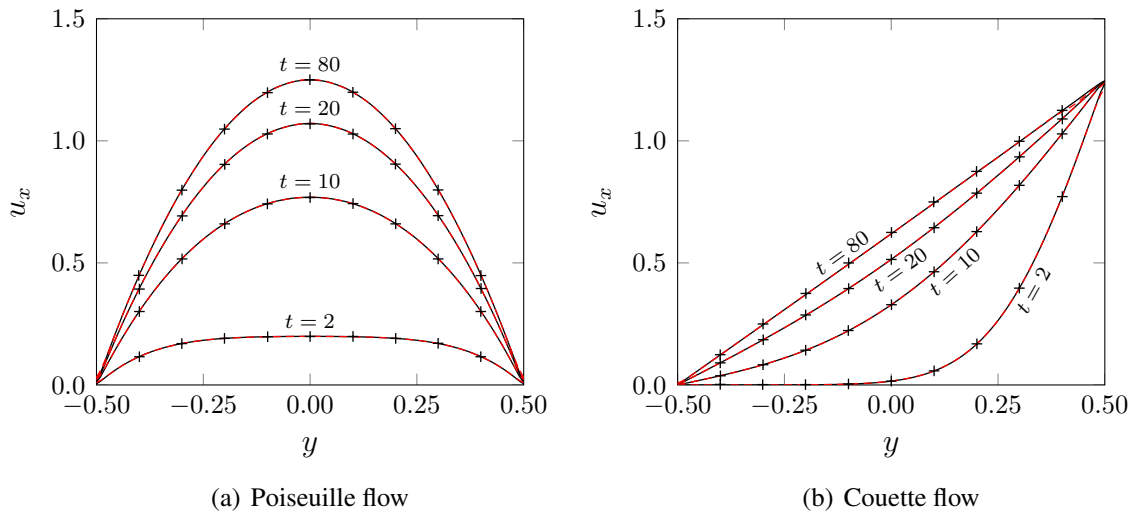


Figure 2.6: Poiseuille and Couette flow: velocity profile u_x across the channel obtained with the proposed formulation and an initial particle spacing of $\Delta x = 2.0 \times 10^{-2}$ (red dashed line) and 1.0×10^{-2} (black solid line) compared to analytical solution (crosses) at different points in time.

The results are post-processed applying SPH approximation (2.12) also considering the quantities of boundary particles. The obtained velocity profile u_x across the channel is displayed for the cases of a Poiseuille and a Couette flow in Figure 2.6 for different values of the initial particle spacing Δx at different points in time. The obtained results are in very good agreement with the analytical solution [33]. At time $t = 80$ a steady state has developed that is characterized by a parabolic velocity profile for Poiseuille flow and a linear velocity profile for Couette flow in accordance with the analytical solution.

2.7.2 Shear-driven cavity flow

In the following, a shear-driven cavity flow is considered representing a well-known CFD benchmark problem for viscous fluid flow [89–91]. The geometry and boundary conditions of the benchmark problem are relatively simple, though it is characterized by complex flow patterns. For validation, the results obtained with the proposed formulation are compared to [89] applying a finite-difference method to discretize the fluid domain. A closed quadratic cavity with edge length $B = 0.1$ is filled by a Newtonian fluid initially at rest with density $\rho^f = 1.0$. The coordinate axes \mathbf{e}_x and \mathbf{e}_y are pointing in horizontal and vertical direction. The top wall of the cavity moves with a velocity $u_w = 1.0$ in positive x -direction, while the remaining walls of the cavity are spatially fixed. No-slip boundary conditions are applied on all walls of the cavity. Accordingly, the Reynolds number of the problem is given as $Re = u_w B / \nu^f$. In the following, two different cases characterized by the Reynolds numbers $Re = 100$ and $Re = 1000$ are considered, achieved by varying the kinematic viscosity ν^f accordingly. For the fluid phase, an artificial speed of sound $c = 10.0$ is chosen, resulting in a reference pressure $p_0 = 100.0$ of the weakly compressible model. The background pressure p_b of the transport velocity formulation is set equal to the reference pressure p_0 . The walls of the box are modeled using (moving) boundary particles. The problem is solved for different values of the initial particle spacing Δx for times $t \in [0, 25.0]$ with time step size Δt obeying respective conditions (2.28).

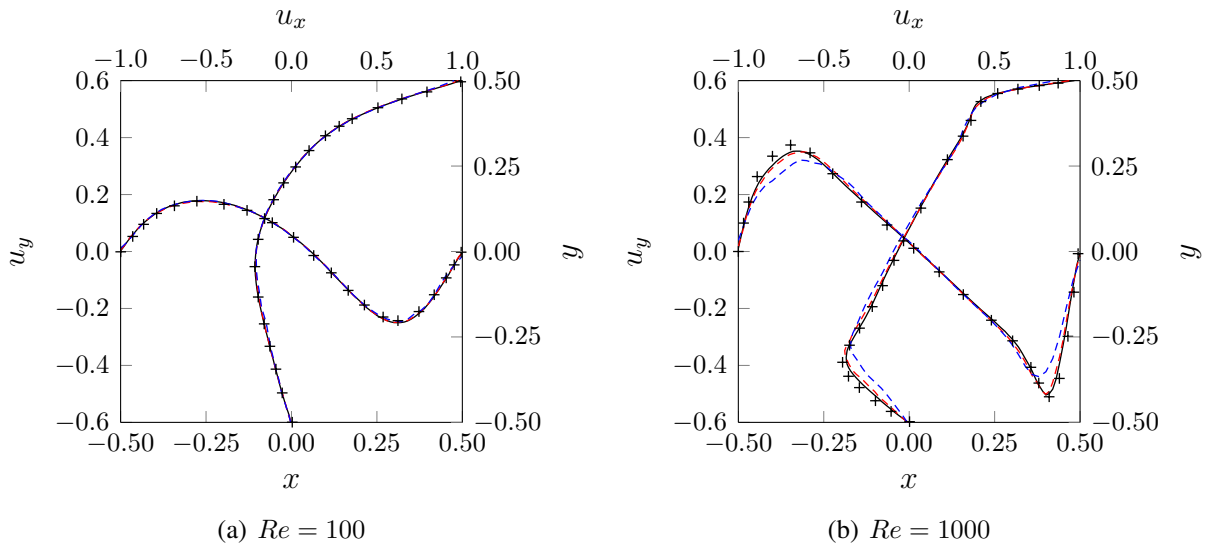


Figure 2.7: Shear-driven cavity flow: velocity profiles u_x and u_y along the vertical and horizontal centerline obtained with the proposed formulation and an initial particle spacing of $\Delta x = 2.0 \times 10^{-2}$ (blue dashed line), $\Delta x = 1.0 \times 10^{-2}$ (red dashed line), and $\Delta x = 5.0 \times 10^{-3}$ (black solid line) compared to the reference solution [89] (crosses).

The results are post-processed applying SPH approximation (2.12) also considering the quantities of boundary particles. The obtained velocity profiles u_x and u_y along the vertical and horizontal centerline of the cavity in the steady state are displayed in Figure 2.7 for different values of the initial particle spacing Δx and different Reynolds numbers Re compared to the reference solution [89]. The results for Reynolds number $Re = 100$ obtained with different initial particle

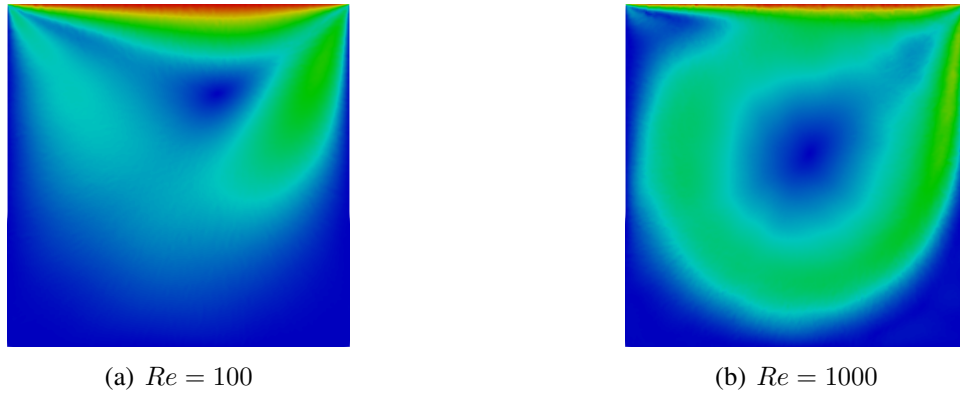


Figure 2.8: Shear-driven cavity flow: magnitude of the fluid velocity field ranging from 0.0 (blue) to 1.0 (red) obtained with the proposed formulation and an initial particle spacing of $\Delta x = 5.0 \times 10^{-3}$.

spacing Δx show only minor differences and are in very good agreement to the reference solution [89]. For Reynolds number $Re = 1000$, the results obtained with different initial particle spacing Δx show good convergence against the reference solution [89]. Finally, the magnitude of the fluid velocity field in the steady state is displayed in Figure 2.8 obtained with an initial particle spacing of $\Delta x = 5.0 \times 10^{-3}$ for different Reynolds numbers Re . The fluid flow in the cavity is characterized by a large primary vortex induced by shear forces in the fluid due to the movement of the top wall of the cavity. In addition, for Reynolds number $Re = 1000$, secondary vortices in the bottom corners of the cavity emerge. Furthermore, these results are qualitatively in very good agreement with the results of [41], confirming accurate implementation of the SPH formulation.

2.7.3 Three-dimensional Rayleigh-Taylor instability

The purpose of this example is to demonstrate the capability and efficiency of the parallel computational framework in handling systems constituted of a large number of particles. To this end, a three-dimensional Rayleigh-Taylor instability consisting of a total of approximately 3.54×10^6 particles is examined on a parallel system, and conclusions are drawn concerning the parallel behavior of the parallel computational framework. A Rayleigh-Taylor instability is initiated at the interface of a lighter and a heavier fluid phase under the influence of gravity due to a disturbance. Consider a rectangular domain of height $H = 2.0$ and widths $B = 1.0$ with coordinate system in the center. The coordinate axes e_x and e_y are pointing in lateral direction, and the coordinate axis e_z in vertical direction. The domain is occupied by a Newtonian fluid initially at rest consisting of two fluid phases: a lighter fluid phase with density $\rho^l = 1.0$ at the bottom and a heavier fluid phase with density $\rho^h = 1.8$ on top. The interface between the two fluid phases is described as $z = 0.15 \sin(2\pi x) \sin(2\pi y)$. Periodic boundary conditions are applied in x - and y -direction and no-slip boundary conditions are applied at the bottom and top faces of the domain. A gravitational acceleration of magnitude $|g| = 1.0$ is acting in negative z -direction.

The Reynolds number and the Froude number of the problem are similarly to [41, 92] set to

$$Re = u_{ref}H/\nu^f = 420 \quad \text{and} \quad Fr = u_{ref}/\sqrt{|g|H} = 1.0, \quad (2.38)$$

resulting in the reference velocity $u_{ref} = \sqrt{|g|H}$ and defining the kinematic viscosity ν^f of both fluid phases. The reference pressure of the weakly compressible model is set to $p_0^l = 200.0$ and $p_0^h = 360.0$ for the lighter and heavier fluid phase with artificial speed of sound $c = 10u_{ref} \approx 14.14$. The background pressure p_b of the transport velocity formulation is set equal to the reference pressure of each phase. No-slip boundary conditions at the bottom and top faces are modeled using boundary particles. The complete domain is discretized by particles with initial particle spacing $\Delta x = 0.025/3$ resulting in a total of approximately 3.54×10^6 particles, thereof 3.46×10^6 fluid particles and 8.64×10^4 boundary particles. Following a spatial decomposition approach, the computational domain is divided into $36 \times 36 \times 76$ cubic cells resulting in approximately 36 particles per cell. The problem is solved for times $t \in [0, 10.0]$ with a time step size of $\Delta t = 1.0 \times 10^{-4}$.

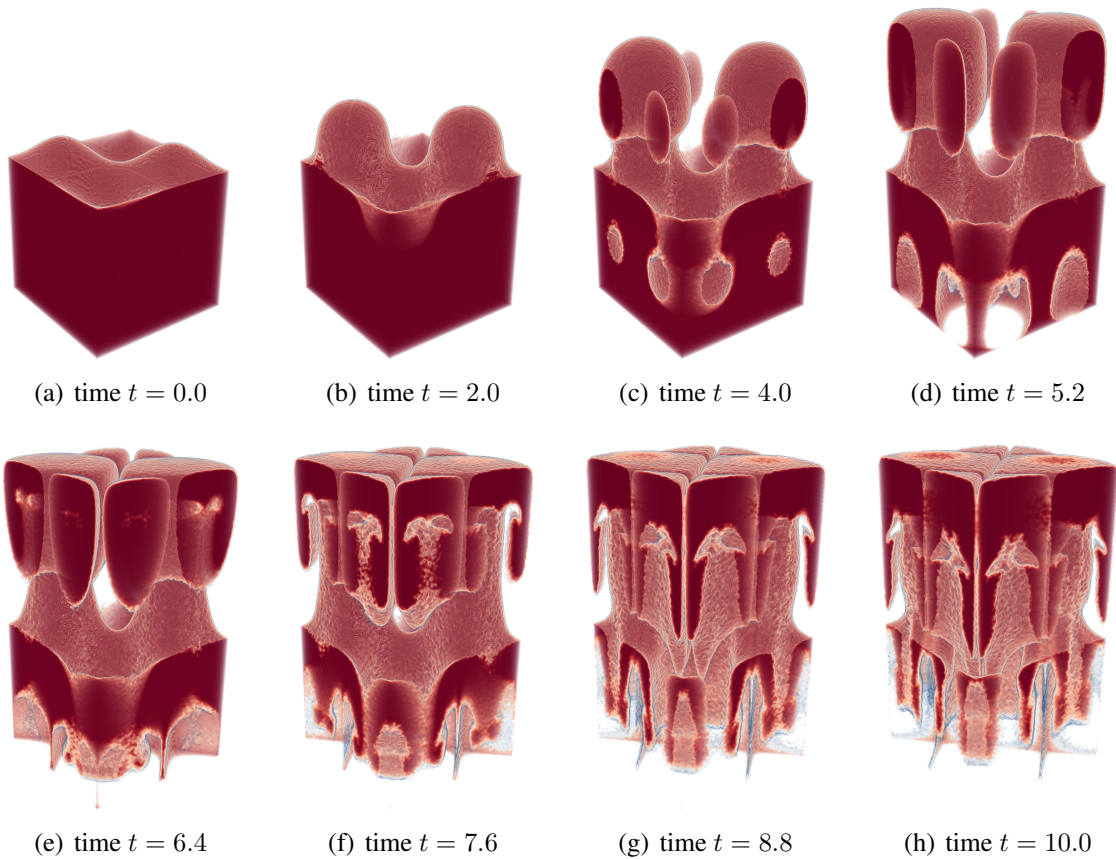


Figure 2.9: Three-dimensional Rayleigh-Taylor instability: time series of the obtained results with density field ranging from $\rho^l = 1.0$ (red) to $(\rho^l + \rho^h)/2 = 1.4$ (blue).

For the purposes of illustration, a time series of the obtained results is given in Figure 2.9. The density field of both phases is post-processed applying SPH approximation (2.12) and visualized

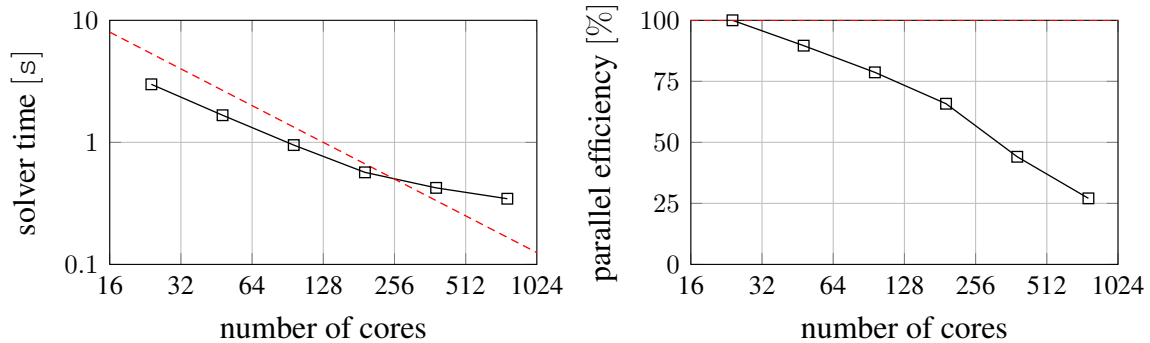


Figure 2.10: Three-dimensional Rayleigh-Taylor instability: solver time per time step (left) and parallel efficiency given in percent of linear scaling (right) for a problem consisting of approximately 3.54×10^6 particles on up to 768 cores (Intel Xeon E5-2680 v3 Haswell, 2.5 GHz) compared to optimal linear scaling (red dashed line).

by a specific color code with opacity. Next, a strong scaling analysis is performed to showcase the capability and efficiency of the parallel computational framework, utilizing a parallel system consisting of up to 32 nodes with 2×12 cores (Intel Xeon E5-2680 v3 Haswell, 2.5 GHz). The parallel behavior of the computational framework is shown in Figure 2.10, illustrating the obtained solver time per time step and the parallel efficiency given in percent of linear scaling. The parallel efficiency is computed as $t_1 / (n \cdot t_n) \cdot 100\%$, where t_1 and t_n are the times to solve the problem on one node respectively n nodes. Almost linear scaling is observed for up to 192 cores on the considered parallel system with a parallel efficiency of more than 65%. Finally, for larger number of cores, the scalability deteriorates and the parallel efficiency drops to under 50% due to an increasing communication overhead, cf. Remark 2.12. Similar results of a strong scaling analysis of an SPH framework are given, e.g., in [70] ($r_c/\Delta x = 2.5$) and [93] ($r_c/\Delta x = 2.4$), however, in contrast to this example ($r_c/\Delta x = 3.0$) with a smaller ratio of the support radius r_c and the initial particle spacing Δx , thus, resulting in a lower influence on the communication overhead, cf. Remark 2.12. The obtained results confirm, that the parallel computational framework is capable of efficiently solving three-dimensional systems constituted of a large number of particles on multiple cores.

3 Summary of publications

This chapter gives a brief summary of the publications [Paper A \[21\]](#) and [Paper B \[22\]](#) which form the core of this cumulative thesis and highlights the author's individual contributions:

- S. L. Fuchs, C. Meier, W. A. Wall, and C. J. Cyron. A novel smoothed particle hydrodynamics and finite element coupling scheme for fluid-structure interaction: The sliding boundary particle approach. *Computer Methods in Applied Mechanics and Engineering*, 383:113922, 2021
- S. L. Fuchs, C. Meier, W. A. Wall, and C. J. Cyron. An SPH framework for fluid-solid and contact interaction problems including thermo-mechanical coupling and reversible phase transitions. *Advanced Modeling and Simulation in Engineering Sciences*, 8(1):15, 2021

The full texts of these publications are reprinted in [Appendix A](#).

3.1 Paper A

A novel smoothed particle hydrodynamics and finite element coupling scheme for fluid-structure interaction: The sliding boundary particle approach

Sebastian L. Fuchs, Christoph Meier, Wolfgang A. Wall, Christian J. Cyron

Summary

This publication proposes a novel numerical formulation for solving fluid-structure interaction (FSI) problems. The fluid domain is spatially discretized using smoothed particle hydrodynamics (SPH) and the structural domain using the finite element method (FEM). Due to the Lagrangian nature and the mesh-free character of SPH, this approach provides some significant benefits as compared to fully mesh- or grid-based FSI frameworks: That is, SPH simplifies the treatment of large deformations of the fluid domain without additional methodological and computational effort. Besides, the proposed formulation can be easily extended to account for multiphase flow and dynamic phase transitions.

The coupling of both sub-domains is based on a Dirichlet-Neumann partitioned approach, where the fluid domain is the Dirichlet partition with prescribed interface displacements and velocities, and the structural domain is the Neumann partition subject to interface forces. Hence, the interface forces are evaluated by the fluid solver utilizing the current interface displacements and velocities which are directly extracted from the structural domain. Afterwards, the interface forces are applied to the structural solver enforcing conservation of linear momentum. An iterative fixed-point coupling scheme [94] is employed to satisfy dynamic equilibrium at the fluid-structure interface with respect to a predefined convergence criterion. This so-called strong coupling of fluid and structural domain is crucial to overcome instabilities, e.g., due to the artificial added mass effect, that are known to occur for weakly coupled schemes in FSI [95, 96].

Introducing the sliding boundary particle approach for the treatment of highly deformable and strongly curved boundaries of the fluid domain in an accurate, robust, and computationally efficient manner, constitutes an important aspect of the proposed numerical formulation for solving FSI problems. The concept of the proposed sliding boundary particle approach is based on a transient set of virtual boundary particles that are regularly arranged around the current projection point of a fluid particle onto the fluid domain boundary. Accordingly, the transient set of virtual boundary particles ensures full support of the smoothing kernel. Moreover, a generalized formulation for the extrapolation of field variables from fluid to virtual boundary particles is proposed, which is inspired by the procedure of [40].

Finally, the accuracy and robustness of the novel sliding boundary particle approach and the proposed numerical formulation for solving FSI problems are demonstrated studying several numerical examples, among others, in the form of well-known CFD and FSI benchmark problems [97, 98]. Altogether, the obtained numerical results are in very good agreement with analytical or reference solutions. Finally, a three-dimensional, application-focused example is considered reaping the full benefits of the novel sliding boundary particle approach and confirming the applicability of the proposed formulation to capture large deformations of the fluid domain.

In conclusion, the proposed numerical formulation for solving FSI problems has the ability to

accurately model a host of complex multiphysics problems involving dynamic effects and large interface displacements for detailed studies in engineering and biomechanics.

Contribution

Sebastian L. Fuchs and Christoph Meier derived the model equations and conceived the general concept of the proposed modeling approach. Sebastian L. Fuchs carried out the specific code implementation in the in-house parallel multiphysics research code BACI (Bavarian Advanced Computational Initiative) [24] and performed the numerical simulations. Sebastian L. Fuchs prepared the draft for the manuscript. All authors provided critical feedback and contributed to the final version of the manuscript.

Reference

S. L. Fuchs, C. Meier, W. A. Wall, and C. J. Cyron. A novel smoothed particle hydrodynamics and finite element coupling scheme for fluid-structure interaction: The sliding boundary particle approach. *Computer Methods in Applied Mechanics and Engineering*, 383:113922, 2021

3.2 Paper B

An SPH framework for fluid-solid and contact interaction problems including thermo-mechanical coupling and reversible phase transitions

Sebastian L. Fuchs, Christoph Meier, Wolfgang A. Wall, Christian J. Cyron

Summary

Fluid-solid and contact interaction problems that are characterized by a large number of solid bodies immersed in a fluid flow while undergoing (reversible) phase transitions are of great interest in many applications in engineering and biomechanics. In most cases, explicitly modeling the deformation of solid bodies is not required and thus it is sufficient to consider undeformable but mobile rigid bodies as it reduces the complexity of the problem and simplifies the modeling approach.

To this end, a computational approach for fluid-solid and contact interaction problems including thermo-mechanical coupling and reversible phase transitions is presented in this publication. The solid domain consists of several arbitrarily-shaped, undeformable but mobile rigid bodies that are evolved in time separately, and thus, may get into mechanical contact with each other. The fluid domain generally consist of multiple (liquid and gas) phases. A temperature field is evaluated for both fluid and solid domain by solving the heat equation, and thus, allows for evaluation of reversible phase transitions in the form of melting and solidification between the fluid and solid domain. Consequently, the shape and also the total number of rigid bodies may vary over time.

Most current mesh- or grid-based methods require substantial methodological and computational efforts to model continually changing interface topologies, reversible phase transitions, and dynamic motion of rigid bodies in fluid flow. The method of smoothed particle hydrodynamics (SPH), being a mesh-free discretization scheme and due to its Lagrangian nature, is particularly well suited to capture such phenomena. For this reason, in the proposed computational approach all domains are spatially discretized using SPH. Accordingly, the rigid bodies are fully resolved, that is, spatially discretized as clusters of particles. This allows to utilize advanced boundary particle methods, e.g., based on the extrapolation of field quantities from fluid to boundary particles [33, 40, 42], to accurately model momentum exchange at the fluid-solid interface. Proposing a detailed concept for the parallelization of the computational approach, especially for a computationally efficient evaluation of rigid body motion, is far from trivial but indispensable when examining numerical examples that are of practical relevance, and thus, constitutes an essential part of this publication.

Finally, the accuracy and robustness of the proposed computational approach for fluid-solid and contact interaction problems including thermo-mechanical coupling and reversible phase transitions is shown by several numerical examples in two and three dimensions, among others, involving multiple rigid bodies, two-phase flow, and reversible phase transitions. A focus is set on two potential application scenarios in the fields of engineering and biomechanics: powder bed fusion additive manufacturing (PBFAM) and disintegration of food boluses in the human stomach. Above that, the parallel behavior and efficiency of the proposed computational ap-

proach is demonstrated by a strong scaling analysis of a three-dimensional example, confirming that detailed studies at a large scale are possible.

Altogether, highly dynamic motion of arbitrarily-shaped rigid bodies embedded in a multi-phase flow and simultaneously occurring reversible phase transitions can be captured by the proposed computational approach in an accurate, robust, and computationally efficient manner. In conclusion, the proposed computational approach has the ability to model a host of complex multiphysics problems, and is thus expected to become a valuable tool for advanced studies in the fields of engineering and biomechanics.

Contribution

Sebastian L. Fuchs and Christoph Meier contributed to the derivation of model equations and worked out the general concept of the proposed modeling approach. Sebastian L. Fuchs performed the specific code implementation in the in-house parallel multiphysics research code BACI (Bavarian Advanced Computational Initiative) [24] and conducted the numerical simulations. Sebastian L. Fuchs prepared the draft for the manuscript. All authors contributed to the discussion of results and approved the final manuscript.

Reference

S. L. Fuchs, C. Meier, W. A. Wall, and C. J. Cyron. An SPH framework for fluid-solid and contact interaction problems including thermo-mechanical coupling and reversible phase transitions. *Advanced Modeling and Simulation in Engineering Sciences*, 8(1):15, 2021

4 Discussion and conclusion

Computational modeling of multiphysics problems in science and engineering, especially in biomechanics, is a challenging task. Applications in these fields are often characterized by multiphase flow, (reversible) phase transitions, geometrically complex and continually changing interface topologies, or fluid-structure interactions. To allow for sophisticated in-silico studies of multiphysics applications, advanced computational approaches are required which capture these phenomena. However, the most commonly applied mesh- or grid-based methods necessitate substantial methodological and computational efforts, e.g., for interface tracking, to model the aforementioned class of multiphysics problems. By contrast, SPH, as a mesh-free discretization scheme and due to its Lagrangian nature, is particularly suitable for applications involving multiphase flow, phase transitions, as well as complex interface topologies. In recent years, SPH has been applied to a wide range of applications, e.g., in biomechanics, to model vascular [99, 100] and cardiac hemodynamics [101–103], intestinal [104–106] and gastric peristalsis [107], or cerebrospinal fluid [108]. This showcases the method’s general applicability to simulate complex fluid flow.

This cumulative thesis is devoted to the development of accurate, robust, and computationally efficient numerical formulations for multiphysics problems in science and engineering using SPH and the FEM. In general, the numerical solution of realistic coupled multiphysics problems at a large scale with spatial discretizations via SPH and the FEM requires an efficient parallel computational framework that can handle systems containing a large number of particles and finite elements. To this end, a highly efficient SPH framework is developed and presented in Section 2.6 and (with an extension for the motion of rigid bodies) in Paper B [22]. Moreover, Paper A [21] proposes a computational framework for solving FSI problems, in which the fluid domain is spatially discretized using SPH and the structural domain using the FEM, to accurately model complex multiphysics problems involving dynamic effects and large interface displacements. Finally, a numerical formulation to model highly dynamic motions of arbitrarily-shaped rigid bodies embedded in a multiphase flow is presented in Paper B [22]. In this formulation, SPH is used for the spatial discretization of all domains, thus, the rigid bodies are fully resolved as clusters of particles. In addition, thermal conduction and reversible phase transitions between the fluid and the rigid bodies is considered. In summary, the computational methods proposed in Chapter 2, Paper A [21], and Paper B [22] can be applied to problems ranging from classical engineering to biomechanics. This includes, for example, mesoscale melt pool modeling in metal PBFAM processes and the digestion of food in the human stomach.

In metal PBFAM, complex structural components are created by melting and fusing a metal powder layer per layer to form the final part. This process is expected to open up entirely new opportunities in product design, manufacturing, and supply chains. However, the overall metal PBFAM process is still not completely understood due to its complexity, giving rise to the need for detailed physics-based modeling and predictive simulations, among others in the field of computational melt pool modeling. A detailed literature review on metal PBFAM is given, e.g.,

in [11–13]. Additionally, [12] gives an overview of several modeling approaches of the powder bed, the melt pool, and the solidified structural part. The melt pool dynamics in metal PBFAM are characterized by thermo-capillary flow [109, 110] involving solid, liquid, and gaseous phases as well as continuous phase transitions. Recently, a promising SPH formulation that captures these physical phenomena has been proposed [23], with a special focus on evaporation-induced recoil pressure forces, temperature-dependent surface tension and wetting forces, Gaussian laser beam heat sources, and evaporation-induced heat losses. Other SPH formulations for mesoscale melt pool modeling in metal PBFAM are presented in [111–114]. For simplicity, all the aforementioned approaches are restricted to immobile powder grains. However, in the real physical process induced gas flow and high recoil pressure forces may evoke the formation of keyholes and lead to spatter of melt drops or powder grains being ejected away [11, 17, 18]. This considerably affects the process stability in metal PBFAM, and thus, the quality of the solidified structural part. The formulation presented in [Paper B](#) [22] captures the motion and interaction of arbitrarily-shaped powder grains, the liquid melt phase, and a surrounding gas phase while undergoing reversible phase transitions in the form of melting and solidification. Accordingly, this formulation represents a useful extension of the formulation for mesoscale melt pool modeling [23] or other state-of-the-art approaches [111–114]. Such a combined approach is expected to become a powerful tool for detailed studies of melt pool thermo-hydrodynamics in metal PBFAM processes.

Modeling the digestion of food in the human stomach constitutes an emerging field of biomechanics [2] and requires to address several complex phenomena, such as gastric electrophysiology, solid mechanics of the gastric wall, and fluid mechanics of the digesta. However, coupling of all of these individual components to a comprehensive multiphysics model of the human stomach still remains open. Large scale in-silico analyses of digestion in the stomach are expected to give significant insights into gastric mechanics and allow conclusive studies of motility both in health and disease. A state-of-the-art review on multiphysics modeling of the human stomach is given, e.g., in [2]. Significant progress has been achieved considering the interplay of (gastric) electrophysiology and mechanics of the wall [6, 115–117]. Nevertheless, these coupled electromechanical models of the human stomach do not incorporate fluid mechanics of the digesta, thus, neglect its effect on the deformation of the gastric wall. To this end, an FSI formulation is presented in [Paper A](#) [21], which is deemed especially suitable for applications in biomechanics that are subject to large interface deformations, as they occur, e.g., during gastric peristalsis. Furthermore, it is known that gastric fluid mechanics plays an important role for modeling digestion of food in the human stomach. The digesta is characterized by a multiphasic nature consisting of gastric juice, chyme, and solid food boluses. The propagation of ACWs during gastric peristalsis initiates intragastric fluid motion, such as retroulsive flow [7–9] that fosters mechanical and chemical disintegration of food [5]. A valuable tool to model the digesta in the human stomach is proposed in [Paper B](#) [22]. Herein, disintegration of food boluses is modeled in a first phenomenological approach considering chemically-induced phase transitions based on a concentration field, which resembles moisture penetration. The employed model does not explicitly resolve the influence of chemical and mechanical breakdown, however, an extension is possible in a straightforward manner. Altogether, capturing gastric electrophysiology, solid mechanics of the gastric wall, and fluid mechanics of the digesta in a comprehensive multiphysics model of the human stomach remains part of ongoing research and marks a significant milestone toward a better understanding of the digestion processes in the human gastrointestinal tract.

To conclude, efficient computational methods for multiphysics problems using SPH and the FEM are presented in this cumulative thesis. Of the numerous possible applications of the developed framework in engineering and biomechanics, mesoscale melt pool modeling in metal PBFAM and the digestion of food in the stomach have been chosen as exemplary problems. This thesis lays the groundwork for more sophisticated studies on these phenomena, or for a transfer of the methods to other highly relevant questions in multiphysics applications.

Bibliography

- [1] D. E. Keyes, L. C. McInnes, C. Woodward, W. Gropp, E. Myra, M. Pernice, J. Bell, J. Brown, A. Clo, J. Connors, et al. Multiphysics simulations: Challenges and opportunities. *The International Journal of High Performance Computing Applications*, 27(1):4–83, 2013.
- [2] S. Brandstaeter, S. L. Fuchs, R. C. Aydin, and C. J. Cyron. Mechanics of the stomach: A review of an emerging field of biomechanics. *GAMM-Mitteilungen*, 42(3):e201900001, 2019.
- [3] P. Janssen, S. Verschueren, H. Giao Ly, R. Vos, L. Van Oudenhove, and J. Tack. Intragastic pressure during food intake: a physiological and minimally invasive method to assess gastric accommodation. *Neurogastroenterology & Motility*, 23(4):316–e154, 2011.
- [4] E. A. Klausner, E. Lavy, M. Friedman, and A. Hoffman. Expandable gastroretentive dosage forms. *Journal of controlled release*, 90(2):143–162, 2003.
- [5] M. J. Ferrua, F. Kong, and R. P. Singh. Computational modeling of gastric digestion and the role of food material properties. *Trends in Food Science & Technology*, 22(9):480–491, 2011.
- [6] S. Brandstaeter, A. Gizzi, S. L. Fuchs, A. M. Gebauer, R. C. Aydin, and C. J. Cyron. Computational model of gastric motility with active-strain electromechanics. *ZAMM-Journal of Applied Mathematics and Mechanics/Zeitschrift für Angewandte Mathematik und Mechanik*, 98(12):2177–2197, 2018.
- [7] A. Pal, K. Indireskumar, W. Schwizer, B. Abrahamsson, M. Fried, and J. G. Brasseur. Gastric flow and mixing studied using computer simulation. *Proceedings of the Royal Society of London. Series B: Biological Sciences*, 271(1557):2587–2594, 2004.
- [8] F. Kong and R. P. Singh. Disintegration of solid foods in human stomach. *Journal of Food Science*, 73(5):R67–R80, 2008.
- [9] M. J. Ferrua, Z. Xue, and R. P. Singh. On the kinematics and efficiency of advective mixing during gastric digestion—A numerical analysis. *Journal of Biomechanics*, 47(15):3664–3673, 2014.
- [10] K. Indireskumar, J. G. Brasseur, H. Faas, G. S. Hebbard, P. Kunz, J. Dent, C. Feinle, M. Li, P. Boesiger, M. Fried, et al. Relative contributions of “pressure pump” and “peristaltic pump” to gastric emptying. *American Journal of Physiology-Gastrointestinal and Liver Physiology*, 278(4):G604–G616, 2000.

- [11] C. Meier, R. W. Penny, Y. Zou, J. S. Gibbs, and A. J. Hart. Thermophysical phenomena in metal additive manufacturing by selective laser melting: fundamentals, modeling, simulation, and experimentation. *Annual Review of Heat Transfer*, 20, 2017.
- [12] C. Meier, S. L. Fuchs, N. Much, J. Nitzler, R. W. Penny, P. M. Praegla, S. D. Pröll, Y. Sun, R. Weissbach, M. Schreter, N. E. Hodge, A. J. Hart, and W. A. Wall. Physics-Based Modeling and Predictive Simulation of Powder Bed Fusion Additive Manufacturing Across Length Scales. *GAMM-Mitteilungen*, 44(3):e202100014, 2021.
- [13] M. Markl and C. Körner. Multiscale modeling of powder bed-based additive manufacturing. *Annual Review of Materials Research*, 46:93–123, 2016.
- [14] C. Körner, E. Attar, and P. Heintl. Mesoscopic simulation of selective beam melting processes. *Journal of Materials Processing Technology*, 211(6):978–987, 2011.
- [15] C. Körner, A. Bauereiß, and E. Attar. Fundamental consolidation mechanisms during selective beam melting of powders. *Modelling and Simulation in Materials Science and Engineering*, 21(8):085011, 2013.
- [16] A. V. Gusarov, I. Yadroitsev, P. Bertrand, and I. Smurov. Heat transfer modelling and stability analysis of selective laser melting. *Applied Surface Science*, 254(4):975–979, 2007.
- [17] S. A. Khairallah, A. T. Anderson, A. Rubenchik, and W. E. King. Laser powder-bed fusion additive manufacturing: Physics of complex melt flow and formation mechanisms of pores, spatter, and denudation zones. *Acta Materialia*, 108:36–45, 2016.
- [18] Y. Liu, S. Li, H. Wang, W. Hou, Y. Hao, R. Yang, T. Sercombe, and L. C. Zhang. Microstructure, defects and mechanical behavior of beta-type titanium porous structures manufactured by electron beam melting and selective laser melting. *Acta Materialia*, 113:56–67, 2016.
- [19] R. A. Gingold and J. J. Monaghan. Smoothed particle hydrodynamics: theory and application to non-spherical stars. *Monthly Notices of the Royal Astronomical Society*, 181(3):375–389, 1977.
- [20] L. B. Lucy. A numerical approach to the testing of the fission hypothesis. *The Astronomical Journal*, 82:1013–1024, 1977.
- [21] S. L. Fuchs, C. Meier, W. A. Wall, and C. J. Cyron. A novel smoothed particle hydrodynamics and finite element coupling scheme for fluid-structure interaction: The sliding boundary particle approach. *Computer Methods in Applied Mechanics and Engineering*, 383:113922, 2021.
- [22] S. L. Fuchs, C. Meier, W. A. Wall, and C. J. Cyron. An SPH framework for fluid-solid and contact interaction problems including thermo-mechanical coupling and reversible phase transitions. *Advanced Modeling and Simulation in Engineering Sciences*, 8(1):15, 2021.

-
- [23] C. Meier, S. L. Fuchs, A. J. Hart, and W. A. Wall. A novel smoothed particle hydrodynamics formulation for thermo-capillary phase change problems with focus on metal additive manufacturing melt pool modeling. *Computer Methods in Applied Mechanics and Engineering*, 381:113812, 2021.
- [24] *BACI: A Comprehensive Multi-Physics Simulation Framework*, accessed February 25, 2021. URL: <https://baci.pages.gitlab.lrz.de/website>.
- [25] W. Benz. Smooth Particle Hydrodynamics: A Review. *The Numerical Modelling of Nonlinear Stellar Pulsations*, pages 269–288, 1990.
- [26] G.-R. Liu and M. B. Liu. *Smoothed Particle Hydrodynamics: a meshfree particle method*. World scientific, 2003.
- [27] J. J. Monaghan. Smoothed particle hydrodynamics. *Reports on Progress in Physics*, 68(8):1703, 2005.
- [28] M. B. Liu and G.-R. Liu. Smoothed particle hydrodynamics (SPH): an overview and recent developments. *Archives of Computational Methods in Engineering*, 17(1):25–76, 2010.
- [29] D. J. Price. Smoothed particle hydrodynamics and magnetohydrodynamics. *Journal of Computational Physics*, 231(3):759–794, 2012.
- [30] J. J. Monaghan. Smoothed particle hydrodynamics and its diverse applications. *Annual Review of Fluid Mechanics*, 44:323–346, 2012.
- [31] N. J. Quinlan, M. Basa, and M. Lastiwka. Truncation error in mesh-free particle methods. *International Journal for Numerical Methods in Engineering*, 66(13):2064–2085, 2006.
- [32] M. B. Liu, G.-R. Liu, and K. Lam. Constructing smoothing functions in smoothed particle hydrodynamics with applications. *Journal of Computational and Applied Mathematics*, 155(2):263–284, 2003.
- [33] J. P. Morris, P. J. Fox, and Y. Zhu. Modeling low Reynolds number incompressible flows using SPH. *Journal of Computational Physics*, 136(1):214–226, 1997.
- [34] J. Hongbin and D. Xin. On criteria for smoothed particle hydrodynamics kernels in stable field. *Journal of Computational Physics*, 202(2):699–709, 2005.
- [35] L. D. Libersky, A. G. Petschek, T. C. Carney, J. R. Hipp, and F. A. Allahdadi. High strain Lagrangian hydrodynamics: a three-dimensional SPH code for dynamic material response. *Journal of Computational Physics*, 109(1):67–75, 1993.
- [36] J. J. Monaghan. Smoothed particle hydrodynamics. *Annual Review of Astronomy and Astrophysics*, 30(1):543–574, 1992.
- [37] J. J. Monaghan. Simulating free surface flows with SPH. *Journal of Computational Physics*, 110(2):399–406, 1994.

- [38] T. Belytschko, Y. Krongauz, J. Dolbow, and C. Gerlach. On the completeness of mesh-free particle methods. *International Journal for Numerical Methods in Engineering*, 43(5):785–819, 1998.
- [39] A. Colagrossi and M. Landrini. Numerical simulation of interfacial flows by smoothed particle hydrodynamics. *Journal of Computational Physics*, 191(2):448–475, 2003.
- [40] S. Adami, X. Y. Hu, and N. A. Adams. A generalized wall boundary condition for smoothed particle hydrodynamics. *Journal of Computational Physics*, 231(21):7057–7075, 2012.
- [41] S. Adami, X. Y. Hu, and N. A. Adams. A transport-velocity formulation for smoothed particle hydrodynamics. *Journal of Computational Physics*, 241:292–307, 2013.
- [42] M. Basa, N. J. Quinlan, and M. Lastiwka. Robustness and accuracy of SPH formulations for viscous flow. *International Journal for Numerical Methods in Fluids*, 60(10):1127–1148, 2009.
- [43] J. J. Monaghan and J. B. Kajtár. SPH particle boundary forces for arbitrary boundaries. *Computer Physics Communications*, 180(10):1811–1820, 2009.
- [44] H. Takeda, S. M. Miyama, and M. Sekiya. Numerical simulation of viscous flow by smoothed particle hydrodynamics. *Progress of Theoretical Physics*, 92(5):939–960, 1994.
- [45] P. W. Randles and L. D. Libersky. Smoothed particle hydrodynamics: some recent improvements and applications. *Computer Methods in Applied Mechanics and Engineering*, 139(1-4):375–408, 1996.
- [46] S. Kulasegaram, J. Bonet, R. W. Lewis, and M. Profit. A variational formulation based contact algorithm for rigid boundaries in two-dimensional SPH applications. *Computational Mechanics*, 33(4):316–325, 2004.
- [47] M. Ferrand, D. R. Laurence, B. D. Rogers, D. Violeau, and C. Kassiotis. Unified semi-analytical wall boundary conditions for inviscid, laminar or turbulent flows in the meshless SPH method. *International Journal for Numerical Methods in Fluids*, 71(4):446–472, 2013.
- [48] A. Mayrhofer, M. Ferrand, C. Kassiotis, D. Violeau, and F.-X. Morel. Unified semi-analytical wall boundary conditions in SPH: analytical extension to 3-D. *Numerical Algorithms*, 68(1):15–34, 2015.
- [49] L. Chiron, M. De Leffe, G. Oger, and D. Le Touzé. Fast and accurate SPH modelling of 3D complex wall boundaries in viscous and non viscous flows. *Computer Physics Communications*, 234:93–111, 2019.
- [50] F. Macia, M. Antuono, L. M. González, and A. Colagrossi. Theoretical analysis of the no-slip boundary condition enforcement in SPH methods. *Progress of Theoretical Physics*, 125(6):1091–1121, 2011.

-
- [51] A. Valizadeh and J. J. Monaghan. A study of solid wall models for weakly compressible SPH. *Journal of Computational Physics*, 300:5–19, 2015.
- [52] T. Ye, D. Pan, C. Huang, and M. Liu. Smoothed particle hydrodynamics (SPH) for complex fluid flows: Recent developments in methodology and applications. *Physics of Fluids*, 31(1):011301, 2019.
- [53] M. Lastiwka, M. Basa, and N. J. Quinlan. Permeable and non-reflecting boundary conditions in SPH. *International Journal for Numerical Methods in Fluids*, 61(7):709–724, 2009.
- [54] C. E. Alvarado-Rodríguez, J. Klapp, L. D. G. Sigalotti, J. M. Domínguez, and E. de la Cruz Sánchez. Nonreflecting outlet boundary conditions for incompressible flows using SPH. *Computers & Fluids*, 159:177–188, 2017.
- [55] M. Ferrand, A. Joly, C. Kassiotis, D. Violeau, A. Leroy, F.-X. Morel, and B. D. Rogers. Unsteady open boundaries for SPH using semi-analytical conditions and Riemann solver in 2D. *Computer Physics Communications*, 210:29–44, 2017.
- [56] A. Monteleone, M. Monteforte, and E. Napoli. Inflow/outflow pressure boundary conditions for smoothed particle hydrodynamics simulations of incompressible flows. *Computers & Fluids*, 159:9–22, 2017.
- [57] L. Verlet. Computer "experiments" on classical fluids. I. Thermodynamical properties of Lennard-Jones molecules. *Physical Review*, 159(1):98–103, 1967.
- [58] B. J. Leimkuhler, S. Reich, and R. D. Skeel. Integration methods for molecular dynamics. In *Mathematical Approaches to biomolecular structure and dynamics*, pages 161–185. Springer, 1996.
- [59] O. C. Zienkiewicz, R. L. Taylor, and J. Z. Zhu. *The finite element method: its basis and fundamentals*. Elsevier, 2005.
- [60] O. C. Zienkiewicz and R. L. Taylor. *The finite element method for solid and structural mechanics*. Elsevier, 2005.
- [61] P. Wriggers. *Nonlinear finite element methods*. Springer Science & Business Media, 2008.
- [62] T. Belytschko, W. K. Liu, B. Moran, and K. Elkhodary. *Nonlinear Finite Elements for Continua and Structures*. John Wiley & Sons, 2013.
- [63] S. Gupta. Computing aspects of molecular dynamics simulation. *Computer Physics Communications*, 70(2):243–270, 1992.
- [64] T. W. Clark, R. Von Hanxleden, J. A. McCammon, and L. R. Scott. Parallelizing molecular dynamics using spatial decomposition. In *Proceedings of IEEE Scalable High Performance Computing Conference*, pages 95–102. IEEE, 1994.

- [65] S. Plimpton. Fast parallel algorithms for short-range molecular dynamics. *Journal of Computational Physics*, 117(1):1–19, 1995.
- [66] J. R. Williams and R. O’Connor. Discrete element simulation and the contact problem. *Archives of Computational Methods in Engineering*, 6(4):279–304, 1999.
- [67] T. Pöschel and T. Schwager. *Computational granular dynamics: models and algorithms*. Springer Science & Business Media, 2005.
- [68] D. Darmana, N. G. Deen, and J. Kuipers. Parallelization of an Euler–Lagrange model using mixed domain decomposition and a mirror domain technique: Application to dispersed gas–liquid two-phase flow. *Journal of Computational Physics*, 220(1):216–248, 2006.
- [69] M. P. Allen and D. J. Tildesley. *Computer Simulation of Liquids*. Oxford University Press, 2017.
- [70] G. Oger, D. Le Touzé, D. Guibert, M. De Leffe, J. Biddiscombe, J. Soumagne, and J.-G. Piccinalli. On distributed memory MPI-based parallelization of SPH codes in massive HPC context. *Computer Physics Communications*, 200:1–14, 2016.
- [71] J. M. Domínguez, A. J. Crespo, M. Gómez-Gesteira, and J.-C. Marongiu. Neighbour lists in smoothed particle hydrodynamics. *International Journal for Numerical Methods in Fluids*, 67(12):2026–2042, 2011.
- [72] M. Furuichi and D. Nishiura. Iterative load-balancing method with multigrid level relaxation for particle simulation with short-range interactions. *Computer Physics Communications*, 219:135–148, 2017.
- [73] L. Clarke, I. Glendinning, and R. Hempel. The MPI message passing interface standard. In *Programming environments for massively parallel distributed systems*, pages 213–218. Springer, 1994.
- [74] E. Gabriel, G. E. Fagg, G. Bosilca, T. Angskun, J. J. Dongarra, J. M. Squyres, V. Sahay, P. Kambadur, B. Barrett, A. Lumsdaine, et al. Open MPI: Goals, concept, and design of a next generation MPI implementation. In *European Parallel Virtual Machine/Message Passing Interface Users’ Group Meeting*, pages 97–104. Springer, 2004.
- [75] M. A. Heroux, R. A. Bartlett, V. E. Howle, R. J. Hoekstra, J. J. Hu, T. G. Kolda, R. B. Lehoucq, K. R. Long, R. P. Pawlowski, E. T. Phipps, et al. An overview of the Trilinos project. *ACM Transactions on Mathematical Software (TOMS)*, 31(3):397–423, 2005.
- [76] M. A. Heroux and J. M. Willenbring. A new overview of the Trilinos project. *Scientific Programming*, 20(2):83–88, 2012.
- [77] K. D. Devine, E. G. Boman, R. T. Heaphy, B. Hendrickson, and C. Vaughan. Zoltan data management services for parallel dynamic applications. *Computing in Science & Engineering*, 4(2):90–96, 2002.

- [78] E. G. Boman, Ü. V. Çatalyürek, C. Chevalier, and K. D. Devine. The Zoltan and Isoropia parallel toolkits for combinatorial scientific computing: Partitioning, ordering and coloring. *Scientific Programming*, 20(2):129–150, 2012.
- [79] P. A. Cundall and O. D. Strack. A discrete numerical model for granular assemblies. *geotechnique*, 29(1):47–65, 1979.
- [80] Y. Bashir and J. D. Goddard. A novel simulation method for the quasi-static mechanics of granular assemblages. *Journal of Rheology*, 35(5):849–885, 1991.
- [81] H. Zhu, Z. Zhou, R. Yang, and A. Yu. Discrete particle simulation of particulate systems: theoretical developments. *Chemical Engineering Science*, 62(13):3378–3396, 2007.
- [82] H. Zhu, Z. Zhou, R. Yang, and A. Yu. Discrete particle simulation of particulate systems: a review of major applications and findings. *Chemical Engineering Science*, 63(23):5728–5770, 2008.
- [83] D. C. Rapaport. *The Art of Molecular Dynamics Simulation*. Cambridge University Press, 2004.
- [84] P. Hoogerbrugge and J. M. V. A. K. Koelman. Simulating microscopic hydrodynamic phenomena with dissipative particle dynamics. *EPL (Europhysics Letters)*, 19(3):155, 1992.
- [85] R. D. Groot and P. B. Warren. Dissipative particle dynamics: Bridging the gap between atomistic and mesoscopic simulation. *The Journal of Chemical Physics*, 107(11):4423–4435, 1997.
- [86] M. J. Berger and S. H. Bokhari. A partitioning strategy for nonuniform problems on multiprocessors. *IEEE Computer Architecture Letters*, 36(05):570–580, 1987.
- [87] K. D. Devine, E. G. Boman, R. T. Heaphy, R. H. Bisseling, and U. V. Catalyurek. Parallel hypergraph partitioning for scientific computing. In *Proceedings 20th IEEE International Parallel & Distributed Processing Symposium*, pages 10–pp. IEEE, 2006.
- [88] U. V. Catalyurek, E. G. Boman, K. D. Devine, D. Bozdağ, R. T. Heaphy, and L. A. Riesen. A repartitioning hypergraph model for dynamic load balancing. *Journal of Parallel and Distributed Computing*, 69(8):711–724, 2009.
- [89] U. Ghia, K. N. Ghia, and C. Shin. High-Re solutions for incompressible flow using the Navier-Stokes equations and a multigrid method. *Journal of Computational Physics*, 48(3):387–411, 1982.
- [90] R. Schreiber and H. B. Keller. Driven cavity flows by efficient numerical techniques. *Journal of Computational Physics*, 49(2):310–333, 1983.
- [91] O. C. Zienkiewicz, R. L. Taylor, and P. Nithiarasu. *The finite element method for fluid dynamics*. Elsevier, 2006.

- [92] S. J. Cummins and M. Rudman. An SPH projection method. *Journal of Computational Physics*, 152(2):584–607, 1999.
- [93] E. Yang, H. H. Bui, H. De Sterck, G. D. Nguyen, and A. Bouazza. A scalable parallel computing SPH framework for predictions of geophysical granular flows. *Computers and Geotechnics*, 121:103474, 2020.
- [94] U. Küttler and W. A. Wall. Fixed-point fluid–structure interaction solvers with dynamic relaxation. *Computational Mechanics*, 43(1):61–72, 2008.
- [95] P. Causin, J.-F. Gerbeau, and F. Nobile. Added-mass effect in the design of partitioned algorithms for fluid–structure problems. *Computer Methods in Applied Mechanics and Engineering*, 194(42-44):4506–4527, 2005.
- [96] C. Förster, W. A. Wall, and E. Ramm. Artificial added mass instabilities in sequential staggered coupling of nonlinear structures and incompressible viscous flows. *Computer Methods in Applied Mechanics and Engineering*, 196(7):1278–1293, 2007.
- [97] M. Schäfer, S. Turek, F. Durst, E. Krause, and R. Rannacher. Benchmark computations of laminar flow around a cylinder. In *Flow Simulation with High-Performance Computers II*, pages 547–566. Springer, 1996.
- [98] S. Turek and J. Hron. Proposal for numerical benchmarking of fluid-structure interaction between an elastic object and laminar incompressible flow. In *Fluid-Structure Interaction*, pages 371–385. Springer, 2006.
- [99] M. Müller, S. Schirm, and M. Teschner. Interactive blood simulation for virtual surgery based on smoothed particle hydrodynamics. *Technology and Health Care*, 12(1):25–31, 2004.
- [100] T. Yamaguchi, T. Ishikawa, Y. Imai, N. Matsuki, M. Xenos, Y. Deng, and D. Bluestein. Particle-based methods for multiscale modeling of blood flow in the circulation and in devices: challenges and future directions. *Annals of Biomedical Engineering*, 38(3):1225–1235, 2010.
- [101] W. Mao, K. Li, and W. Sun. Fluid–structure interaction study of transcatheter aortic valve dynamics using smoothed particle hydrodynamics. *Cardiovascular Engineering and Technology*, 7(4):374–388, 2016.
- [102] M. Toma, D. R. Einstein, C. H. Bloodworth IV, R. P. Cochran, A. P. Yoganathan, and K. S. Kunzelman. Fluid–structure interaction and structural analyses using a comprehensive mitral valve model with 3D chordal structure. *International Journal for Numerical Methods in Biomedical Engineering*, 33(4):e2815, 2017.
- [103] A. Caballero, W. Mao, L. Liang, J. Oshinski, C. Primiano, R. McKay, S. Kodali, and W. Sun. Modeling left ventricular blood flow using smoothed particle hydrodynamics. *Cardiovascular Engineering and Technology*, 8(4):465–479, 2017.

- [104] M. D. Sinnott, P. W. Cleary, J. W. Arkwright, and P. G. Dinning. Investigating the relationships between peristaltic contraction and fluid transport in the human colon using Smoothed Particle Hydrodynamics. *Computers in Biology and Medicine*, 42(4):492–503, 2012.
- [105] M. D. Sinnott, P. W. Cleary, P. G. Dinning, J. W. Arkwright, and M. Costa. Interpreting manometric signals for propulsion in the gut. *Computational Particle Mechanics*, 2(3):273–282, 2015.
- [106] M. D. Sinnott, P. W. Cleary, and S. M. Harrison. Peristaltic transport of a particulate suspension in the small intestine. *Applied Mathematical Modelling*, 44:143–159, 2017.
- [107] S. M. Harrison, P. W. Cleary, and M. D. Sinnott. Investigating mixing and emptying for aqueous liquid content from the stomach using a coupled biomechanical-SPH model. *Food & Function*, 9(6):3202–3219, 2018.
- [108] H. Duckworth, D. J. Sharp, and M. Ghajari. Smoothed particle hydrodynamic modelling of the cerebrospinal fluid for brain biomechanics: Accuracy and stability. *International Journal for Numerical Methods in Biomedical Engineering*, 37(4):e3440, 2021.
- [109] M. Tong and D. J. Browne. An incompressible multi-phase smoothed particle hydrodynamics (SPH) method for modelling thermocapillary flow. *International Journal of Heat and Mass Transfer*, 73:284–292, 2014.
- [110] M. Hopp-Hirschler, M. S. Shadloo, and U. Nieken. A smoothed particle hydrodynamics approach for thermo-capillary flows. *Computers & Fluids*, 176:1–19, 2018.
- [111] M. A. Russell, A. Souto-Iglesias, and T. I. Zohdi. Numerical simulation of Laser Fusion Additive Manufacturing processes using the SPH method. *Computer Methods in Applied Mechanics and Engineering*, 341:163–187, 2018.
- [112] M. Trautmann, M. Hertel, and U. Füssel. Numerical simulation of weld pool dynamics using a SPH approach. *Welding in the World*, 62(5):1013–1020, 2018.
- [113] J. Weirather, V. Rozov, M. Wille, P. Schuler, C. Seidel, N. A. Adams, and M. F. Zaeh. A smoothed particle hydrodynamics model for laser beam melting of Ni-based alloy 718. *Computers & Mathematics with Applications*, 78(7):2377–2394, 2019.
- [114] J.-P. Fürstenau, H. Wessels, C. Weißenfels, and P. Wriggers. Generating virtual process maps of SLM using powder-scale SPH simulations. *Computational Particle Mechanics*, 7(4):655–677, 2020.
- [115] N. R. Akhmadeev and R. N. Miftahof. Stress-strain distribution in the human stomach. *Modelling in Medicine and Biology*, 5(2):90–107, 2010.
- [116] L. Klemm, R. Seydewitz, M. Borsdorf, T. Siebert, and M. Böl. On a coupled electro-chemomechanical model of gastric smooth muscle contraction. *Acta Biomaterialia*, 109:163–181, 2020.

- [117] A. Nitti, J. Kiendl, A. Gizzi, A. Reali, and M. D. de Tullio. A curvilinear isogeometric framework for the electromechanical activation of thin muscular tissues. *Computer Methods in Applied Mechanics and Engineering*, 382:113877, 2021.

A Full texts of publications

A.1 Paper A

A novel smoothed particle hydrodynamics and finite element coupling scheme for fluid-structure interaction: The sliding boundary particle approach

Sebastian L. Fuchs, Christoph Meier, Wolfgang A. Wall, Christian J. Cyron

Reprinted from S. L. Fuchs, C. Meier, W. A. Wall, and C. J. Cyron. A novel smoothed particle hydrodynamics and finite element coupling scheme for fluid-structure interaction: The sliding boundary particle approach. *Computer Methods in Applied Mechanics and Engineering*, 383:113922, 2021, licensed under the Creative Commons Attribution License 4.0 (<https://creativecommons.org/licenses/by/4.0/>).



ELSEVIER



Available online at www.sciencedirect.com

ScienceDirect

Comput. Methods Appl. Mech. Engrg. 383 (2021) 113922

Computer methods
in applied
mechanics and
engineering

www.elsevier.com/locate/cma

A novel smoothed particle hydrodynamics and finite element coupling scheme for fluid–structure interaction: The sliding boundary particle approach

Sebastian L. Fuchs^{a,b,*}, Christoph Meier^a, Wolfgang A. Wall^a, Christian J. Cyron^{b,c}

^a Institute for Computational Mechanics, Technical University of Munich, Boltzmannstraße 15, 85748, Garching, Germany

^b Institute of Continuum and Materials Mechanics, Hamburg University of Technology, Eißendorfer Straße 42, 21073, Hamburg, Germany

^c Institute of Material Systems Modeling, Helmholtz-Zentrum Hereon, Max-Planck-Straße 1, 21502 Geesthacht, Germany

Received 5 November 2020; received in revised form 8 May 2021; accepted 10 May 2021

Available online 1 June 2021

Abstract

A novel numerical formulation for solving fluid–structure interaction (FSI) problems is proposed where the fluid field is spatially discretized using smoothed particle hydrodynamics (SPH) and the structural field using the finite element method (FEM). As compared to fully mesh- or grid-based FSI frameworks, due to the Lagrangian nature of SPH this framework can be easily extended to account for more complex fluids consisting of multiple phases and dynamic phase transitions. Moreover, this approach facilitates the handling of large deformations of the fluid domain respectively the fluid–structure interface without additional methodological and computational efforts. In particular, to achieve an accurate representation of interaction forces between fluid particles and structural elements also for strongly curved interface geometries, the novel sliding boundary particle approach is proposed to ensure full support of SPH particles close to the interface. The coupling of the fluid and the structural field is based on a Dirichlet–Neumann partitioned approach, where the fluid field is the Dirichlet partition with prescribed interface displacements and the structural field is the Neumann partition subject to interface forces. To overcome instabilities inherent to weakly coupled schemes an iterative fixed-point coupling scheme is employed. Several numerical examples in form of well-known benchmark tests are considered to validate the accuracy, stability, and robustness of the proposed formulation. Finally, the filling process of a highly flexible thin-walled balloon-like container is studied, representing a model problem close to potential application scenarios of the proposed scheme in the field of biomechanics.

© 2021 The Authors. Published by Elsevier B.V. This is an open access article under the CC BY license (<http://creativecommons.org/licenses/by/4.0/>).

Keywords: Fluid–structure interaction; Smoothed particle hydrodynamics; Finite element method; Iterative Dirichlet–Neumann coupling; Large deformation; Incompressible flow

1. Introduction

In many applications in science and engineering fluid–structure interaction (FSI) phenomena play an essential role in modeling and simulation, in particular, in some areas of biomechanics, e.g., digestion of food in the human

* Corresponding author at: Institute for Computational Mechanics, Technical University of Munich, Boltzmannstraße 15, 85748, Garching, Germany.

E-mail addresses: fuchs@lmm.mw.tum.de (S.L. Fuchs), meier@lmm.mw.tum.de (C. Meier), wall@lmm.mw.tum.de (W.A. Wall), christian.cyron@tuhh.de (C.J. Cyron).

<https://doi.org/10.1016/j.cma.2021.113922>

0045-7825/© 2021 The Authors. Published by Elsevier B.V. This is an open access article under the CC BY license (<http://creativecommons.org/licenses/by/4.0/>).

stomach [1,2], referring to the authors target application. Besides the challenge to deal with large deformations of both fluid and structural domain, accurate modeling of fluid flow in biomechanics is even more demanding in the case of complex fluids including, e.g., multiple fluid phases and dynamic phase transitions (e.g. due to chemical reactions). Most current FSI frameworks utilize mesh- or grid-based methods, e.g., the finite element method (FEM), finite difference method (FDM), or finite volume method (FVM), which often require additional methodological and computational effort to capture the aforementioned phenomena. A promising approach to model complex fluids, e.g., the content of gastric lumen in the human stomach [1,2], is the method of smoothed particle hydrodynamics (SPH). SPH is a mesh-free discretization scheme that was originally and independently of one another introduced by Gingold and Monaghan [3] and Lucy [4] in 1977. While initially intended to study astrophysical problems, SPH gained increasing importance in other fields of computational fluid dynamics (CFD) since then. Due to its Lagrangian nature, SPH is very well suited for flow problems involving multiple phases, dynamic phase transitions, as well as complex interface topologies. Especially for many fluid–structure interaction scenarios in biomechanics it would therefore be desirable to discretize the fluid field with SPH whereas the solid field is often easier to handle with finite elements. To this end, a robust and efficient algorithm coupling SPH and FEM for the simulation of fluid–structure interactions is required.

On these grounds, this contribution proposes a novel numerical formulation for solving FSI problems where the fluid field is modeled using SPH and the structural field using FEM. Both sub-fields are coupled following a Dirichlet–Neumann partitioned approach. The fluid field is the Dirichlet partition with prescribed interface displacements or interface velocities, respectively, and the structural field is the Neumann partition subject to interface forces. That means, the interface forces are evaluated by the fluid solver utilizing the current interface displacements and interface velocities that are directly extracted from the structural field. Afterwards, the interface forces are applied to the structural solver enforcing conservation of linear momentum. An iterative fixed-point coupling scheme [5] is employed to satisfy dynamic equilibrium at the fluid–structure interface with respect to a predefined convergence criterion. This so-called strong coupling of both sub-fields is crucial to overcome instabilities, e.g., due to the artificial added mass effect, that are known to occur for weakly coupled schemes in FSI [6,7].

One focus of this work lies on the crucial aspect of the treatment of deformable and strongly curved boundaries of the SPH domain as especially required for many FSI applications. In the literature several different formulations for modeling (rigid) boundaries in SPH are proposed. Among them are penalty-like repulsive force formulations [8–10], ghost particle formulations [11], boundary particle methods based on fixed layers of particles resembling rigid walls [12,13], or semi-analytical methods considering non-vanishing surface integrals due to missing kernel support [14–16]. For an overview on the advantages and disadvantages of the aforementioned methods the interested reader is referred to the literature, e.g., in [17,18]. In principle, all those methods modeling rigid boundaries in SPH naturally have the potential to serve as a basis also for the treatment of flexible structural boundaries in the context of FSI problems [19–23]. However, FSI applications, especially in biomechanics, are characterized by large deformations at the fluid–structure interface including strong curvature and large stretch. This requires a special treatment of boundaries in order to prevent loss of accuracy at the fluid–structure interface. To the best of the authors' knowledge, the existing methods are either missing the required accuracy, computationally expensive, or not capable of modeling deforming interfaces undergoing strong curvature and large stretch. To address this shortcoming of existing approaches, the novel sliding boundary particle approach is proposed. It is based on a transient set of virtual boundary particles regularly arranged around the current projection point of a fluid particle onto the fluid domain boundary. Moreover, a generalized formulation for the extrapolation of field variables from fluid to virtual boundary particles is proposed, which is inspired by the procedure of [13].

The present publication is organized as follows: To begin with, the governing equations for FSI problems are briefly introduced in Section 2, followed by a detailed presentation of the numerical methods and the computational framework being utilized with a focus on the evaluation of the interface forces and the coupling scheme, cf. Section 3. Finally, numerical results obtained with the proposed novel numerical formulation for solving FSI problems are shown in Section 4. For validation purposes, well-known CFD respectively FSI benchmark tests are studied confirming the accuracy and robustness of the proposed formulation. This is followed by an application-motivated academic example examining the filling process of a highly flexible thin-walled container.

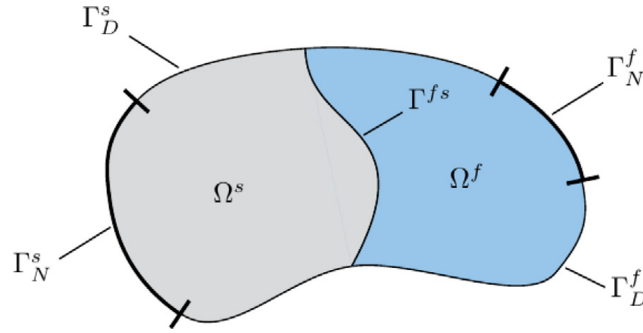


Fig. 1. Domain Ω of a fluid–structure interaction problem consisting of two disjunct sub-domains for the fluid field Ω^f and the structural field Ω^s with shared common interface Γ^{fs} .

2. Governing equations

At all times $t \in [0, T]$ the domain Ω of a fluid–structure interaction problem consists of a non-overlapping fluid domain Ω^f and a structural domain Ω^s that share a common interface Γ^{fs} , with $\Omega = \Omega^f \cup \Omega^s$ and $\Omega^f \cap \Omega^s = \Gamma^{fs}$, refer to Fig. 1. This leads to the so-called geometric coupling condition that restricts the fluid and structural domains to perfectly match without any holes or gaps at the fluid–structure interface Γ^{fs} . In the following, the (standard) governing equations of the fluid and structural field as well as the respective coupling condition for FSI are briefly given.

Remark 1. In Eqs. (1)–(2) governing the fluid field and (5) governing the structural field all time derivatives follow the motion of material points, i.e., the material derivative reads $\frac{d(\cdot)}{dt} = \frac{\partial(\cdot)}{\partial t} + \mathbf{u} \cdot \nabla(\cdot)$. Furthermore, $\nabla(\cdot)$ denotes within the setting of nonlinear continuum mechanics derivatives with respect to spatial coordinates while $\nabla_0(\cdot)$ denotes derivatives with respect to material coordinates.

2.1. Fluid field

The fluid field is governed by the instationary Navier–Stokes equations in the domain Ω^f in convective form consisting of the mass continuity equation and the momentum equation

$$\frac{d\rho^f}{dt} = -\rho^f \nabla \cdot \mathbf{u}^f \quad \text{in } \Omega^f, \quad (1)$$

$$\frac{d\mathbf{u}^f}{dt} = -\frac{1}{\rho^f} \nabla p^f + \mathbf{f}_v + \mathbf{b}^f \quad \text{in } \Omega^f, \quad (2)$$

with viscous force \mathbf{f}_v and body force \mathbf{b}^f each per unit mass. For a Newtonian fluid the viscous force is $\mathbf{f}_v = \nu^f \nabla^2 \mathbf{u}^f$ with kinematic viscosity ν^f . The mass continuity equation (1) and the momentum equation (2) represent a system of four equations with the five unknowns, velocity \mathbf{u}^f , density ρ^f , and pressure p^f . The system of equations is closed with an equation of state $p^f = p^f(\rho^f)$ relating fluid density ρ^f and pressure p^f , cf. Section 3.1.5. The Navier–Stokes equations (1) and (2) are subject to the following initial conditions

$$\rho^f = \rho_0^f \quad \text{and} \quad \mathbf{u}^f = \mathbf{u}_0^f \quad \text{in } \Omega^f \quad \text{at } t = 0 \quad (3)$$

with initial density ρ_0^f and initial velocity \mathbf{u}_0^f . In addition, Dirichlet and Neumann boundary conditions are applied on the fluid boundary $\Gamma^f = \partial\Omega^f \setminus \Gamma^{fs}$

$$\mathbf{u}^f = \hat{\mathbf{u}}^f \quad \text{on } \Gamma_D^f \quad \text{and} \quad \mathbf{t}^f = \hat{\mathbf{t}}^f \quad \text{on } \Gamma_N^f, \quad (4)$$

with prescribed boundary velocity $\hat{\mathbf{u}}^f$ and boundary traction $\hat{\mathbf{t}}^f$, where $\Gamma^f = \Gamma_D^f \cup \Gamma_N^f$ and $\Gamma_D^f \cap \Gamma_N^f = \emptyset$.

2.2. Structural field

Considering the regime of finite deformations, the structural field is governed by the balance of linear momentum in the following local material form

$$\rho_0^s \frac{d^2 \mathbf{d}^s}{dt^2} = \nabla_0 \cdot (\mathbf{FS}) + \rho_0^s \mathbf{b}_0^s \quad \text{in } \Omega^s \quad (5)$$

with the material forms of density ρ_0^s and body force \mathbf{b}_0^s , and the structural displacement \mathbf{d}^s as primary unknowns. The deformation of the structure is described by the deformation gradient $\mathbf{F} = \nabla_0 \mathbf{d}^s$ defining the Green–Lagrange strains $\mathbf{E} = \frac{1}{2}(\mathbf{F}^T \mathbf{F} - \mathbf{I})$. For simplicity, and as applicable and most often used in biomechanical problems, the second Piola–Kirchhoff stresses \mathbf{S} are chosen to follow from a constitutive relation of the form $\mathbf{S} = \partial \Psi / \partial \mathbf{E}$ based on a hyperelastic strain energy function $\Psi = \Psi(\mathbf{E})$. The partial differential equation (5) is subject to initial conditions for the structural displacement and velocity

$$\mathbf{d}^s = \mathbf{d}_0^s \quad \text{and} \quad \frac{d\mathbf{d}^s}{dt} = \frac{d\mathbf{d}_0^s}{dt} \quad \text{in } \Omega^s \quad \text{at } t = 0. \quad (6)$$

On the structural boundary $\Gamma^s = \partial \Omega^s \setminus \Gamma^{fs}$, Dirichlet and Neumann boundary conditions are prescribed

$$\mathbf{d}^s = \hat{\mathbf{d}}^s \quad \text{on } \Gamma_D^s \quad \text{and} \quad (\mathbf{FS}) \cdot \mathbf{N} = \hat{\mathbf{t}}_0^s \quad \text{on } \Gamma_N^s, \quad (7)$$

with prescribed boundary displacement $\hat{\mathbf{d}}^s$, boundary traction $\hat{\mathbf{t}}_0^s$, and outward pointing unit normal vector \mathbf{N} on Γ^s in material description, where $\Gamma^s = \Gamma_D^s \cup \Gamma_N^s$ and $\Gamma_D^s \cap \Gamma_N^s = \emptyset$.

2.3. Coupling conditions

A geometric coupling condition results from restricting both the fluid and structural domain to match at the fluid–structure interface Γ^{fs} as already described in the beginning of this section. In addition, the so-called kinematic coupling condition (or no-slip boundary condition) enforces a continuous fluid and structural velocity at the interface Γ^{fs} . Consequently, these two conditions can be expressed as

$$\mathbf{r}^f = \mathbf{r}^s \quad \text{and} \quad \mathbf{u}^f = \frac{d\mathbf{d}^s}{dt} \quad \text{on } \Gamma^{fs}, \quad (8)$$

with the current position \mathbf{r}^f respectively \mathbf{r}^s of the fluid and structural field. Finally, the dynamic coupling condition ensures equilibrium of fluid and structural traction across the interface Γ^{fs}

$$\mathbf{t}^f = \mathbf{t}^s \quad \text{on } \Gamma^{fs}. \quad (9)$$

3. Numerical methods and computational framework

The purpose of this section is to present the methods for discretization and numerical solution of the fluid–structure interaction problem as described in Section 2. The discretization of the fluid field is based on smoothed particle hydrodynamics while the discretization of the structural field is based on the finite element method, as illustrated in Fig. 2 (left).

While in Sections 3.1 and 3.2 the basics of these two methods are recapitulated, the focus of this publication is set on the specific evaluation of interaction forces, cf. Section 3.3, introducing the sliding boundary particle approach, and the employed coupling algorithm, cf. Section 3.4, in terms of underlying methods. The presented computational framework is implemented in the in-house parallel multiphysics research code BACI (Bavarian Advanced Computational Initiative) [24].

3.1. Discretization of fluid field via smoothed particle hydrodynamics

The fluid field governed by the instationary Navier–Stokes equations (1) and (2) is solved using smoothed particle hydrodynamics following a weakly compressible approach [9,17,25]. For modeling fluid flow using SPH, several different formulations each with its own characteristics and benefits can be derived as reflected by the vast amount of literature. The aim of this section is to give a brief introduction into the basics of SPH and an overview of the

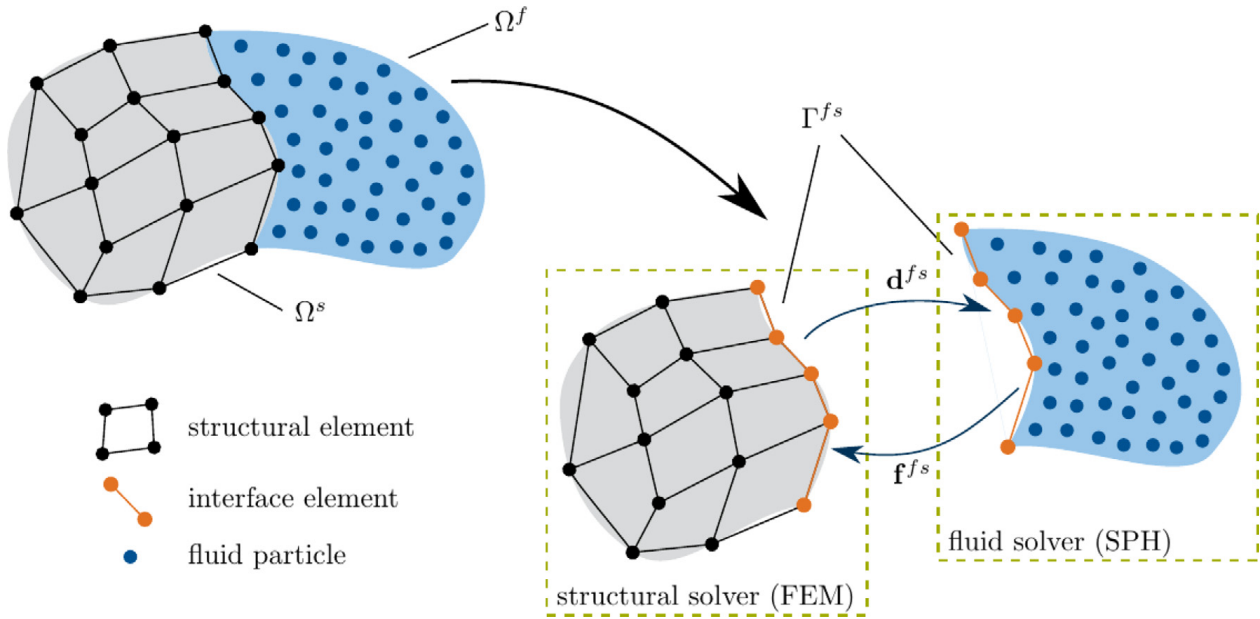


Fig. 2. Discretized domain Ω of a fluid–structure interaction problem with structural mesh and fluid particles (left) and separated sub-domains as seen by the fluid solver (SPH) and the structural solver (FEM) each with interface mesh for interaction handling and exchange of interface displacements \mathbf{d}^{fs} and interface forces \mathbf{f}^{fs} in the sense of a Dirichlet–Neumann partitioned coupling approach (right).

formulation applied throughout this work. Note that the contribution resulting from the coupling condition of the fluid and structural field at the interface Γ^{fs} , refer to Section 2.3, is omitted in this section and described in detail in Section 3.3. For ease of notation, in the following the index $(\cdot)^f$ denoting fluid quantities, as used in Section 2, is dropped.

3.1.1. Approximation of field quantities via smoothing kernel

The fundamental concept of SPH is based on the approximation of a field quantity f via a smoothing operation and on the discretization of the domain Ω with discretization points, so-called particles. To begin with, a field quantity f on a domain Ω can be expressed exactly in integral form as

$$f(\mathbf{r}) = \int_{\Omega} f(\mathbf{r}')\delta(|\mathbf{r} - \mathbf{r}'|) \, d\mathbf{r}' \tag{10}$$

making use of the Dirac delta function $\delta(r)$. Replacing the latter by a so-called smoothing kernel $W(r, h)$, that fulfills certain required properties, cf. Remark 2 and [17], leads to an approximation of the field quantity f in smoothed integral form

$$f(\mathbf{r}) \approx \int_{\Omega} f(\mathbf{r}')W(|\mathbf{r} - \mathbf{r}'|, h) \, d\mathbf{r}' \tag{11}$$

while committing a smoothing error.

Remark 2. The smoothing kernel $W(r, h)$ is a monotonically decreasing, smooth function that depends on a distance r and a smoothing length h . The smoothing length h together with a scaling factor κ define the support radius of the smoothing kernel $r_c = \kappa h$. Compact support, i.e., $W(r, h) = 0$ for $r > r_c$, as well as positivity, i.e., $W(r, h) \geq 0$ for $r \leq r_c$, are typical properties of standard smoothing kernels $W(r, h)$. In addition, the normalization property requires that $\int_{\Omega} W(|\mathbf{r} - \mathbf{r}'|, h) \, d\mathbf{r}' = 1$. The Dirac delta function property $\lim_{h \rightarrow 0} W(r, h) = \delta(r)$ ensures an exact representation of a field quantity f in the limit $h \rightarrow 0$.

In a next step, the computational domain Ω is filled with discretization points or so-called particles j , each occupying a volume V_j . Thus, the smoothed integral form of quantity f reduces in discretized form to a summation

of contributions from all particles j in the domain Ω , cf. [Remark 3](#),

$$f(\mathbf{r}) \approx \sum_j V_j f(\mathbf{r}_j) W(|\mathbf{r} - \mathbf{r}_j|, h) \quad (12)$$

adding a discretization error [26]. A straightforward approach in SPH to determine the gradient of a quantity f follows directly by differentiation of Eq. (12) resulting in

$$\nabla f(\mathbf{r}) \approx \sum_j V_j f(\mathbf{r}_j) \nabla W(|\mathbf{r} - \mathbf{r}_j|, h). \quad (13)$$

Note that this (simple) variant for an approximation of the gradient shows some particular disadvantages, hence, more advanced approximations for gradients are given in the literature [9] and also applied in this work [13,27], cf. Section 3.1.4.

Remark 3. In general, contributions from all particles in the domain Ω are considered in the SPH approximation of a field quantity f , cf. Eq. (12). However, note that in practice due to the compact support of the smoothing kernel W only neighboring particles within the support radius r_c need to be considered. This property is very beneficial as it reduces the computational effort of the method.

Applying the concept of SPH reduces the partial differential equations (1) and (2) to ordinary differential equations that are solved, i.e., evaluated and integrated in time, for all particles in the domain Ω (cf. Sections 3.1.4 and 3.1.7). The transient positions of particles are advected with the fluid velocity resembling the Lagrangian nature of the method. As a result, all fluid quantities are evaluated at and associated with particle positions, meaning each particle carries its corresponding fluid quantities.

Finally, in a post-processing step the continuous field quantity f is recovered from the discrete fluid quantities carried by each particle in the domain based on approximation (12) and the commonly known Shepard filter

$$\hat{f}(\mathbf{r}) \approx \frac{\sum_j V_j f(\mathbf{r}_j) W(|\mathbf{r} - \mathbf{r}_j|, h)}{\sum_j V_j W(|\mathbf{r} - \mathbf{r}_j|, h)}. \quad (14)$$

Note that the denominator typically takes on values close to one inside the fluid domain and is mainly relevant for boundary regions with reduced support due to a lack of neighboring particles.

Remark 4. In the following, a quantity f evaluated for particle i at position \mathbf{r}_i is written as $f_i = f(\mathbf{r}_i)$. In addition, the short notation $W_{ij} = W(r_{ij}, h)$ denotes the smoothing kernel W evaluated for particle i at position \mathbf{r}_i with neighboring particle j at position \mathbf{r}_j , where $r_{ij} = |\mathbf{r}_i - \mathbf{r}_j|$ is the absolute distance between particles i and j . Similarly, the derivative of the smoothing kernel W with respect to the absolute distance r_{ij} is denoted by $\partial W / \partial r_{ij} = \partial W(r_{ij}, h) / \partial r_{ij}$.

Remark 5. Herein, the smoothing of fluid quantities is carried out using a quintic spline smoothing kernel $W(r, h)$ as defined in [12] with smoothing length h and compact support of the smoothing kernel with support radius $r_c = \kappa h$ and scaling factor $\kappa = 3$.

3.1.2. Initial particle spacing

Within this contribution, the fluid domain is initially filled with particles located on a regular grid with particle spacing Δx , thus in a d -dimensional space each particle initially occupies an effective volume of $(\Delta x)^d$. The mass of a particle i is then set using the reference density according to $m_i = \rho_0 (\Delta x)^d$ and remains constant throughout the simulation. In general, the initial particle spacing Δx can be freely chosen, however, within this work the initial particle spacing Δx is set equal to the smoothing length $h = r_c / \kappa$.

3.1.3. Density summation

The density of a particle i is determined via summation of the respective smoothing kernel contributions of all neighboring particles j within the support radius r_c

$$\rho_i = m_i \sum_j W_{ij}. \quad (15)$$

This approach is typically denoted as density summation and results in an exact conservation of mass in the fluid domain, which can be shown in a straightforward manner considering the commonly applied normalization of the smoothing kernel to unity. It shall be noted that the density field may alternatively be obtained by discretization and integration of the mass continuity equation (1) [17].

3.1.4. Momentum equation

The momentum equation (2) is discretized following [13,27] including a transport velocity formulation to suppress the problem of tensile instability. It will be briefly recapitulated in the following. The transport velocity formulation relies on a constant background pressure p_b that is applied to all particles and results in a contribution to the particle accelerations for in general disordered particle distributions. However, these additional acceleration contributions vanish for particle distributions fulfilling the partition of unity, thus fostering these desirable configurations. For the sake of brevity, the definition of the modified advection velocity and the additional terms in the momentum equation from the aforementioned transport velocity formulation are not discussed in the following and the reader is kindly referred to the original publication [27]. Altogether, the acceleration $\mathbf{a}_i = \mathbf{u}_i/t$ of a particle i results from summation of all acceleration contributions due to interaction with neighboring particles j and a body force as

$$\mathbf{a}_i = \frac{1}{m_i} \sum_j (V_i^2 + V_j^2) \left[-\tilde{p}_{ij} \frac{\partial W}{\partial r_{ij}} \mathbf{e}_{ij} + \tilde{\eta}_{ij} \frac{\mathbf{u}_{ij}}{r_{ij}} \frac{\partial W}{\partial r_{ij}} \right] + \mathbf{b}_i, \quad (16)$$

with volume $V_i = m_i/\rho_i$ of particle i , unit vector $\mathbf{e}_{ij} = \mathbf{r}_i - \mathbf{r}_j/|\mathbf{r}_i - \mathbf{r}_j| = \mathbf{r}_{ij}/r_{ij}$ pointing from particle j to particle i , relative velocity $\mathbf{u}_{ij} = \mathbf{u}_i - \mathbf{u}_j$, density-weighted inter-particle averaged pressure

$$\tilde{p}_{ij} = \frac{\rho_j p_i + \rho_i p_j}{\rho_i + \rho_j}, \quad (17)$$

and inter-particle averaged dynamic viscosity

$$\tilde{\eta}_{ij} = \frac{2\eta_i\eta_j}{\eta_i + \eta_j}. \quad (18)$$

In the following the acceleration contribution of a neighboring particle j to particle i is, for ease of notation, denoted as \mathbf{a}_{ij} , where $\mathbf{a}_i = \sum_j \mathbf{a}_{ij} + \mathbf{b}_i$. Note that the above given momentum formulation, cf. Eq. (16), exactly conserves linear momentum due to pairwise anti-symmetric particle forces

$$m_i \mathbf{a}_{ij} = -m_j \mathbf{a}_{ji}, \quad (19)$$

which can easily be verified by using the property $\partial W/\partial r_{ij} = \partial W/\partial r_{ji}$ of the smoothing kernel.

3.1.5. Equation of state

Following a weakly compressible approach, density ρ_i and pressure p_i of a particle i are linked via the equation of state

$$p_i(\rho_i) = c^2(\rho_i - \rho_0) = p_0 \left(\frac{\rho_i}{\rho_0} - 1 \right) \quad (20)$$

with reference density ρ_0 , reference pressure $p_0 = \rho_0 c^2$ and artificial speed of sound c . Note that this commonly applied approach only represents deviations from the reference pressure, i.e., $p_i(\rho_0) = 0$, and not the total pressure. Thus, free boundaries can be modeled by setting $p = 0$ (see also Section 3.1.6). To limit density fluctuations to an acceptable level, while still avoiding too severe time step restrictions, strategies are discussed in [12] on how to determine an appropriate value of the artificial speed of sound.

3.1.6. Boundary conditions

Rigid wall boundary conditions. Following the approach of [13], rigid wall boundary conditions are modeled using fixed boundary particles with quantities extrapolated from the fluid field based on a local force balance. For more details the interested reader is referred to the aforementioned literature. In the numerical examples in Section 4 the channel walls are modeled using rigid wall boundary conditions.

Inflow and outflow boundary conditions. Open boundaries are modeled similar to [28] via defined inflow and outflow zones occupying so-called inflow respectively outflow particles. Thereby, full support of the interior fluid particles is maintained for density summation (15) and evaluation of the momentum equation (16) when considering contributions from neighboring inflow and outflow particles. At the inflow, i.e., the Dirichlet boundary, the desired inflow velocity is prescribed directly to all inflow particles, while the pressure field is extrapolated from the interior fluid particles i to the inflow particles k following

$$p_k = \frac{\sum_i V_i p_i W_{ki}}{\sum_i V_i W_{ki}}. \quad (21)$$

At the outflow, i.e., the Neumann boundary, a zero pressure field is prescribed to all outflow particles. The density field of both inflow and outflow particles is determined from the pressure field with the equation of state (20). Finally, to determine consistent velocities of the outflow particles, the momentum equation (16) is evaluated for outflow particles considering interactions with neighboring fluid particles, boundary particles, and outflow particles.

Periodic boundary conditions. Imposing a periodic boundary condition in a specific spatial direction allows for particle interaction evaluation across opposite domain borders. Moreover, particles leaving the domain on one side are re-injecting on the opposite side. Periodic boundary conditions are commonly applied in SPH modeling of channel or shear flow.

3.1.7. Time integration scheme

The momentum equation (16) is integrated in time applying an explicit velocity-Verlet time integration scheme in kick–drift–kick form, also denoted as leapfrog scheme, as proposed by Monaghan [9]. In the absence of dissipative effects, the velocity-Verlet scheme is of second order accuracy and reversible in time [9].

In a first kick-step the particle accelerations $\mathbf{a}_i^n = (\mathbf{u}_i/t)^n$ determined in the previous time step n are used to compute intermediate particle velocities at $n + 1/2$

$$\mathbf{u}_i^{n+1/2} = \mathbf{u}_i^n + \frac{\Delta t}{2} \mathbf{a}_i^n, \quad (22)$$

where Δt is the time step size, before the particle positions at $n + 1$ are updated in a drift-step

$$\mathbf{r}_i^{n+1} = \mathbf{r}_i^n + \Delta t \mathbf{u}_i^{n+1/2}. \quad (23)$$

Using the particle positions \mathbf{r}_i^{n+1} and intermediate velocities $\mathbf{u}_i^{n+1/2}$, the particle densities ρ_i^{n+1} and accelerations \mathbf{a}_i^{n+1} are updated following Eqs. (15) and (16). In a final kick-step the particle velocities at $n + 1$ are determined

$$\mathbf{u}_i^{n+1} = \mathbf{u}_i^{n+1/2} + \frac{\Delta t}{2} \mathbf{a}_i^{n+1}. \quad (24)$$

To maintain stability of the time integration scheme, the time step size Δt is restricted by the Courant–Friedrichs–Lewy (CFL) condition, the viscous condition, and the body force condition, refer to [12,27] for more details,

$$\Delta t \leq \min \left\{ 0.25 \frac{h}{c + |\mathbf{u}_{max}|}, \quad 0.125 \frac{h^2}{\nu}, \quad 0.25 \sqrt{\frac{h}{|\mathbf{b}_{max}|}} \right\}, \quad (25)$$

with maximum fluid velocity \mathbf{u}_{max} and maximum body force \mathbf{b}_{max} .

3.2. Discretization of structural field via the finite element method

The discretization of the structural field, governed by the strong form of the balance of linear momentum (5), is based on the finite element method. Since it is not the focus of this work, the basics of the FEM are presented here only very briefly. For further informations the reader is referred to, e.g., [29,30].

Applying the method of weighted residuals, in the following interpreted as principle of virtual work, the weak form of the initial boundary value problem for the structural field is obtained as

$$\delta \mathcal{W}^s = \left(\delta \mathbf{d}^s, \rho_0^s \frac{d^2 \mathbf{d}^s}{dt^2} \right)_{\Omega^s} + (\nabla_0 \delta \mathbf{d}^s, \mathbf{FS})_{\Omega^s} - (\delta \mathbf{d}^s, \rho_0^s \mathbf{b}_0^s)_{\Omega^s} - (\delta \mathbf{d}^s, \hat{\mathbf{t}}_0^s)_{\Gamma_N^s} = 0 \quad (26)$$

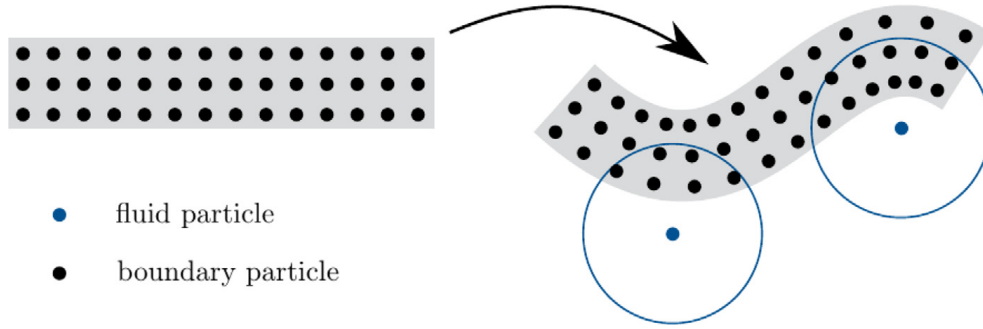


Fig. 3. A structural domain initially discretized by a regular and equidistant set of boundary particles fixed to material points of the structure (left) undergoing strong curvature and large stretch (right). Clearly, the support of the smoothing kernel of fluid particles close to regions of large structural displacements is disturbed.

with the variation $\delta \mathbf{d}^s$ of the primary unknown structural displacement \mathbf{d}^s . Herein, the contribution to the weak form resulting from the coupling condition of the fluid and structural field at the interface Γ^{fs} (cf. Section 2.3) is omitted and instead treated in Section 3.3.

By introducing the trial space $\mathcal{V} = \{\mathbf{d}^s \mid \mathbf{d}^s \in \mathcal{H}^1, \mathbf{d}^s = \hat{\mathbf{d}}^s \text{ on } \Gamma_D^s\}$ as well as the test space $\mathcal{W} = \{\delta \mathbf{d}^s \mid \delta \mathbf{d}^s \in \mathcal{H}^1, \delta \mathbf{d}^s = 0 \text{ on } \Gamma_D^s\}$, where \mathcal{H}^1 denotes the Sobolev space of functions with square-integrable first derivatives, the weak form (26) is equivalent to the strong form of the balance of linear momentum (5).

The computational domain of the structural field Ω^s is sub-divided into non-overlapping finite elements with nodes i . Hence, the structural displacement field \mathbf{d}^s is discretized introducing nodal displacements \mathbf{d}_i^s of nodes i . The displacement field is approximated via

$$\mathbf{d}^s(\mathbf{r}) \approx \sum_j N_j^e(\mathbf{r}) \mathbf{d}_j^s \quad (27)$$

using the Lagrange polynomials N_j^e with compact support inside element e . Within a Bubnov–Galerkin approach, the same Lagrange polynomials for trial and test functions are employed. Following the iso-parametric concept, the parameter coordinates $\boldsymbol{\xi}$ used for the definition of the shape functions within a standard element geometry are mapped onto the physical coordinates applying the same shape functions also used for the displacement interpolation. Specifically, in the numerical examples in Section 4 finite elements based on first-order interpolation are employed.

Subsequently, the semi-discrete form is discretized in time applying a generalized-alpha time integration scheme. The resulting system of nonlinear equations in residual form is finally solved for the nodal structural displacements using a Newton–Raphson method.

3.3. SPH-FE interaction: a novel sliding boundary particle approach

In this section, a novel sliding boundary particle approach for the application in a fluid–structure interaction framework coupling SPH and FEM is proposed. In contrast to existing methods modeling boundaries in SPH, e.g., boundary particle methods, cf. Fig. 3, the proposed method can handle also deforming interfaces undergoing strong curvature and large stretch, as typical for some FSI applications especially in biomechanics, while keeping the computational costs at a reasonable level. The following is mainly concerned with the evaluation of the interface force \mathbf{f}^{fs} at the fluid–structure interface Γ^{fs} . The coupling of fluid and structural field following a Dirichlet–Neumann partitioned approach is subsequently described in Section 3.4.

3.3.1. Conforming interface mesh

Introducing an interface mesh on the fluid–structure interface Γ^{fs} allows for exchange of interface displacement \mathbf{d}^{fs} and interface force \mathbf{f}^{fs} between the fluid and the structural field, cf. Fig. 2, while keeping the fluid and structural solvers separated. For convenience, the interface mesh, which is purely introduced as one possibility to facilitate the displacement and load transfer between the solvers, can be chosen as an extraction or clone of the structural mesh at the fluid–structure interface Γ^{fs} . But the proposed approach also works for non-matching meshes.

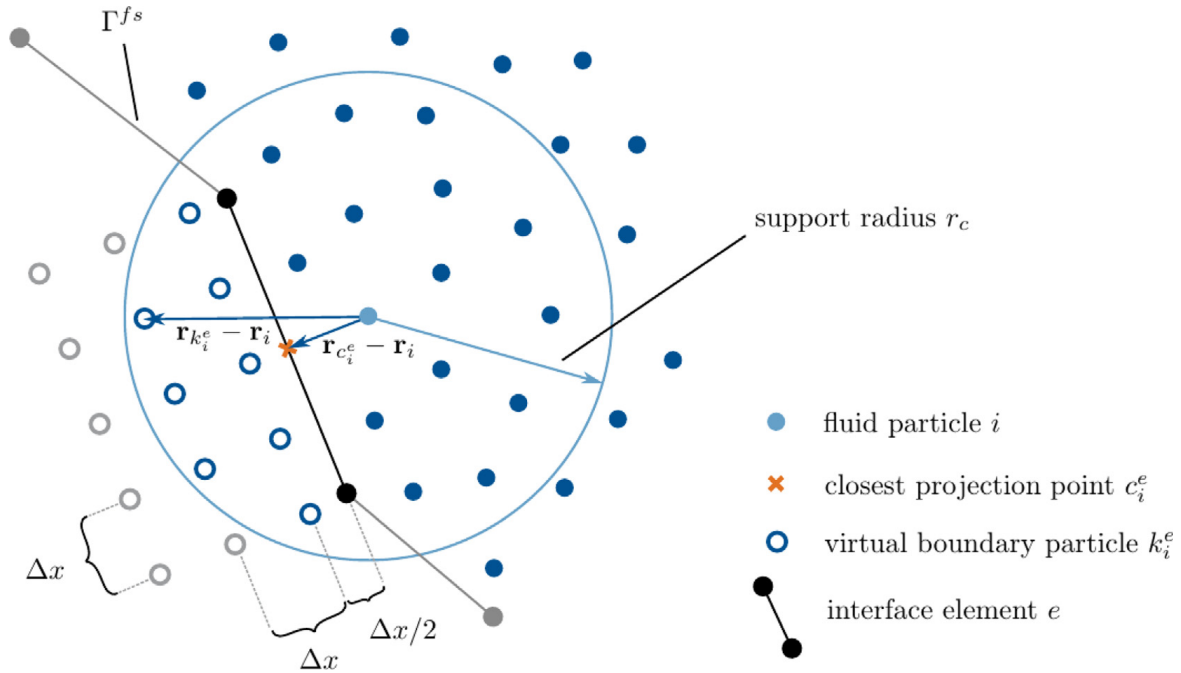


Fig. 4. Fluid particle i with closest projection point c_i^e to the interface Γ^{fs} on interface element e within support radius r_c of the smoothing kernel W and corresponding set of virtual boundary particles k_i^e associated with fluid particle i and ensuring full support of the smoothing kernel W .

For the interface mesh, again the iso-parametric concept is employed to describe the standard element geometry of interface elements e via parameter coordinates ξ and Lagrange polynomials N_j^e of corresponding nodes j . Note that for interface elements the parameter coordinates ξ are of one dimension lower compared to structural elements. Deduced from the geometric coupling condition (8) the current interface position is in the following depicted by \mathbf{r}^{fs} .

In case of a conforming mesh, the transfer of quantities between interface and structure is straightforward and is, hence, just briefly sketched here. Both, interface position \mathbf{r}^{fs} and interface displacement \mathbf{d}^{fs} can be extracted directly from the respective structural position \mathbf{r}^s and structural displacement \mathbf{d}^s . Similarly, the interface force \mathbf{f}^{fs} can be added directly to the respective structural force \mathbf{f}^s . In case non-matching interfaces are preferred or needed, e.g., because of special resolution demands of the two involved physical fields, the transfer of quantities between interface and structure could simply be done via a Mortar technique [31]. In comparison to the interface structure transfer, the transfer of quantities to the fluid field is more elaborate and will be covered in the following subsections.

3.3.2. Detection of closest projection point

The interaction evaluation is performed between fluid particles and interface elements. Consider a fluid particle i with support radius r_c of the smoothing kernel W that is close to the fluid–structure interface Γ^{fs} , cf. Fig. 4.

In general, the closest projection point c_i^e of fluid particle i to the interface Γ^{fs} is located on interface element e and lies within the support radius, i.e., $|\mathbf{r}_{c_i^e} - \mathbf{r}_i| < r_c$. The position $\mathbf{r}_{c_i^e}$ of point c_i^e can be described in iso-parametric coordinates $\xi_{c_i^e}$ on interface element e . As a result, the shape functions $N_j^e(\xi_{c_i^e})$ of all nodes j of interface element e evaluated at the closest projection point c_i^e can be utilized to interpolate kinematic quantities, e.g., positions, velocities, and accelerations, at the closest projection point using nodal quantities and to distribute kinetic quantities, e.g., interaction forces, from the closest projection point to adjacent nodes. The closest projection point c_i^e of a fluid particle i to a neighboring interface element e is detected solving the following minimization problem

$$|\mathbf{r}_{c_i^e} - \mathbf{r}_i| = \min_{\xi} \left| \sum_j N_j^e(\xi) \mathbf{r}_j^{fs} - \mathbf{r}_i \right| \tag{28}$$

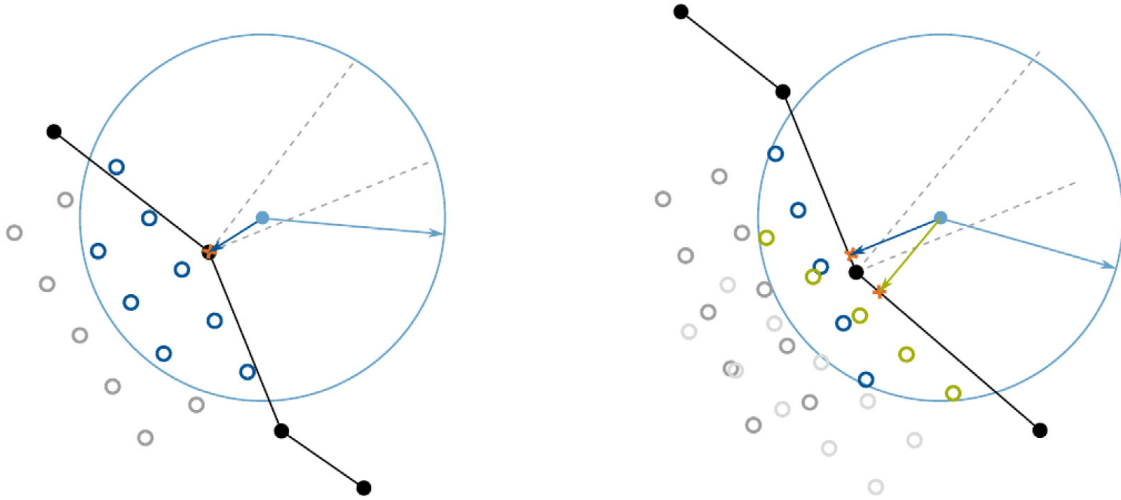


Fig. 5. Special cases of a convex angle (left) and a concave angle (right) between neighboring interface elements for the treatment of closest projection points of a fluid particle, cf. Remark 6 (legend similar to Fig. 4).

with position \mathbf{r}_i of fluid particle i and positions $\mathbf{r}_j^{f,s}$ of nodes j of interface element e . The solution of the minimization problem gives the iso-parametric coordinates $\xi_{c_i^e}$ of the closest projection point c_i^e on interface element e . Hence, the position of the closest projection point c_i^e results in

$$\mathbf{r}_{c_i^e} = \sum_j N_j^e(\xi_{c_i^e}) \mathbf{r}_j^{f,s}. \quad (29)$$

As stated above only closest projection points c_i^e located within the support radius of fluid particle i are considered in the interaction evaluation, meaning in addition $|\mathbf{r}_{c_i^e} - \mathbf{r}_i| < r_c$ must be fulfilled. By definition, when evolving the position of a fluid particle i over time, also the position of the closest projection point c_i^e is changing, i.e., is sliding on the interface $\Gamma^{f,s}$.

Remark 6. In the general case, the closest projection point of a particle is located on the surface of an interface element, as illustrated for instance in Fig. 4. In addition, the two special cases of a convex and a concave angle between two neighboring interface elements are worth being discussed here. In the case a particle is located within the perpendicular straight lines of neighboring interface elements at a convex angle, cf. Fig. 5 (left), a single closest projection point is considered that is located on the node respectively the edge being shared by those interface elements. For a particle located at a concave angle, cf. Fig. 5 (right), multiple closest projection points on the surface of each of the interface elements are considered.

Remark 7. Note that very similar to typical contact problems in finite element analysis an extension to a C^1 -continuous representation of the structural geometry, e.g., by employing Hermite polynomials [32] or B-Splines [33,34] as shape functions, could be beneficial within the proposed sliding boundary particle approach in terms of a smoother interaction force evolution and help to abstain from the aforementioned case distinctions, cf. Remark 6.

3.3.3. Virtual boundary particles

The support of the smoothing kernel of a fluid particle i close to the fluid–structure interface $\Gamma^{f,s}$ is truncated, i.e., fluid particle i experiences reduced contributions from neighboring fluid particles, cf. Fig. 4. To overcome this issue, full support of the smoothing kernel of fluid particle i is retained by considering a set of virtual boundary particles k_i^e that contribute to the interaction evaluation of fluid particle i and are regularly and equidistantly arranged behind the closest projection point c_i^e as illustrated in Fig. 4. This is achieved by a certain number of layers of virtual boundary particles with spacing Δx among them. Accordingly, together with the closest projection point c_i^e , the set of virtual boundary particles k_i^e are sliding along the fluid–structure interface $\Gamma^{f,s}$ following the movement of a fluid particle i , giving rise to the name of the proposed method: sliding boundary particle approach.

Remark 8. Within this work, as stated in Sections 3.1.1 and 3.1.2, a quintic spline smoothing kernel with support radius $r_c = 3h$ is applied with initial particle spacing Δx equal to the smoothing length h . As a consequence, three layers of virtual boundary particles are positioned behind the closest projection point c_i^e , thus, maintaining full support of the smoothing kernel W of fluid particle i , cf. Fig. 4.

All layers of virtual boundary particles are positioned perpendicular to the connection vector $\mathbf{r}_{c_i^e} - \mathbf{r}_i$ of fluid particle i and its closest projection point c_i^e , where the first layer is at a distance of $\Delta x/2$ behind the closest projection point c_i^e on interface element e . An orthonormal basis $(\mathbf{e}_r, \mathbf{e}_s, \mathbf{e}_t)$ with first base vector $\mathbf{e}_r = (\mathbf{r}_{c_i^e} - \mathbf{r}_i)/|\mathbf{r}_{c_i^e} - \mathbf{r}_i|$ is constructed [35]. Consequently, the position of all virtual boundary particles k_i^e can be given in terms of the particle spacing Δx and the constructed orthonormal basis $(\mathbf{e}_r, \mathbf{e}_s, \mathbf{e}_t)$ as

$$\mathbf{r}_{k_i^e} = \mathbf{r}_{c_i^e} + (m_r + 1/2) \Delta x \mathbf{e}_r + m_s \Delta x \mathbf{e}_s + m_t \Delta x \mathbf{e}_t \quad (30)$$

with integers $m_r \in \{0, 1, \dots, (q-1)\}$ and $m_s, m_t \in \{-(q-1), \dots, (q-1)\}$ where $q = \text{floor}(r_c/\Delta x)$ defines the number of particles necessary to maintain full support of the smoothing kernel. Finally, the vector from fluid particle i to virtual boundary particle k_i^e is $\mathbf{r}_{k_i^e} - \mathbf{r}_i$, cf. Fig. 4.

Remark 9. The floor operator used herein is defined by $\text{floor}(x) := \max\{k \in \mathbb{Z} \mid k \leq x\}$ and returns the largest integer that is less than or equal to its argument x .

3.3.4. Interaction forces on fluid particles

A fluid particle i close to the fluid–structure interface Γ^{fs} , i.e., for which the closest projection point c_i^e on interface element e is within the support radius $|\mathbf{r}_{c_i^e} - \mathbf{r}_i| < r_c$ of fluid particle i , additionally experiences contributions to the density summation (15) and the momentum evaluation (16) from all virtual boundary particles k_i^e for which $|\mathbf{r}_{k_i^e} - \mathbf{r}_i| < r_c$ holds, cf. Fig. 4.

As described in Section 3.1.3 the density field is computed via summation of the respective smoothing kernel contributions of neighboring fluid particles j , refer to Eq. (15). Hence, considering the additional contributions of virtual boundary particles k_i^e , the density summation for a fluid particle i reads

$$\rho_i = m_i \sum_j W_{ij} + m_i \sum_e \sum_{k_i^e} W_{ik_i^e} \quad (31)$$

ensuring full support of the smoothing kernel.

Inspired by the treatment of boundary particles for rigid walls [13] the properties of virtual boundary particles k_i^e , i.e., density, pressure, and velocity, are extrapolated based on the corresponding quantities from neighboring fluid particles j of closest projection point c_i^e on interface element e . The goal is to achieve an undisturbed pressure field of fluid particles close to the interface. Satisfying the kinematic coupling condition on the fluid–structure interface Γ^{fs} , cf. Eq. (8), also called no-slip boundary condition, viscous forces are considered in the momentum equation. It shall be noted, that some boundary particle formulations in SPH are based on the assumption of zero normal pressure gradients close to the interface. However, in [13] it is shown, that including the pressure gradient obtained from a local force balance is beneficial to accurately model the pressure field of fluid particles close to the boundary. Therefore, a similar strategy is pursued in the following.

In a first step, the pressure $p_{k_i^e}$ of virtual boundary particles k_i^e is approximated based on a first order Taylor series expansion with center of expansion at

$$\langle \mathbf{r} \rangle_f = \frac{\sum_j \mathbf{r}_j W_{c_i^e j}}{\sum_j W_{c_i^e j}}. \quad (32)$$

The position $\langle \mathbf{r} \rangle_f$ can be interpreted as smoothed or averaged centroid position of the domain covered by the neighboring fluid particles j as illustrated in Fig. 6. Hence, the pressure of virtual boundary particles k_i^e is determined following

$$p_{k_i^e} = \langle p \rangle_f + (\mathbf{r}_{k_i^e} - \langle \mathbf{r} \rangle_f) \cdot \langle \nabla p \rangle_f \quad (33)$$

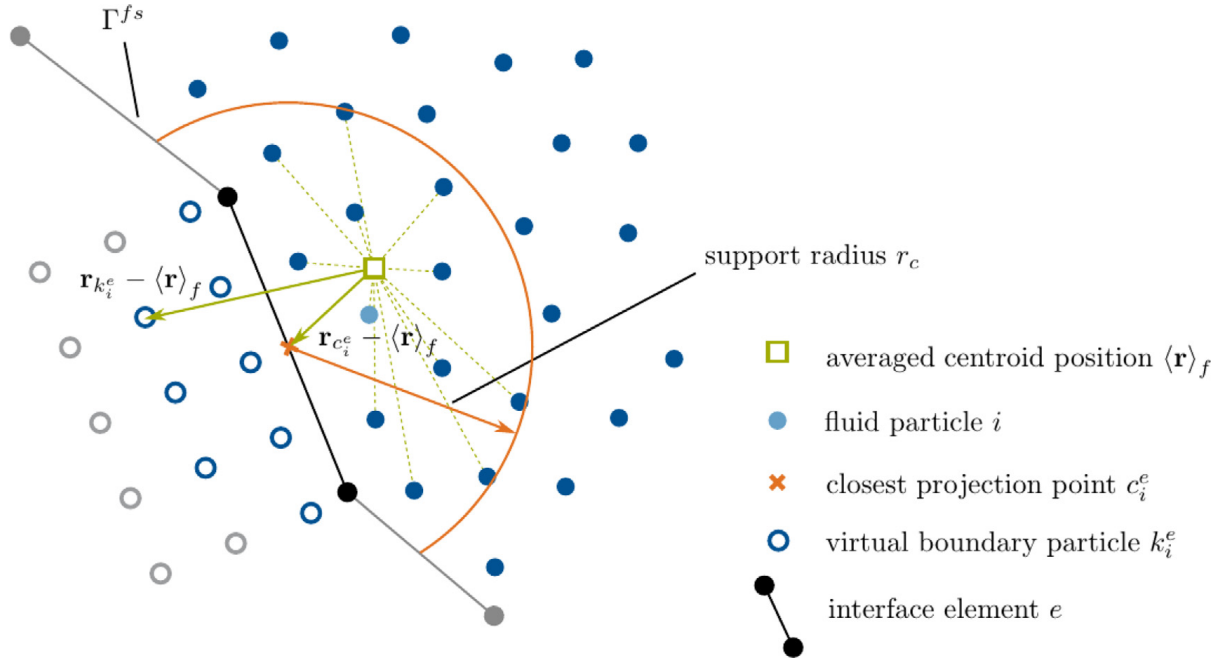


Fig. 6. Averaged centroid position f of the domain covered by neighboring fluid particles j of closest projection point c_i^e .

with smoothed pressure $\langle p \rangle_f = \sum_j p_j W_{c_i^e j} / \sum_j W_{c_i^e j}$ and smoothed pressure gradient

$$\langle \nabla p \rangle_f = \frac{\sum_j \rho_j W_{c_i^e j}}{\sum_j W_{c_i^e j}} (\mathbf{b}_i - \mathbf{a}_{c_i^e}). \tag{34}$$

The latter is approximated based on a local force balance neglecting viscous forces as proposed in [13], cf. Eq. (2), with acceleration $\mathbf{a}_{c_i^e}$ of the closest projection point c_i^e , cf. Remark 11. Applying the equation of state (20) of the respective interacting fluid particle i together with pressure $p_{k_i^e}$, the density $\rho_{k_i^e}$ of virtual boundary particles k_i^e follows as

$$\rho_{k_i^e} = \frac{p_{k_i^e}}{c^2} + \rho_0. \tag{35}$$

Remark 10. Note that the approximation of the smoothed pressure gradient $\langle \nabla p \rangle_f$, cf. Eq. (34), could be improved considering viscous forces in the local force balance, e.g., [36], however, at the cost of additional computational and algorithmic effort.

Remark 11. Similar to the position $\mathbf{r}_{c_i^e}$ of the closest projection point c_i^e , cf. Eq. (29), the velocity and acceleration are obtained following $\mathbf{u}_{c_i^e} = \sum_j N_j^e(\xi_{c_i^e}) \mathbf{u}_j^{fs}$ and $\mathbf{a}_{c_i^e} = \sum_j N_j^e(\xi_{c_i^e}) \mathbf{a}_j^{fs}$, where \mathbf{u}_j^{fs} and \mathbf{a}_j^{fs} are the velocities and accelerations of nodes j of interface element e .

In a next step, the velocity $\mathbf{u}_{k_i^e}$ of virtual boundary particles k_i^e is approximated considering the kinematic coupling condition on the fluid–structure interface Γ^{fs} , cf. Eq. (8), prescribing the velocity $\mathbf{u}_{c_i^e}$ of closest projection point c_i^e , cf. Remark 11. Applying a first order Taylor series expansion with center of expansion at $\langle \mathbf{r} \rangle_f$ according to (32) gives the relation

$$\mathbf{u}_{c_i^e} = \langle \mathbf{u} \rangle_f + (\mathbf{r}_{c_i^e} - \langle \mathbf{r} \rangle_f) \cdot \mathbf{e}_r \langle \nabla_{\mathbf{e}_r} \mathbf{u} \rangle_f \tag{36}$$

with smoothed velocity $\langle \mathbf{u} \rangle_f = \sum_j \mathbf{u}_j W_{c_i^e j} / \sum_j W_{c_i^e j}$ and unit vector \mathbf{e}_r pointing from particle i to closest projection point c_i^e thus representing the wall normal vector as defined in Section 3.3.3. The quantity $\langle \nabla_{\mathbf{e}_r} \mathbf{u} \rangle_f$ denotes the

smoothed directional derivative of the velocity in direction of \mathbf{e}_r and follows from Eq. (36) as

$$\langle \nabla_{\mathbf{e}_r} \mathbf{u} \rangle_f = \frac{\mathbf{u}_{c_i^e} - \langle \mathbf{u} \rangle_f}{(\mathbf{r}_{c_i^e} - \langle \mathbf{r} \rangle_f) \cdot \mathbf{e}_r} \quad (37)$$

exploiting the velocity $\mathbf{u}_{c_i^e}$ of the closest projection point c_i^e . Finally, the velocity $\mathbf{u}_{k_i^e}$ of virtual boundary particles k_i^e is approximated again applying a Taylor series expansion with center of expansion at $\langle \mathbf{r} \rangle_f$ resulting in

$$\mathbf{u}_{k_i^e} = \langle \mathbf{u} \rangle_f + (\mathbf{r}_{k_i^e} - \langle \mathbf{r} \rangle_f) \cdot \mathbf{e}_r \langle \nabla_{\mathbf{e}_r} \mathbf{u} \rangle_f. \quad (38)$$

In addition to the acceleration contributions \mathbf{a}_{ij} of neighboring fluid particles j , the momentum equation (16) for a fluid particle i is extended by the acceleration contributions $\mathbf{a}_{ik_i^e}$ of virtual boundary particles k_i^e related to the closest projection points c_i^e on interface elements e

$$\mathbf{a}_i = \sum_j \mathbf{a}_{ij} + \sum_e \sum_{k_i^e} \mathbf{a}_{ik_i^e} + \mathbf{b}_i \quad (39)$$

with

$$\mathbf{a}_{ik_i^e} = \frac{1}{m_i} (V_i^2 + V_{k_i^e}^2) \left[-\tilde{p}_{ik_i^e} \frac{\partial W}{\partial r_{ik_i^e}} \mathbf{e}_{ik_i^e} + \eta_i \frac{\mathbf{u}_{ik_i^e}}{r_{ik_i^e}} \frac{\partial W}{\partial r_{ik_i^e}} \right] \quad (40)$$

and density-weighted inter-particle averaged pressure $\tilde{p}_{ik_i^e}$ as defined in (17).

Remark 12. The extrapolation of pressure and velocity for virtual boundary particles k_i^e by the Taylor series expansions (33) and (38) requires the quantities $\langle \cdot \rangle_f$ to be evaluated only once for each closest projection point c_i^e , which is the main advantage of this procedure regarding computational costs.

Remark 13. Note that the contributions of virtual boundary particles k_i^e resulting from a background pressure p_b as part of the transport velocity formulation [27] are also considered for fluid particles i , however, similar to Section 3.1.4 for ease of notation not pointed out here.

3.3.5. Nodal interface forces on interface elements

The coupling of the fluid and the structural field, cf. Fig. 2, following a Dirichlet–Neumann partitioned approach (as discussed in more detail in Section 3.4) requires the evaluation of interface forces \mathbf{f}^{fs} . To enforce conservation of linear momentum at the fluid–structure interface Γ^{fs} , in accordance with (19), the interface forces \mathbf{f}^{fs} can be computed directly from the resulting acceleration contributions of fluid particles interacting with virtual boundary particles, as described in the previous section. Consequently, the resulting force $\mathbf{f}_{c_i^e}^e$ acting on an interface element e at the closest projection point c_i^e due to interaction of virtual boundary particles k_i^e with fluid particle i reads

$$\mathbf{f}_{c_i^e}^e = -m_i \sum_{k_i^e} \mathbf{a}_{ik_i^e} \quad (41)$$

with mass m_i of fluid particle i and acceleration contribution $\mathbf{a}_{ik_i^e}$ of virtual boundary particle k_i^e on fluid particle i . Note that the above given formulation of the resulting force $\mathbf{f}_{c_i^e}^e$ guarantees conservation of linear momentum between fluid particle i and interface element e . The resulting force $\mathbf{f}_{c_i^e}^e$ (being a point force acting on interface element e at closest projection point c_i^e) is distributed to the nodes j of interface element e using its shape functions $N_j^e(\boldsymbol{\xi}_{c_i^e})$ evaluated at the closest projection point c_i^e given in iso-parametric coordinates $\boldsymbol{\xi}_{c_i^e}$. Finally, the interface force \mathbf{f}_j^{fs} of a node j results from summation over all force contributions $\mathbf{f}_{c_i^e}^e$ of fluid particles i acting on various interface elements e connected to node j

$$\mathbf{f}_j^{fs} = \sum_e \sum_i N_j^e(\boldsymbol{\xi}_{c_i^e}) \mathbf{f}_{c_i^e}^e. \quad (42)$$

3.4. Partitioned coupling approach

The fluid and the structural field are coupled following a Dirichlet–Neumann partitioned approach, where the fluid field is the Dirichlet partition with prescribed interface displacements \mathbf{d}^{fs} and the structural field is the Neumann partition subject to interface forces \mathbf{f}^{fs} , as illustrated in Fig. 2 (right).

Introducing the field operators \mathcal{F} and \mathcal{S} for the fluid and the structural problem [5] both mapping the interface displacements \mathbf{d}^{fs} to interface forces

$$\mathbf{f}_{\mathcal{F}}^{fs} = \mathcal{F}(\mathbf{d}^{fs}) \quad \text{and} \quad \mathbf{f}_{\mathcal{S}}^{fs} = \mathcal{S}(\mathbf{d}^{fs}), \quad (43)$$

equilibrium at the interface Γ^{fs} is satisfied in case the condition

$$\mathcal{F}(\mathbf{d}^{fs}) = \mathcal{S}(\mathbf{d}^{fs}) \quad (44)$$

holds. The inverse fluid and structural field operators mapping interface forces \mathbf{f}^{fs} to interface displacements are consequently defined as

$$\mathbf{d}_{\mathcal{F}}^{fs} = \mathcal{F}^{-1}(\mathbf{f}^{fs}) \quad \text{and} \quad \mathbf{d}_{\mathcal{S}}^{fs} = \mathcal{S}^{-1}(\mathbf{f}^{fs}). \quad (45)$$

In [7] it is shown that weakly coupled schemes exhibit instabilities in FSI problems with incompressible flows due to the artificial added mass effect. To overcome those instabilities, a fixed-point coupling algorithm is employed to iteratively reach dynamic equilibrium of the fluid and the structural field at the interface with respect to a predefined convergence criterion, i.e., fluid and structural field are strongly coupled. Following a synchronous time stepping scheme the same time step size Δt is set for both fluid and structural solver and is based on the in general more severe restrictions of the SPH time integration scheme, cf. Eq. (25).

Remark 14. Note that the applied generalized alpha time integration scheme for the structural field being an implicit method in general allows for a larger time step size Δt than possible for the fluid field solved using SPH. Thus, future research may focus on asynchronous time stepping and sub-stepping schemes in order to reduce computational costs.

The coupling algorithm applied herein is described in detail below as Algorithm 1. Convergence of the iterative coupling loop in Algorithm 1 is achieved in case the following criterion based on the increment of interface displacements $\Delta \mathbf{d}_{n+1,i+1}^{fs}$ is fulfilled

$$\frac{|\Delta \mathbf{d}_{n+1,i+1}^{fs}|}{\Delta t \sqrt{n_{dof}^{fs}}} < \epsilon \quad (46)$$

with time step size Δt , number of interface degrees of freedom n_{dof}^{fs} , and predefined tolerance for convergence ϵ .

Remark 15. In general, applying dynamic relaxation of the interface displacements \mathbf{d}^{fs} in each iteration of the coupling algorithm [5] can have a stabilizing effect and accelerate the convergence of the partitioned coupling. However, it shall be noted, that due to the restrictions of the time step size Δt resulting from the SPH time integration scheme, an accelerating effect is not required with the proposed formulation, cf. examples 4.2.2 and 4.2.3.

4. Numerical examples

The purpose of this section is to validate the novel sliding boundary particle approach and the proposed numerical formulation for solving fluid–structure interaction problems examining several numerical examples in two and three dimensions. The obtained results are assessed on the basis of analytical solutions and reference solutions given in the literature.

4.1. Validation of the sliding boundary particle approach

At first, the capabilities of the proposed method considering fluid flow in the presence of rigid and undeformable structures with a focus on the validation of the novel sliding boundary particle approach as presented in Section 3.3

Algorithm 1 Time loop of a Dirichlet–Neumann partitioned fixed-point fluid–structure interaction algorithm

```

while  $t < T$  do
   $t \leftarrow t + \Delta T$  ▷ increment time
   $i \leftarrow 1$  ▷ reset iteration counter
   $\mathbf{d}_{n+1,i}^{fs}$  ▷ predict interface displacements
  while true do
     $\mathbf{f}_{n+1,i+1}^{fs} = \mathcal{F}(\mathbf{d}_{n+1,i}^{fs})$  ▷ solve fluid field
     $\mathbf{d}_{n+1,i+1}^{fs} = \mathcal{S}^{-1}(\mathbf{f}_{n+1,i+1}^{fs})$  ▷ solve structural field
     $\Delta \mathbf{d}_{n+1,i+1}^{fs} = \mathbf{d}_{n+1,i+1}^{fs} - \mathbf{d}_{n+1,i}^{fs}$  ▷ compute increment of interface displacements
    if  $|\Delta \mathbf{d}_{n+1,i+1}^{fs}| / \Delta t \sqrt{n_{dof}^{fs}} < \epsilon$  then ▷ check convergence criterion, cf. equation (46)
      break
    end if
     $i \leftarrow i + 1$  ▷ increment iteration counter
  end while
   $n \leftarrow n + 1$  ▷ increment step counter
end while

```

are shown. The obtained results are compared to analytical solutions and reference solutions given in the literature both in a quantitative and qualitative manner. Additionally, as rigid and undeformable structures are considered, these examples can also be examined utilizing an implementation of the rigid wall boundary condition proposed in [13]. As a result, this allows for validation of the proposed sliding boundary particle approach against the established rigid wall boundary condition [13] within the context of rigid and undeformable structures. Finally, an example demonstrates the advantages of the proposed sliding boundary particle approach in the regime of large structural deformations. In all examples discussed in this section, the structural field is not solved, though, the fluid–structure interface is explicitly described either via an interface mesh or analytically by parameterization.

4.1.1. Hydrostatic pressure in a fluid between two parallel plates

The gap between two spatially fixed and undeforming parallel plates being a distance of $L = 0.2$ apart is filled with a Newtonian fluid of density $\rho^f = 1.0$ and kinematic viscosity $\nu^f = 1.0 \times 10^{-2}$. A coordinate axis \mathbf{e}_q is introduced pointing in the direction perpendicular to the parallel plates with origin centered between the latter, cf. Fig. 7(a). Finally, a body force of magnitude $b_q = 0.1$ acting in direction \mathbf{e}_q is applied on the fluid. For this simple example the analytical solution for the pressure profile in the static equilibrium state is given to $p(q) = \rho^f b_q q$ showing linear behavior.

The fluid domain between the two parallel plates is discretized by 40 layers of fluid particles, i.e., with an initial particle spacing $\Delta x = 5.0 \times 10^{-3}$. The smoothing length h of the smoothing kernel is set equal to the initial particle spacing Δx resulting in a support radius $r_c = 1.5 \times 10^{-2}$. For the fluid phase, an artificial speed of sound $c = 1.0$ is chosen, leading to a reference pressure $p_0 = 1.0$. The background pressure p_b is set equal to the reference pressure p_0 . The two parallel plates are modeled by a surface element each. The problem is solved with time step size $\Delta t = 3.125 \times 10^{-4}$, cf. Eq. (25), until a static equilibrium state is reached.

Fig. 7(b) shows the hydrostatic pressure in the fluid at time $t = 10.0$. The results compared to the analytical solution are post-processed applying SPH approximation (14). The results are in very good agreement with the analytical solution showing the capability of the proposed sliding boundary particle approach to capture linear pressure profiles near the boundary, cf. Eq. (33). In addition, the example is computed with an implementation of the rigid wall boundary condition [13] modeling the two parallel plates via fixed boundary particles. Comparing the result to those obtained with the proposed sliding boundary particle approach, cf. Fig. 7(b), delivers apart from roundoff errors equivalent results for this example. Finally, a detailed view of the boundary region at $q = 0.1$ is given

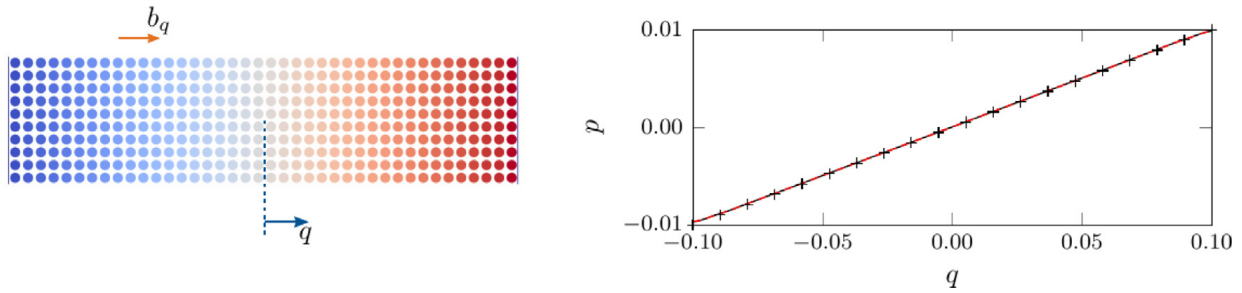


Fig. 7. Hydrostatic pressure in a fluid between two parallel plates: particle distribution colored with fluid pressure ranging from -0.01 (blue) to 0.01 (red) with illustration of coordinate axis and body force (left) and numerical result using the proposed sliding boundary particle approach (black solid line) and the rigid wall boundary condition [13] (red dashed line) compared to analytical solution (crosses) (right) in static equilibrium state at time $t = 10.0$. (For interpretation of the references to color in this figure legend, the reader is referred to the web version of this article.)

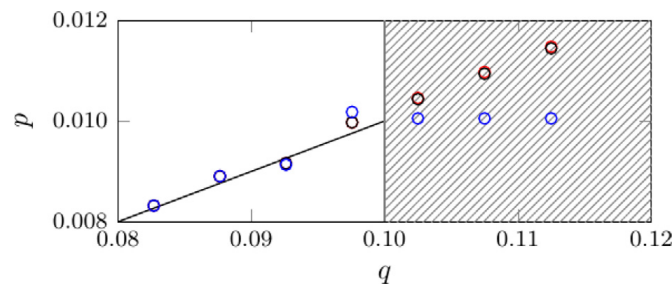


Fig. 8. Hydrostatic pressure in a fluid between two parallel plates: detailed view of boundary region with pressure values of fluid particles and (virtual) boundary particles using the proposed sliding boundary particle approach *with* (black circles) and *without* (blue circles) considering the pressure gradient (34) in Eq. (33), and the rigid wall boundary condition [13] also considering the pressure gradient (red circles) compared to analytical solution (black solid line). (For interpretation of the references to color in this figure legend, the reader is referred to the web version of this article.)

in Fig. 8 showing the pressure values of fluid particles and (virtual) boundary particles obtained with the proposed sliding boundary particle approach and the rigid wall boundary condition [13]. In addition, a modified variant of the sliding boundary particle approach *without* considering the pressure gradient (34) in Eq. (33) is examined. With this modified variant, the pressure value of the fluid particle closest to the boundary, cf. Fig. 8, clearly deviates from the expected linear pressure profile. Thus, considering the improved accuracy and the fact that the computational costs required for the extrapolation of pressure (and velocity) for virtual boundary particles are negligible, cf. Remark 12, in the following, the standard variant as proposed in Section 3.3.4 is applied.

4.1.2. Planar Taylor–Couette flow

In this example, a laminar, planar Taylor–Couette flow is considered. The gap between two coaxial cylinders with radii $r_1 = 1.0$ and $r_2 = 2.0$ is filled with a Newtonian fluid of density $\rho^f = 1.0$ and kinematic viscosity $\nu^f = 1.0$. The inner cylinder is fixed, i.e., its angular velocity is $\omega_1 = 0.0$, while the outer cylinder rotates with angular velocity $\omega_2 = 2.0$ around its axis of symmetry. No-slip boundary conditions are applied between the fluid and the surfaces of the cylinders. The geometry and boundary conditions of the problem are illustrated in Fig. 9(a). The Reynolds number of the problem is $Re = \omega_2 r_2 (r_2 - r_1) / \nu^f = 4.0$ with maximum velocity $\omega_2 r_2$ and gap $(r_2 - r_1)$ between the coaxial cylinders.

The fluid domain is discretized by fluid particles with initial particle spacing $\Delta x = 5.0 \times 10^{-2}$. The smoothing length h is equal to the initial particle spacing Δx resulting in a support radius $r_c = 1.5 \times 10^{-1}$. The artificial speed of sound is set to $c = 40.0$, hence the reference pressure is $p_0 = 1600.0$. The background pressure p_b is set equal to the reference pressure p_0 . In this example, the structural surfaces are described analytically by parameterization of the cylindrical surfaces in order to show the capabilities and flexibility of the proposed sliding boundary particle approach. However, it shall be noted that the geometry naturally could have been discretized by a finite element

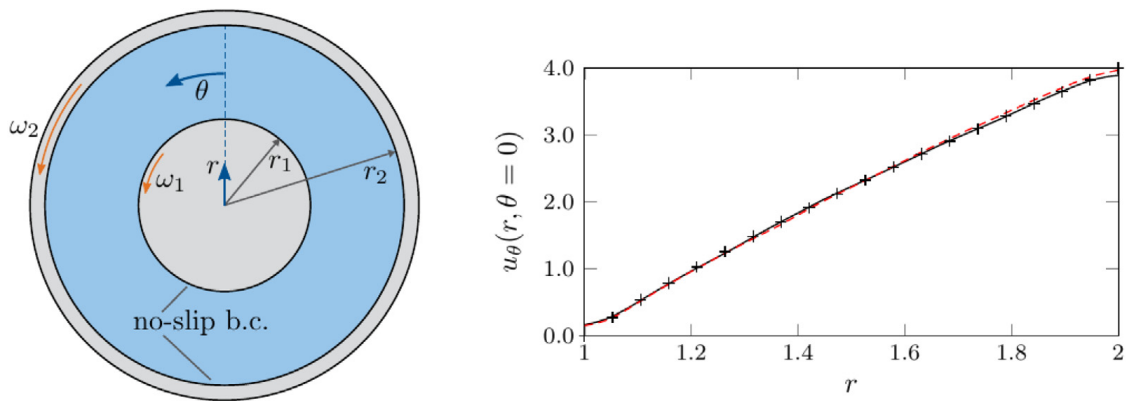


Fig. 9. Planar Taylor–Couette flow: geometry and boundary conditions of the problem (left) and stationary velocity of the fluid in angular direction using the proposed sliding boundary particle approach (black solid line) and the rigid wall boundary condition [13] (red dashed line) compared to analytical solution [37] (crosses) (right). (For interpretation of the references to color in this figure legend, the reader is referred to the web version of this article.)

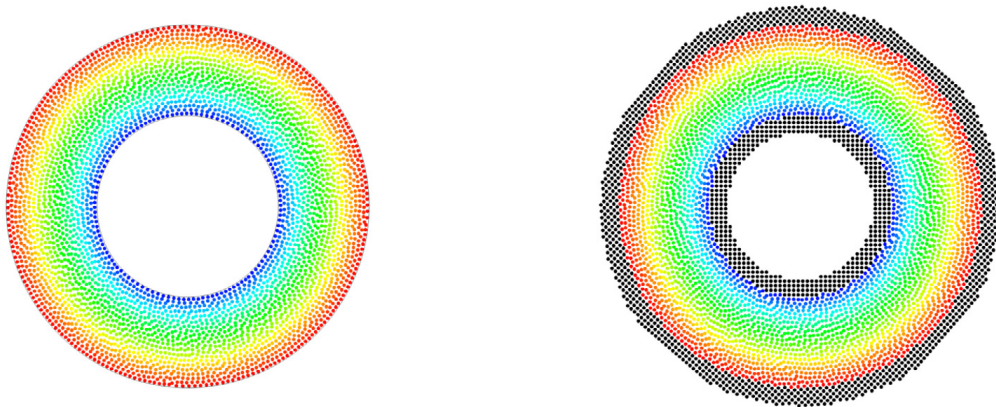


Fig. 10. Planar Taylor–Couette flow: particle distribution at time $t = 2.0$ colored with magnitude of the fluid velocity ranging from 0.0 (blue) to 4.0 (red) using the sliding boundary particle approach with parameterization of the cylindrical shape (left) and the rigid wall boundary condition [13] with fixed boundary particles approximating the cylindrical shape (right). (For interpretation of the references to color in this figure legend, the reader is referred to the web version of this article.)

mesh. The problem is solved with time step size $\Delta t = 3.125 \times 10^{-4}$, cf. Eq. (25), until a nearly stationary state is reached at time $t = 2.0$.

In Fig. 9(b) the stationary velocity of the fluid in the gap between the cylinders, post-processed applying SPH approximation (14), is plotted over the radius r in angular direction θ at time $t = 2.0$. The result obtained with the proposed sliding boundary particle approach is compared to the result obtained with an implementation of the rigid wall boundary condition [13] and to the analytical solution of the problem [37]. Both methods show a high degree of conformity with the analytical solution. The deviation of the velocity in Fig. 9(b) close to the cylindrical surfaces, i.e., at $r = r_1$ and $r = r_2$, results from missing kernel support during post-processing. This phenomenon likewise occurs for both methods, but at a varying degree. Finally, the particle distribution at time $t = 2.0$ is shown in Fig. 10 comparing the results of the sliding boundary particle approach with the rigid wall boundary condition [13]. In contrast to the rigid wall boundary condition with fixed boundary particles approximating the cylindrical shape, the sliding boundary particle approach does not suffer from geometry discretization errors thus resulting in an improved preservation of the solution symmetry (cf. Fig. 10) and a decreased deviation from the analytical velocity profile (cf. Fig. 9(b)). On the other hand, approaches where the cylindrical shape is discretized by boundary particles in ring-shaped arrangement suffer from a disturbed support of the smoothing kernel of fluid particles close to the cylindrical surface, similar than in Fig. 3.

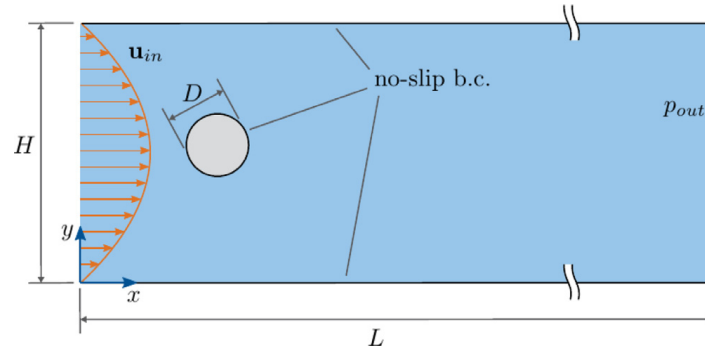


Fig. 11. Laminar flow around a rigid cylinder: geometry and boundary conditions of the benchmark problem as proposed by Schäfer and Turek et al. [38].

4.1.3. Laminar flow around a rigid cylinder

A prominent CFD benchmark problem was proposed by Schäfer and Turek et al. [38] in the year 1996 and since then was considered in a huge variety of publications. The benchmark is concerned with the laminar flow around a rigid cylinder in a channel. Within this publication, the problem is utilized to validate the momentum exchange at the fluid–structure interface, i.e., at the surface of the cylinder, examining characteristic quantities such as the drag and the lift coefficient or the cycle duration of the time-periodic solution. In the following the focus is set on the two-dimensional, unsteady test case 2D-2 [38].

Consider a rigid cylinder of diameter $D = 0.1$ with center fixed at position $(0.2, 0.2)$ in a rectangular channel of length $L = 2.2$ and height $H = 0.41$, as illustrated in Fig. 11. The channel is filled by a Newtonian fluid initially at rest with density $\rho^f = 1.0$ and kinematic viscosity $\nu^f = 1.0 \times 10^{-3}$. It shall be noted that the problem setup is designed intentionally non-symmetric in order to initiate unsteady vortex shedding behind the cylinder. No-slip boundary conditions are applied at the bottom and top channel wall and on the surface of the cylinder. At the channel inflow, a parabolic, time dependent velocity profile $\mathbf{u}_{in} = \mathbf{u}(x = 0, y, t)$ is prescribed with components

$$u_x(x = 0, y, t) = u_{max} \frac{4y(H - y)}{H^2} \tau(t) \quad \text{and} \quad u_y(x = 0, y, t) = 0.0 \quad (47)$$

where

$$\tau(t) = \begin{cases} \frac{1}{2}(1 - \cos(\frac{\pi}{2}t)) & \text{if } t < 2.0 \\ 1.0 & \text{otherwise} \end{cases} \quad (48)$$

The maximum inflow velocity is set to $u_{max} = 1.5$ resulting in a Reynolds number $Re = u_{mean}D/\nu^f = 100$ with mean velocity $u_{mean} = 2/3u_{max} = 1.0$ for all times $t \geq 2.0$. At the channel outflow a zero pressure condition $p_{out} = p(x = L, y, t) = 0.0$ is applied.

The fluid domain is discretized by fluid particles with initial particle spacing $\Delta x = 2.0 \times 10^{-3}$. The smoothing length h is set equal to the initial particle spacing Δx resulting in a support radius $r_c = 6.0 \times 10^{-3}$ of the smoothing kernel. An artificial speed of sound $c = 12.5$ is chosen for the fluid phase leading to a reference pressure $p_0 = 156.25$. The background pressure is set to $p_b = 312.5$ and is on the order of the reference pressure as proposed by [27]. The bottom and top channel walls are modeled utilizing boundary particles according to [13] with spacing equal to the initial particle spacing Δx . On account of the fact that the cylinder is fixed and undeformable only the surface of the cylinder is regularly discretized by 48 surface elements of same size that are considered in the computation of the fluid field, i.e., the structural field is not solved. The unsteady flow simulation is solved for times $t \in [0, 8.0]$ with a time step size of $\Delta t = 4.0 \times 10^{-5}$ based on the time step size conditions defined in Eq. (25).

To allow for a quantitative comparison of the obtained results with existing reference solutions, the drag and the lift coefficient are defined as

$$c_{drag} = \frac{2f_{drag}}{\rho^f u_{mean}^2 D} \quad \text{and} \quad c_{lift} = \frac{2f_{lift}}{\rho^f u_{mean}^2 D} \quad (49)$$

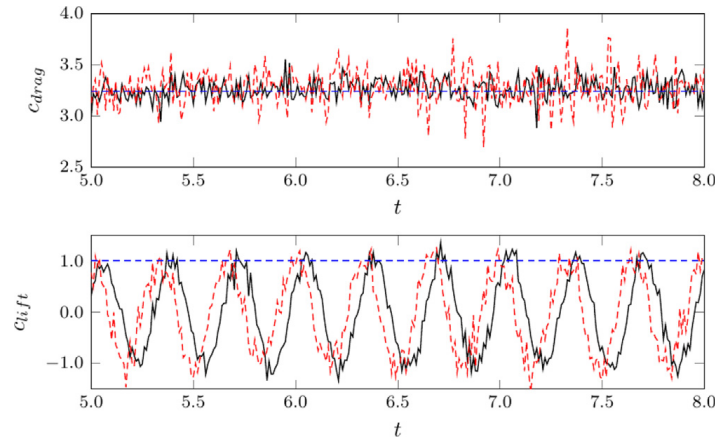


Fig. 12. Laminar flow around a rigid cylinder: drag coefficient c_{drag} and lift coefficient c_{lift} using the proposed sliding boundary particle approach (black solid line) and the rigid wall boundary condition [13] (red dashed line) compared to the upper bounds given in reference solution [38] (blue dashed line). (For interpretation of the references to color in this figure legend, the reader is referred to the web version of this article.)

where f_{drag} and f_{lift} denote the forces in x - respectively y -direction acting on the cylinder obtained from the sum of all force contributions of fluid particles acting on interface elements of the discretized surface of the cylinder, cf. Eq. (41). Fig. 12 shows the drag coefficient c_{drag} and the lift coefficient c_{lift} obtained for the fully developed time-periodic solution after approximately $t = 5.0$. Both drag and lift coefficient show typical fluctuations as common in SPH-based simulations (similar to an example in [27]), that result from disturbances of the density field [12] due to relative particle movement. Besides that, the obtained results are in good agreement to the lower bound ($c_{drag} = 3.2200$, $c_{lift} = 0.9900$) and upper bound ($c_{drag} = 3.2400$, $c_{lift} = 1.0100$) of the maximum drag and lift coefficient given by [38]. The shape of the curve of lift coefficient c_{lift} allows identifying periodic cycles of the solution with approximate cycle duration $t_{cycle} = 0.33$ in close agreement to the result of [39]. In addition, the example is computed discretizing the cylinder with fixed boundary particles based on an implementation of the rigid wall boundary condition [13]. The results in form of the drag coefficient c_{drag} and the lift coefficient c_{lift} are compared to those obtained with the proposed sliding boundary particle approach, cf. Fig. 12, and likewise show the observed typical fluctuations. Note that the visible phase shift in the time-periodic solution of the lift coefficient c_{lift} is stemming from roundoff errors that influence the initiation of vortex shedding. Finally, Fig. 13 shows the magnitude of the fluid velocity field for a periodic cycle from $t_0 = 6.90$ to $t_1 = 7.23$ at four equidistant points in time. At time $t = 6.98$ the present results of the velocity field visualized in Fig. 13 are qualitatively in good agreement to the results of [39]. Altogether, the results of the CFD benchmark problem obtained with the sliding boundary particle approach represent the given reference solutions [38,39] both quantitatively and qualitatively in good approximation and further showcase the capabilities of the novel formulation to accurately model the momentum exchange at the fluid–structure interface.

4.1.4. Isochoric deformation of a box filled with a fluid

This example aims to demonstrate the advantages of the proposed sliding boundary particle approach over fixed (material) boundary particle methods in the case of large deformations at the fluid–structure interface. To this end, an academic example is examined utilizing both the proposed sliding boundary particle approach and an implementation of the rigid wall boundary condition [13] with boundary particles fixed to material points of the structure.

An initially quadratic structural box with inner edge length $b = 0.1$ and wall thickness $d = 0.015$ is filled by a Newtonian fluid initially at rest with density $\rho^f = 1.0$ and kinematic viscosity $\nu^f = 1.0 \times 10^{-2}$. An isochoric deformation of the structural box to obtain a rectangular shape (with final edge lengths $b_x = 0.2$ and $b_y = 0.05$ starting from $t = 2.5$) is prescribed, defined by the deformation gradient

$$\mathbf{F} = \begin{bmatrix} \lambda(t) & 0 \\ 0 & 1.0/\lambda(t) \end{bmatrix} \quad \text{where} \quad \lambda(t) = \begin{cases} 1.0 + 0.4t & \text{if } t < 2.5 \\ 2.0 & \text{otherwise} \end{cases}, \quad (50)$$

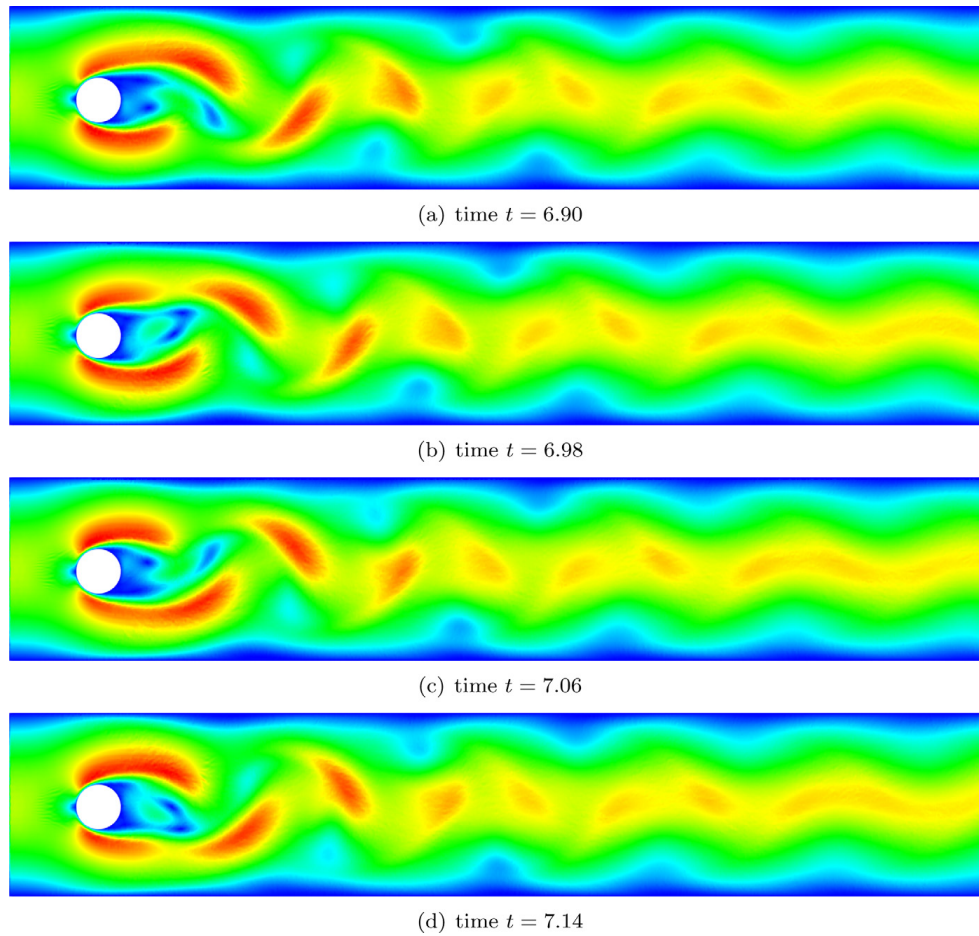


Fig. 13. Laminar flow around a rigid cylinder: magnitude of the fluid velocity field ranging from 0.0 (blue) to 2.2 (red) for a periodic cycle from $t_0 = 6.90$ to $t_1 = 7.23$ at four equidistant points in time. (For interpretation of the references to color in this figure legend, the reader is referred to the web version of this article.)

and accordingly with $\det \mathbf{F} = 1.0$. It follows, that also the volume of the fluid within the structural box remains constant at all times. Consequently, in the final static equilibrium state the fluid density is expected to be constant throughout the entire fluid domain.

The fluid domain within the structural box is discretized by fluid particles with initial particle spacing $\Delta x = 5.0 \times 10^{-3}$. The smoothing length h of the smoothing kernel is set equal to the initial particle spacing Δx resulting in a support radius $r_c = 1.5 \times 10^{-2}$. For the fluid phase, an artificial speed of sound $c = 1.0$ is chosen, leading to a reference pressure $p_0 = 1.0$. The background pressure p_b is set equal to the reference pressure p_0 . The walls of the structural box are either modeled by surface elements when using the proposed sliding boundary particle approach or by boundary particles fixed to material points of the structure when using the rigid wall boundary condition [13]. The problem is solved for times $t \in [0, 10.0]$ with time step size $\Delta t = 3.125 \times 10^{-4}$, cf. Eq. (25).

Fig. 14 shows the particle distribution obtained using the rigid wall boundary condition [13] with fixed (material) boundary particles in the initial configuration and at time $t = 10.0$. Prescribing the deformation of the structural box naturally also distorts the initially regular arrangement of boundary particles fixed to material points of the structure, i.e., the boundary particle spacing is stretched in horizontal direction and compressed in vertical direction, which is clearly visible at time $t = 10.0$. As a consequence, the support of the smoothing kernel of a fluid particle close to the interface is disturbed, also influencing the density (and pressure) field in the deformed fluid domain. Eventually, leakage of fluid particles through the fluid–structure interface occurs when the boundary particle spacing becomes too large, and accordingly, the fluid density within the structural box is significantly reduced with an average density error of approximately 7.5%. The results obtained with the proposed sliding boundary particle approach are shown in Fig. 15. For the purposes of illustration, at time $t = 10.0$ the virtual boundary particles belonging to a fluid

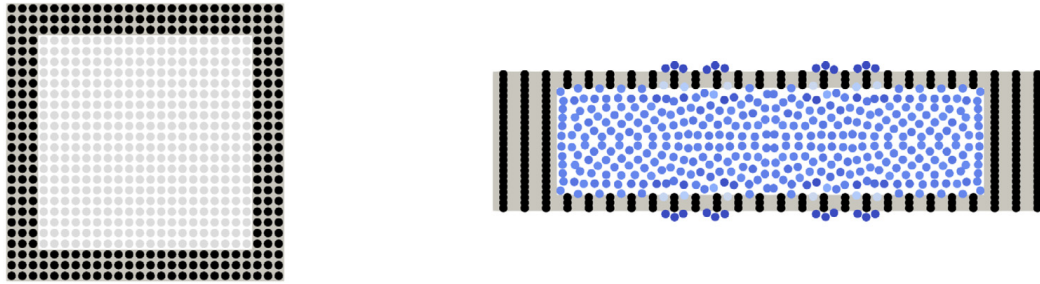


Fig. 14. Isochoric deformation of a box filled with a fluid: particle distribution obtained using the rigid wall boundary condition [13] with fixed (material) boundary particles in the initial configuration with fluid particles (gray) and boundary particles (black) (left) and in the final configuration with fluid particles colored with fluid density ranging from 0.9 (blue) to 1.1 (red) and boundary particles (black) (right). (For interpretation of the references to color in this figure legend, the reader is referred to the web version of this article.)

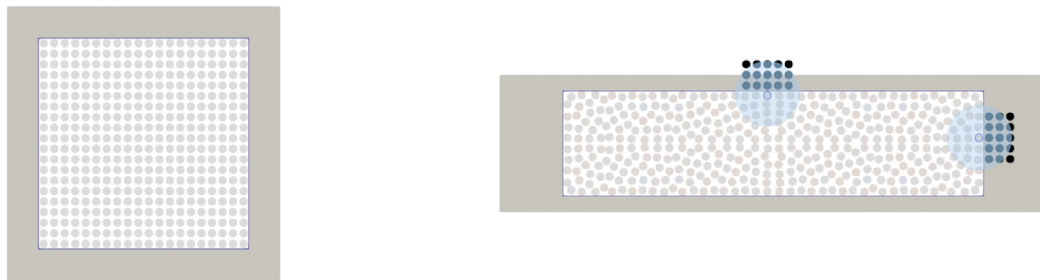


Fig. 15. Isochoric deformation of a box filled with a fluid: particle distribution obtained using the proposed sliding boundary particle approach in the initial configuration with fluid particles (gray) and surface elements (blue) (left) and in the final configuration with fluid particles colored with fluid density ranging from 0.9 (blue) to 1.1 (red) and an illustration of the virtual boundary particles (black) belonging to two characteristic fluid particles (right). (For interpretation of the references to color in this figure legend, the reader is referred to the web version of this article.)

particle close to the upper edge and to a fluid particle close to the right edge are shown. Here the full benefits of the proposed sliding boundary particle approach become obvious: full support of the smoothing kernel of a fluid particle close to the interface is retained by a transient set of regularly arranged virtual boundary particles. As a result, an undisturbed density (and pressure) field is achieved in the deformed fluid domain, and consequently, no leakage of fluid particles through the fluid–structure interface occurs. Altogether, this example illustrates the advantages of the proposed sliding boundary particle approach over fixed (material) boundary particle methods when considering large deformations of the fluid–structure interface.

4.2. Validation of the fluid–structure interaction framework

Additional complexity is added by considering freely moving and deformable structures stressing the coupling of fluid and structural field following a Dirichlet–Neumann partitioned approach. Consequently, in the following examples also the structural field is solved. Analytical solutions and reference solutions given in the literature are used to validate the obtained results in quantitative and qualitative manner.

4.2.1. A rigid cylinder floating in a shear flow

The following example is based on the studies [40,41] stating that a rigid cylinder floating in a shear flow in a channel always migrates to the center of the channel independent of its initial position and velocity. Here, this example serves as a further validation of the proposed method considering rigid body motion of the structural field. For validation, the obtained results are compared to [36] where both the fluid and the solid field are discretized using SPH.

A rigid cylinder of diameter $D = 0.0025$ allowed to move freely is initially placed at position $(0.002, 0.0075)$ in a rectangular channel of length $L = 0.1$ and height $H = 0.01$, as illustrated in Fig. 16. The remainder of the channel is occupied by a Newtonian fluid with density $\rho^f = 1.0$ and kinematic viscosity $\nu^f = 5.0 \times 10^{-6}$. The

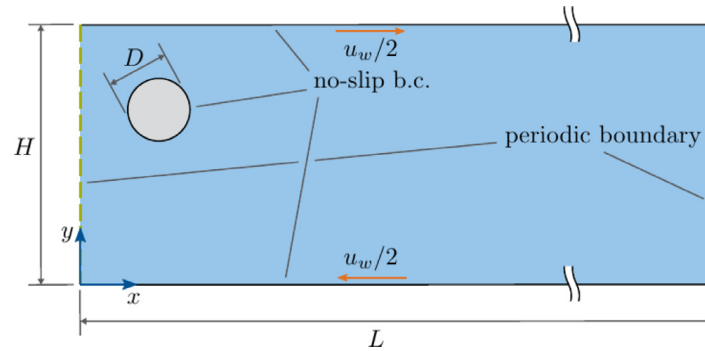


Fig. 16. A rigid cylinder floating in a shear flow: geometry and boundary conditions of the problem.

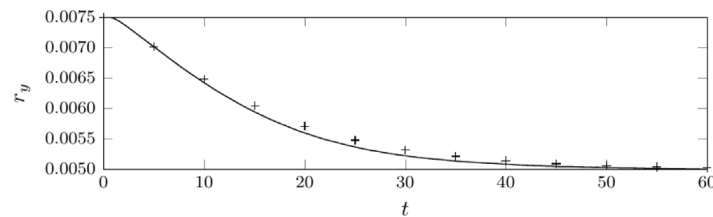


Fig. 17. A rigid cylinder floating in a shear flow: vertical position r_y of the center of the cylinder in the channel computed by the method developed in this article (solid line) compared to reference solution [36] (crosses).

bottom and top channel walls move with a velocity $u_w/2 = 0.01$ in opposite direction inducing a shear flow in the channel under consideration of no-slip boundary conditions on all fluid–structure interfaces. The Reynolds number of the problem is $Re = u_w D^2 / 4\nu^f H = 0.625$ [36,41] taking into account the diameter of the cylinder D and the channel height H . At the left and right end of the channel, periodic boundary conditions are applied.

In this example, the fluid domain is discretized by fluid particles with initial particle spacing $\Delta x = 1.0 \times 10^{-4}$. The smoothing length h is equal to the initial particle spacing Δx leading to a support radius $r_c = 3.0 \times 10^{-4}$ of the smoothing kernel. An artificial speed of sound $c = 0.25$ is chosen, resulting in a reference pressure $p_0 = 0.0625$ for the fluid phase. The background pressure p_b is set equal to the reference pressure p_0 . The motion of the bottom and top channel walls is modeled using moving boundary particles according to [13]. A Saint Venant–Kirchhoff model with relatively high Young’s modulus $E^s = 1.0 \times 10^6$ and Poisson’s ratio $\nu^s = 0.4$ is applied for the structure in order to penalize deformation of the cylinder and allow primarily rigid body motions. The cylinder is regularly discretized by 144 first-order elements with 48 surface elements on the surface of the cylinder. Convergence of the iterative coupling algorithm is checked based on the tolerance $\epsilon = 1.0 \times 10^{-8}$ in Eq. (46). The problem is solved for times $t \in [0, 60.0]$ with a time step size of $\Delta t = 1.0 \times 10^{-4}$.

The vertical position of the center of the cylinder in the channel over time t is displayed in Fig. 17. The cylinder migrates to the center line of the channel as expected. In addition, a quantitative comparison to the results given in [36] shows good agreement for the dynamics of the solution.

4.2.2. Flow-induced oscillations of a flexible beam attached to a rigid cylinder

Based on the benchmark problem of a laminar flow around a rigid cylinder in a channel [38], cf. Section 4.1.3, a FSI benchmark was proposed by Turek and Hron [42] as modification of an example first described in [43]. The purpose of the example is to study flow-induced oscillations of a flexible beam attached to a rigid cylinder in a channel flow. In the following the two-dimensional test case FSI2 [42] is considered that is characterized by large structural displacements.

The problem setup (rectangular channel of length $L = 2.2$ and height $H = 0.41$, rigid cylinder of diameter $D = 0.1$ with center fixed at position $(0.2, 0.2)$) is very equal to the example of a laminar flow around a rigid cylinder discussed in Section 4.1.3. In addition, in this example a flexible beam of length $l = 0.35$ and height $h = 0.02$ is attached at the downstream end of the rigid cylinder, i.e., at position $(0.25, 0.2)$ as illustrated in Fig. 18. Note that also the length of the channel remains equal to the example in Section 4.1.3 and is thus slightly shorter

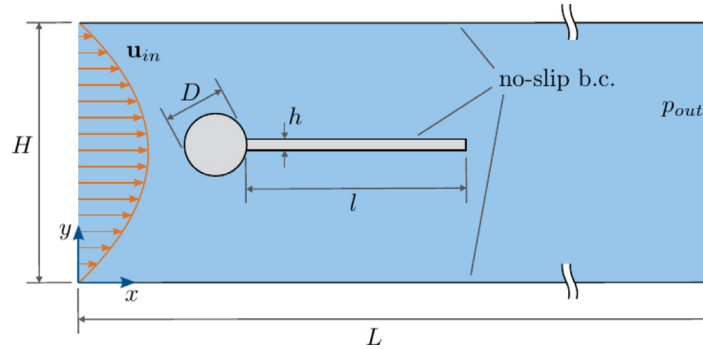


Fig. 18. Flow-induced oscillations of a flexible beam attached to a rigid cylinder: geometry and boundary conditions of the benchmark problem as proposed by Turek and Hron [42].

than originally proposed for the benchmark [42]. A control point needed for evaluation of the results, e.g., in Fig. 19, is placed at the tip of the flexible beam, i.e., at position (0.6, 0.2) in the undeformed configuration. The fluid properties (Newtonian fluid, density $\rho^f = 1.0$, kinematic viscosity $\nu^f = 1.0 \times 10^{-3}$) remain unchanged compared to the previous example. The density of the flexible structure is set to $\rho_0^s = 10.0$ resulting in a density ratio of $\rho_0^s/\rho^f = 10.0$. A Saint Venant–Kirchhoff model with Young’s modulus $E^s = 1.4 \times 10^3$ (resp. shear modulus $\mu^s = 0.5 \times 10^3$) and Poisson’s ratio $\nu^s = 0.4$ is utilized to describe the constitutive behavior of the flexible beam. The same boundary conditions as in the example in Section 4.1.3 (no-slip boundary conditions on all surfaces including the flexible beam, parabolic and time dependent velocity profile at channel inflow with mean velocity $u_{mean} = 1.0$ for all times $t \geq 2.0$, zero pressure conditions at channel outflow) are prescribed. The Reynolds number of this example is given to $Re = u_{mean}D/\nu^f = 100$.

The fluid domain is discretized with fluid particles similar than in the example in Section 4.1.3 (initial particle spacing $\Delta x = 2.0 \times 10^{-3}$, support radius $r_c = 6.0 \times 10^{-3}$ of the smoothing kernel, artificial speed of sound $c = 12.5$, reference pressure $p_0 = 156.25$). In this example, the background pressure is set to $p_b = 1250.0$. Boundary particles according to [13] are utilized to model the bottom and top channel walls. The flexible beam as part of the structural domain is discretized by 35×3 first-order elements. The surface of the cylinder exposed to the fluid field, i.e., without considering the part where the flexible beam is attached, is discretized by 20 surface elements. Convergence of the iterative coupling of fluid and structural field is based on the tolerance $\epsilon = 1.0 \times 10^{-8}$, cf. Eq. (46). The FSI problem is solved for times $t \in [0, 12.0]$ with a time step size of $\Delta t = 4.0 \times 10^{-5}$. In this example, convergence of the partitioned coupling loop, cf. Algorithm 1, is reached after an average number of approximately 5.45 iterations per time step, when averaging over all time steps of the given problem.

The vertical displacement d_y of the control point at the tip of the flexible beam is displayed in Fig. 19. In the present results the minimum and maximum displacement of the control point at the tip of the flexible beam in y -direction are approximately -0.08269 and 0.08309 . This is in good agreement with the results given in the literature: [42] and [44] report a minimum and maximum displacement of -0.07937 and 0.08183 respectively -0.0803 and 0.0829 . The solution of the FSI problem shows time-periodic cycles of the beam deflection after approximately $t = 8.0$ with a cycle duration $t_{cycle} \approx 0.525$ and a frequency $f = 1/t_{cycle} \approx 1.905$ (averaged over all time-periodic cycles), which is in good agreement with [42,44] ($f = 1.90$). In Fig. 20 the magnitude of the fluid velocity field and the deformation of the structure for a periodic cycle from $t_0 = 10.32$ to $t_1 = 10.84$ at four equidistant points in time are shown. Especially, at times $t = 10.45$ and $t = 10.71$ the flexible beam experiences strong curvature. This is where approaches discretizing the structural domain by boundary particles fixed to structural material points suffer from a disturbed support of the smoothing kernel of neighboring fluid particles, cf. Fig. 3. The novel sliding boundary particle approach by definition is not prone to that issue. In summary, the results of the FSI benchmark problem obtained with the sliding boundary particle approach are both quantitatively and qualitatively in good agreement with the given reference solutions [42,44].

4.2.3. Inflation of an academic balloon-like problem

The filling process of a highly flexible thin-walled balloon-like container undergoing large deformations is studied in this example, representing a model problem close to potential application scenarios of the proposed scheme in the field of biomechanics.

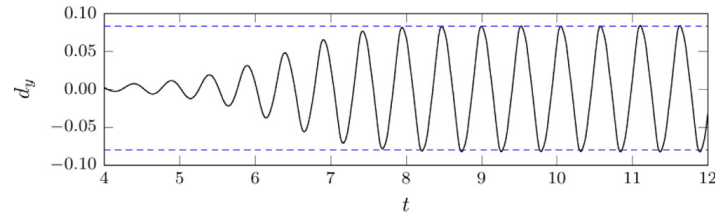


Fig. 19. Flow-induced oscillations of a flexible beam attached to a rigid cylinder: vertical displacement d_y of the control point at the tip of the flexible beam using the proposed sliding boundary particle approach (black solid line) compared to the minimum and maximum displacements given in reference solution [44] (blue dashed line).

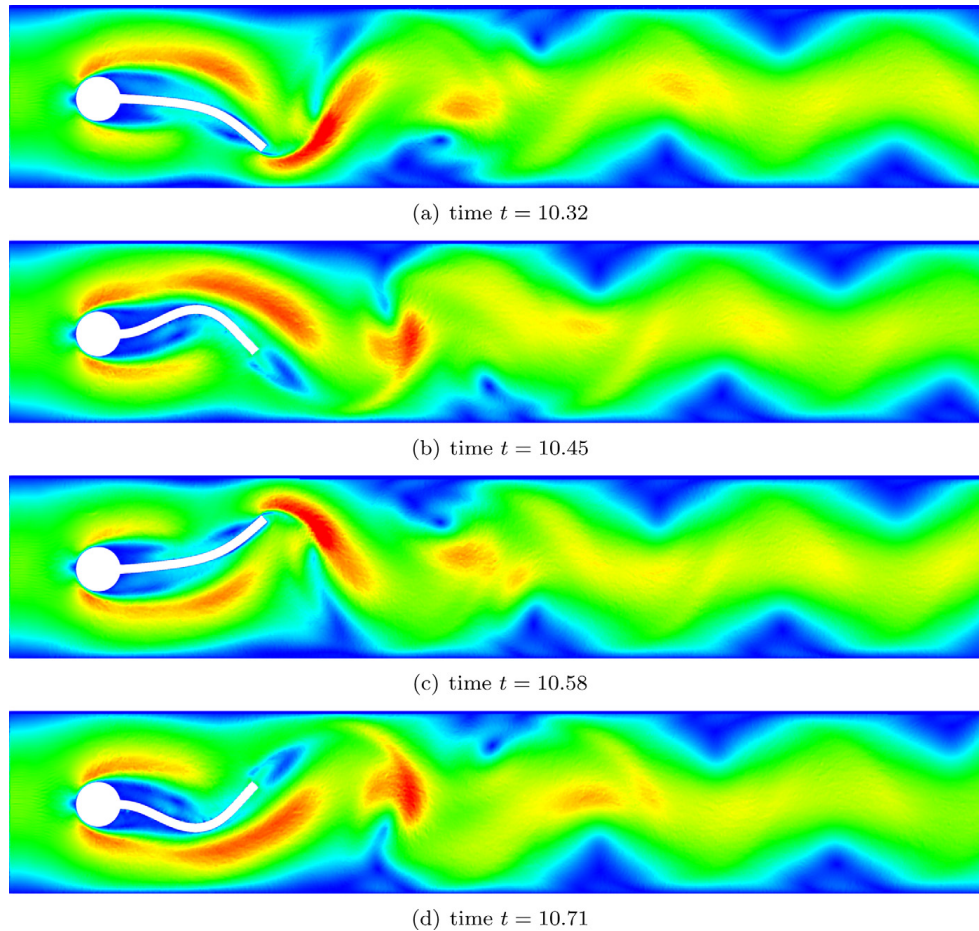


Fig. 20. Flow-induced oscillations of a flexible beam attached to a rigid cylinder: magnitude of the fluid velocity field ranging from 0.0 (blue) to 2.5 (red) and deformation of structure for a periodic cycle from $t_0 = 10.32$ to $t_1 = 10.84$ at four equidistant points in time. (For interpretation of the references to color in this figure legend, the reader is referred to the web version of this article.)

An initially cubical structural geometry with inner edge length $B = 3.0$ and wall thickness $d = 0.2$ is inflated via a quadratic inlet of width and length $b = 1.0$ by a Newtonian fluid that is initially at rest with density $\rho^f = 1.0$ and kinematic viscosity $\nu^f = 5.0 \times 10^{-1}$, cf. Fig. 21(a). The constitutive behavior of the structure with density $\rho_0^s = 1.0$ is described by a Saint Venant–Kirchhoff model with Young’s modulus $E^s = 1.0 \times 10^2$ and Poisson’s ratio $\nu^s = 0.45$. A similar problem was first proposed in [45] with the purpose to study and solve the incompressibility dilemma in partitioned fluid–structure interaction with pure Dirichlet fluid domains. This dilemma does not exist in our approach, given that SPH uses a weakly compressible approach. Here, the example is recapitulated on a three-dimensional geometry with modified fluid and structural material parameters. No-slip boundary conditions are applied at all fluid–structure interfaces. At the inflow of the balloon-like problem, a parabolic, time dependent

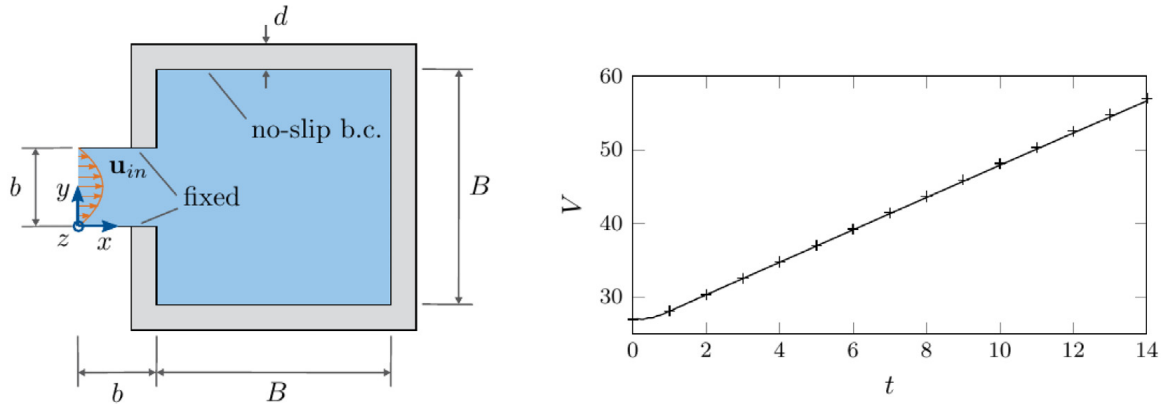


Fig. 21. Inflation of an academic balloon-like problem: geometry and boundary conditions of the problem based on [45] (left) and volume inside the academic balloon (solid line) compared to analytical solution (crosses) (right).

velocity profile $\mathbf{u}_{in} = \mathbf{u}(x = 0, y, z, t)$ with components

$$u_x(x = 0, y, z, t) = u_{max} \frac{4y(b - y)}{b^2} \frac{4z(b - z)}{b^2} \tau(t) \quad \text{and} \quad u_y(x = 0, y, z, t) = u_z(x = 0, y, z, t) = 0.0 \quad (51)$$

and maximum inflow velocity $u_{max} = 5.0$ and

$$\tau(t) = \begin{cases} \frac{1}{2}(1 - \cos(\pi t)) & \text{if } t < 1.0 \\ 1.0 & \text{otherwise} \end{cases} \quad (52)$$

is prescribed. Note that the origin of the coordinate system (x, y, z) is located at the bottom left corner of the inflow area. Accordingly, the volume inside the academic balloon (without considering the volume of the inlet) can be determined analytically via

$$V(t) = V_0 + \int_t \int_{A_{in}} u_x \, dA \, dt \quad (53)$$

for each time t with initial volume $V_0 = B^3$ and inflow area $A_{in} = b^2$.

The fluid domain is discretized by fluid particles with initial particle spacing $\Delta x = 4.0 \times 10^{-2}$. The smoothing length h is set equal to the initial particle spacing Δx resulting in a support radius $r_c = 1.2 \times 10^{-1}$ of the smoothing kernel. The artificial speed of sound is set to $c = 40.0$, hence the reference pressure is $p_0 = 1600.0$. The background pressure p_b is equal to the reference pressure p_0 . The walls of the fixed inlet are modeled utilizing boundary particles according to [13] with spacing equal to the initial particle spacing Δx . The balloon-like structural domain is discretized by first-order elements with a cubic shape in the initial configuration and a characteristic element length of d resulting in one element over the wall thickness. This discretization is justified since the focus of this example is set on the coupling of fluid and structural field at the interface rather than a precise prediction of structural quantities such as the deformation field of the tank. The tolerance $\epsilon = 1.0 \times 10^{-8}$ in Eq. (46) is applied for the iterative coupling of fluid and structural field. The FSI Problem is solved for times $t \in [0, 14.0]$ with a time step size of $\Delta t = 2.5 \times 10^{-4}$. In this example, convergence of the partitioned coupling loop, cf. Algorithm 1, is reached after an average number of approximately 5.88 iterations per time step, when averaging over all time steps of the given problem.

The volume inside the academic balloon is determined summing up the effective volumes of respective particles j following $V = \sum_j m_j / \rho_j$ and compared to the analytical solution (53), cf. Fig. 21(b). The resulting volume is slightly below the analytically determined volume. This can be explained by the weakly compressible approach, cf. Section 3.1.5, applied in this SPH formulation leading in this example to a minor compression of the fluid phase with an average density error of approximately 1%. Note that conservation of mass and accordingly (within the limits of a weakly compressible approach) conservation of volume is a characteristic property of SPH. By definition, this means that also the number of fluid particles is conserved. Therefore, the obtained results, among others, demonstrate that no leakage of fluid particles through the fluid–structure interface occurs. The rear half of the (inflated) structural geometry and a quarter section of the fluid domain are displayed in Fig. 22 in the initial

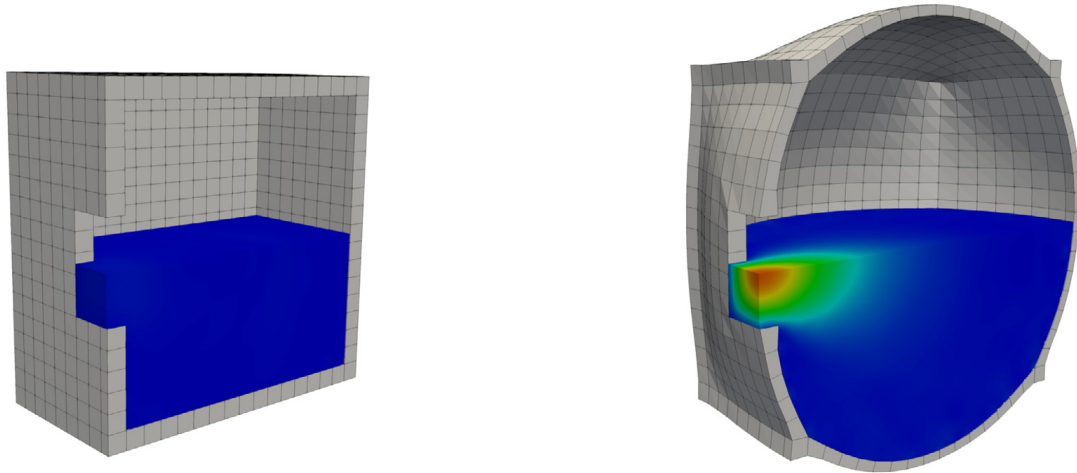


Fig. 22. Inflation of an academic balloon-like problem: magnitude of the fluid velocity field ranging from 0.0 (blue) to 5.0 (red) visualized on a quarter section of the fluid domain and deformation of structure at points in time $t_0 = 0.0$ (left) and $t_1 = 12.65$ (right). (For interpretation of the references to color in this figure legend, the reader is referred to the web version of this article.)

state and at time $t = 12.65$. The fluid velocity is post-processed applying SPH approximation (14). Note that at time $t = 12.65$ the volume inside the academic balloon has doubled, cf. analytical solution (53). In conclusion, this example is characterized by large structural deformations in form of strong curvature and stretch reaping the full benefits of the proposed sliding boundary particle approach in contrast to fixed (material) boundary particle methods. In the presence of large structural deformations, the latter class of boundary particle methods is characterized by insufficient kernel support, and eventually such methods are prone to leakage of fluid particles.

5. Conclusion and outlook

A novel smoothed particle hydrodynamics (SPH) and finite element (FE) coupling scheme for fluid–structure interaction, the sliding boundary particle approach, is presented in this publication. The coupled problem is solved via a Dirichlet–Neumann partitioned approach, with the fluid field (discretized via SPH) being the Dirichlet partition and the structural field (discretized via FE) being the Neumann partition. SPH is a mesh-free computational method that simplifies the treatment of both large deformations in the fluid domain as well as complex flow while avoiding additional methodological and computational effort compared to fully mesh-based methods. Introducing the sliding boundary particle approach for the treatment of deformable and strongly curved boundaries of the SPH domain in an accurate, robust, and computationally cheap manner, constitutes an important aspect of the proposed numerical formulation for solving FSI problems.

Several numerical examples showcase the capabilities of the novel numerical formulation. To begin with, the sliding boundary particle approach is validated examining two-dimensional examples driving certain characteristics of the proposed formulation. The numerical results obtained for the examples of a hydrostatic pressure in a fluid between two parallel plates, cf. Section 4.1.1, and a planar Taylor–Couette flow, cf. Section 4.1.2, are in very good agreement with the respective analytical solutions confirming the capability of the proposed method to model linear pressure profiles near the boundary and to account for no-slip boundary conditions at the boundary as required for high accuracy of the fluid velocity field. In a next step, numerical examples involving dynamic effects and large structural deformations are studied confirming the accuracy and robustness of the proposed formulation. This is, among others, demonstrated showing the results of well-known CFD respectively FSI benchmark problems, cf. Sections 4.1.3 and 4.2.2, as proposed in [38,42]. Altogether, the obtained numerical results are in very good agreement with the results given in the literature. Finally, a three-dimensional, application-focused example is considered examining the filling process of a highly flexible thin-walled container (cf. Section 4.2.3).

Future work may focus on an asynchronous time stepping scheme, e.g., a sub-cycling scheme of fluid and structural field, cf. Remark 14. Such an approach would allow to evolve the solution of the sub-fields with different time step sizes each best suitable for the underlying method respectively solver while reducing the overall computational effort. Besides that, the FSI framework may be extended to multiphase flow including the motion of

rigid bodies. The framework developed herein will be a valuable tool for detailed studies of biomechanical problems involving complex flow, e.g., the human stomach during digestion [1,2].

Declaration of competing interest

The authors declare that they have no known competing financial interests or personal relationships that could have appeared to influence the work reported in this paper.

Acknowledgments

Funded by the Deutsche Forschungsgemeinschaft (DFG, German Research Foundation) - Projektnummer 350481011, Projektnummer 257981274, Projektnummer 386349077. In addition we gratefully thank Georg Hammerl and Niklas Fehn for their preliminary work our particle implementation is based on, Jonas F. Eichinger for discussions concerning parallel programming concepts, Martin Kronbichler for his advice on code efficiency and performance, and Volker Gravemeier for discussions on various aspects in the field of computational fluid dynamics.

References

- [1] S. Brandstaeter, A. Gizzi, S.L. Fuchs, A.M. Gebauer, R.C. Aydin, C.J. Cyron, Computational model of gastric motility with active-strain electromechanics, *ZAMM-J. Appl. Math. Mech./Z. Angew. Math. Mech.* 98 (12) (2018) 2177–2197.
- [2] S. Brandstaeter, S.L. Fuchs, R.C. Aydin, C.J. Cyron, Mechanics of the stomach: A review of an emerging field of biomechanics, *GAMM-Mitt.* 42 (3) (2019) e201900001.
- [3] R.A. Gingold, J.J. Monaghan, Smoothed particle hydrodynamics: theory and application to non-spherical stars, *Mon. Not. R. Astron. Soc.* 181 (3) (1977) 375–389.
- [4] L.B. Lucy, A numerical approach to the testing of the fission hypothesis, *Astron. J.* 82 (1977) 1013–1024.
- [5] U. Küttler, W.A. Wall, Fixed-point fluid–structure interaction solvers with dynamic relaxation, *Comput. Mech.* 43 (1) (2008) 61–72.
- [6] P. Causin, J.-F. Gerbeau, F. Nobile, Added-mass effect in the design of partitioned algorithms for fluid–structure problems, *Comput. Methods Appl. Mech. Engrg.* 194 (42–44) (2005) 4506–4527.
- [7] C. Förster, W.A. Wall, E. Ramm, Artificial added mass instabilities in sequential staggered coupling of nonlinear structures and incompressible viscous flows, *Comput. Methods Appl. Mech. Engrg.* 196 (7) (2007) 1278–1293.
- [8] J.J. Monaghan, Simulating free surface flows with SPH, *J. Comput. Phys.* 110 (2) (1994) 399–406.
- [9] J.J. Monaghan, Smoothed particle hydrodynamics, *Rep. Progr. Phys.* 68 (8) (2005) 1703.
- [10] J.J. Monaghan, J.B. Kajtár, SPH particle boundary forces for arbitrary boundaries, *Comput. Phys. Comm.* 180 (10) (2009) 1811–1820.
- [11] P. Randles, L.D. Libersky, Smoothed particle hydrodynamics: some recent improvements and applications, *Comput. Methods Appl. Mech. Engrg.* 139 (1–4) (1996) 375–408.
- [12] J.P. Morris, P.J. Fox, Y. Zhu, Modeling low Reynolds number incompressible flows using SPH, *J. Comput. Phys.* 136 (1) (1997) 214–226.
- [13] S. Adami, X.Y. Hu, N.A. Adams, A generalized wall boundary condition for smoothed particle hydrodynamics, *J. Comput. Phys.* 231 (21) (2012) 7057–7075.
- [14] S. Kulasegaram, J. Bonet, R. Lewis, M. Profit, A variational formulation based contact algorithm for rigid boundaries in two-dimensional SPH applications, *Comput. Mech.* 33 (4) (2004) 316–325.
- [15] M. Ferrand, D. Laurence, B.D. Rogers, D. Violeau, C. Kassiotis, Unified semi-analytical wall boundary conditions for inviscid, laminar or turbulent flows in the meshless SPH method, *Internat. J. Numer. Methods Fluids* 71 (4) (2013) 446–472.
- [16] A. Mayrhofer, M. Ferrand, C. Kassiotis, D. Violeau, F.-X. Morel, Unified semi-analytical wall boundary conditions in SPH: analytical extension to 3-D, *Numer. Algorithms* 68 (1) (2015) 15–34.
- [17] M. Liu, G. Liu, Smoothed particle hydrodynamics (SPH): an overview and recent developments, *Arch. Comput. Methods Eng.* 17 (1) (2010) 25–76.
- [18] T. Ye, D. Pan, C. Huang, M. Liu, Smoothed particle hydrodynamics (SPH) for complex fluid flows: Recent developments in methodology and applications, *Phys. Fluids* 31 (1) (2019) 011301.
- [19] M. Müller, S. Schirm, M. Teschner, B. Heidelberger, M. Gross, Interaction of fluids with deformable solids, *Comput. Animat. Virtual Worlds* 15 (3–4) (2004) 159–171.
- [20] W. Hu, Q. Tian, H. Hu, Dynamic simulation of liquid-filled flexible multibody systems via absolute nodal coordinate formulation and SPH method, *Nonlinear Dynam.* 75 (4) (2014) 653–671.
- [21] Z. Li, J. Leduc, J. Nunez-Ramirez, A. Combescure, J.-C. Marongiu, A non-intrusive partitioned approach to couple smoothed particle hydrodynamics and finite element methods for transient fluid-structure interaction problems with large interface motion, *Comput. Mech.* 55 (4) (2015) 697–718.
- [22] G. Fourey, C. Hermange, D. Le Touzé, G. Oger, An efficient FSI coupling strategy between smoothed particle hydrodynamics and finite element methods, *Comput. Phys. Comm.* 217 (2017) 66–81.
- [23] T. Long, D. Hu, D. Wan, C. Zhuang, G. Yang, An arbitrary boundary with ghost particles incorporated in coupled FEM–SPH model for FSI problems, *J. Comput. Phys.* 350 (2017) 166–183.

- [24] BACI: A comprehensive multi-physics simulation framework, 2021, (accessed February 25, 2021). URL <https://baci.pages.gitlab.lrz.de/website>.
- [25] D.J. Price, Smoothed particle hydrodynamics and magnetohydrodynamics, *J. Comput. Phys.* 231 (3) (2012) 759–794.
- [26] N.J. Quinlan, M. Basa, M. Lastiwka, Truncation error in mesh-free particle methods, *Internat. J. Numer. Methods Engrg.* 66 (13) (2006) 2064–2085.
- [27] S. Adami, X.Y. Hu, N.A. Adams, A transport-velocity formulation for smoothed particle hydrodynamics, *J. Comput. Phys.* 241 (2013) 292–307.
- [28] M. Lastiwka, M. Basa, N.J. Quinlan, Permeable and non-reflecting boundary conditions in SPH, *Internat. J. Numer. Methods Fluids* 61 (7) (2009) 709–724.
- [29] T. Belytschko, W.K. Liu, B. Moran, K. Elkhodary, *Nonlinear Finite Elements for Continua and Structures*, John Wiley & Sons, 2013.
- [30] O.C. Zienkiewicz, R.L. Taylor, D. Fox, *The Finite Element Method for Solid and Structural Mechanics*, Elsevier/Butterworth-Heinemann, 2014.
- [31] T. Klöppel, A. Popp, U. Küttler, W.A. Wall, Fluid–structure interaction for non-conforming interfaces based on a dual mortar formulation, *Comput. Methods Appl. Mech. Engrg.* 200 (45–46) (2011) 3111–3126.
- [32] C. Meier, W.A. Wall, A. Popp, A unified approach for beam-to-beam contact, *Comput. Methods Appl. Mech. Engrg.* 315 (2017) 972–1010.
- [33] T.J. Hughes, J.A. Cottrell, Y. Bazilevs, Isogeometric analysis: CAD, finite elements, NURBS, exact geometry and mesh refinement, *Comput. Methods Appl. Mech. Engrg.* 194 (39–41) (2005) 4135–4195.
- [34] J.A. Cottrell, T.J. Hughes, Y. Bazilevs, *Isogeometric Analysis: Toward Integration of CAD and FEA*, John Wiley & Sons, 2009.
- [35] J.F. Hughes, T. Moller, Building an orthonormal basis from a unit vector, *J. Graph. Tools* 4 (4) (1999) 33–35.
- [36] M. Hashemi, R. Fatehi, M. Manzari, A modified SPH method for simulating motion of rigid bodies in Newtonian fluid flows, *Int. J. Non-Linear Mech.* 47 (6) (2012) 626–638.
- [37] A.C. Limache, P.J. Sánchez, L.D. Dalcín, S.R. Idelsohn, Objectivity tests for navier–stokes simulations: The revealing of non-physical solutions produced by laplace formulations, *Comput. Methods Appl. Mech. Engrg.* 197 (49–50) (2008) 4180–4192.
- [38] M. Schäfer, S. Turek, F. Durst, E. Krause, R. Rannacher, Benchmark computations of laminar flow around a cylinder, in: *Flow Simulation with High-Performance Computers II*, Springer, 1996, pp. 547–566.
- [39] S. Turek, *Flow Around a Cylinder*, FEATFLOW Homepage, 2020, (accessed October 15, 2020).
- [40] J. Feng, H.H. Hu, D.D. Joseph, Direct simulation of initial value problems for the motion of solid bodies in a Newtonian fluid. Part 2. Couette and poiseuille flows, *J. Fluid Mech.* 277 (1994) 271–301.
- [41] Z.-G. Feng, E.E. Michaelides, Interparticle forces and lift on a particle attached to a solid boundary in suspension flow, *Phys. Fluids* 14 (1) (2002) 49–60.
- [42] S. Turek, J. Hron, Proposal for numerical benchmarking of fluid-structure interaction between an elastic object and laminar incompressible flow, in: *Fluid-Structure Interaction*, Springer, 2006, pp. 371–385.
- [43] E. Ramm, W. Wall, Fluid-structure interaction based upon a stabilized (ALE) finite element method, in: *4th World Congress on Computational Mechanics: New Trends and Applications*, CIMNE, Barcelona, 1998, pp. 1–20.
- [44] S. Turek, *Numerical Benchmarking of Fluid-Structure Interaction between an Elastic Object and Laminar Incompressible Flow*, FEATFLOW Homepage, 2020, (accessed October 15, 2020).
- [45] U. Küttler, C. Förster, W.A. Wall, A solution for the incompressibility dilemma in partitioned fluid–structure interaction with pure Dirichlet fluid domains, *Comput. Mech.* 38 (4) (2006) 417–429.

A.2 Paper B

An SPH framework for fluid-solid and contact interaction problems including thermo-mechanical coupling and reversible phase transitions

Sebastian L. Fuchs, Christoph Meier, Wolfgang A. Wall, Christian J. Cyron

*Reprinted from S. L. Fuchs, C. Meier, W. A. Wall, and C. J. Cyron. An SPH framework for fluid-solid and contact interaction problems including thermo-mechanical coupling and reversible phase transitions. *Advanced Modeling and Simulation in Engineering Sciences*, 8(1):15, 2021, licensed under the Creative Commons Attribution License 4.0 (<https://creativecommons.org/licenses/by/4.0/>).*

RESEARCH ARTICLE

Open Access



An SPH framework for fluid–solid and contact interaction problems including thermo-mechanical coupling and reversible phase transitions

Sebastian L. Fuchs^{1,2} , Christoph Meier¹ , Wolfgang A. Wall¹  and Christian J. Cyron^{2,3*} 

*Correspondence:
christian.cyron@hereon.de
³Institute of Material Systems
Modeling, Helmholtz-Zentrum
Hereon, Max-Planck-Straße 1,
21502 Geesthacht, Germany
Full list of author information is
available at the end of the article

Abstract

The present work proposes an approach for fluid–solid and contact interaction problems including thermo-mechanical coupling and reversible phase transitions. The solid field is assumed to consist of several arbitrarily-shaped, undeformable but mobile rigid bodies, that are evolved in time individually and allowed to get into mechanical contact with each other. The fluid field generally consists of multiple liquid or gas phases. All fields are spatially discretized using the method of smoothed particle hydrodynamics (SPH). This approach is especially suitable in the context of continually changing interface topologies and dynamic phase transitions without the need for additional methodological and computational effort for interface tracking as compared to mesh- or grid-based methods. Proposing a concept for the parallelization of the computational framework, in particular concerning a computationally efficient evaluation of rigid body motion, is an essential part of this work. Finally, the accuracy and robustness of the proposed framework is demonstrated by several numerical examples in two and three dimensions, involving multiple rigid bodies, two-phase flow, and reversible phase transitions, with a focus on two potential application scenarios in the fields of engineering and biomechanics: powder bed fusion additive manufacturing (PBFAM) and disintegration of food boluses in the human stomach. The efficiency of the parallel computational framework is demonstrated by a strong scaling analysis.

Keywords: Rigid body motion, Two-phase flow, Reversible phase transitions, Smoothed particle hydrodynamics, Metal additive manufacturing, Gastric fluid mechanics

Introduction

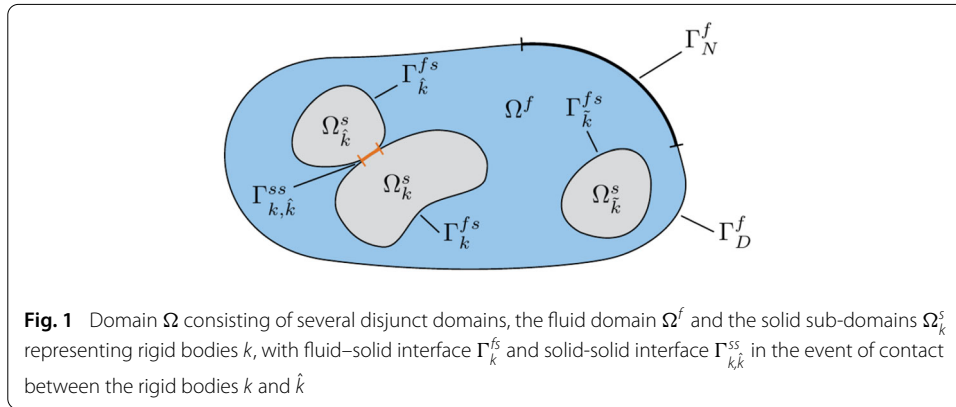
In many applications in science and engineering, like for example in some areas of biomechanics, fluid–solid and contact interaction problems characterized by a large number of solid bodies immersed in a fluid flow and undergoing reversible phase transitions, are of great interest. Often, explicitly considering the deformation of solid bodies can be neglected, which reduces the complexity of the problem to the treatment of unde-

formable but mobile rigid bodies, in favor of simplified modeling. Most current mesh- or grid-based methods, e.g., the finite element method (FEM), the finite difference method (FDM), or the finite volume method (FVM), require substantial methodological and computational efforts to model the motion of rigid bodies in fluid flow. To overcome those issues, several approaches, e.g., based on the particle finite element method (PFEM) [1–3], on the discrete element method (DEM) [4–7], or on smoothed particle hydrodynamics (SPH) [8–14], have been proposed. SPH as a mesh-free discretization scheme is, due to its Lagrangian nature, very well suited for flow problems involving multiple phases, dynamic and reversible phase transitions, and complex interface topologies. This makes SPH very appropriate for a wide range of applications in engineering, e.g., in metal additive manufacturing melt pool modeling [15, 16], or in biomechanics, e.g., for modeling the digestion of food in the human stomach [17]. For the former application, an SPH formulation for thermo-capillary phase transition problems involving solid, liquid, and gaseous phases has recently been proposed [18], amongst others, focusing on evaporation-induced recoil pressure forces, temperature-dependent surface tension and wetting forces, Gaussian laser beam heat sources, and evaporation-induced heat losses. However, for simplicity, this and also other current state-of-the-art approaches, e.g., [19, 20] are restricted to immobile powder grains.

All aforementioned SPH formulations for modeling rigid body motion in fluid flow have in common, that rigid bodies are fully resolved, that is spatially discretized as clusters of particles. It is generally accepted that advanced boundary particle methods, e.g., based on the extrapolation of field quantities from fluid to boundary particles [21–23], are beneficial, because one can model the fluid field close to the boundary with high accuracy. In many of the aforementioned applications, an exact representation of the fluid–solid interface plays an important role. Therefore, herein a formulation of this kind proposed in [23] is utilized. To the best of the authors' knowledge none of the aforementioned SPH formulations modeling rigid body motion in fluid flow simultaneously consider thermal conduction, reversible phase transitions, and multiple (liquid and gas) phases.

To help close this gap, this contribution proposes a fully resolved smoothed particle hydrodynamics framework for fluid–solid and contact interaction problems including thermo-mechanical coupling and reversible phase transitions. The solid field is assumed to consist of several arbitrarily-shaped, undeformable but mobile rigid bodies, that are evolved in time individually. Based on a temperature field, provided by solving the heat equation, reversible phase transitions, i.e., melting and solidification, are evaluated between the fluid and the solid field. As a result, the shape and the total number of rigid bodies may vary over time. In addition, contact between rigid bodies is considered by employing a spring-dashpot model. Note that some characteristic phenomena for thermo-capillary flow [24, 25] and, especially, for metal PBFAM melt pool modeling [18–20, 26–28] are not addressed in this work, thus, referring to the literature.

While parallel implementation aspects along with detailed scalability studies are not in the focus of the aforementioned references, in this work, a concept for the parallelization of the computational framework is proposed, setting the focus in particular on an efficient evaluation of rigid body motion. The parallel behavior is demonstrated, confirming that detailed studies at a large scale become possible. It shall be noted, that the parallel implementation of such a computational framework is far from trivial but indispensable when examining numerical examples that are of practical relevance. Note that the introduced



concept for the parallelization of the computational framework is applicable not only when using SPH as a discretization scheme, but also for other particle-based methods, e.g., discrete element method (DEM), or molecular dynamics (MD).

The remainder of this work is organized as follows: To begin with, the governing equations for a fluid–solid and contact interaction problem including thermo-mechanical coupling and reversible phase transition are outlined. Next, the numerical methods are presented and the details of the computational framework are discussed. Finally, the accuracy and robustness of the proposed formulation is demonstrated by several numerical examples.

Governing equations

Consider a domain Ω of a fluid–solid interaction problem that consists at each time $t \in [0, T]$ of the non-overlapping fluid domain Ω^f and solid domain Ω^s that share a common interface Γ^{fs} , with $\Omega = \Omega^f \cup \Omega^s$ and $\Omega^f \cap \Omega^s = \Gamma^{fs}$. In general, the fluid domain Ω^f may consist of multiple (liquid and gas) phases. For ease of notation, in the following it will not be distinguished between the different fluid phases. The solid domain Ω^s is composed of several non-overlapping sub-domains Ω_k^s , which represent rigid bodies k , such that $\Omega^s = \bigcup_k \Omega_k^s$. In the event of contact between two rigid bodies k and \hat{k} , a common interface $\Gamma_{k,\hat{k}}^{ss} = \Omega_k^s \cap \Omega_{\hat{k}}^s$ exists, separating the two solid sub-domains Ω_k^s and $\Omega_{\hat{k}}^s$. A detailed illustration of the problem is given in Fig. 1. In the following the (standard) governing equations of the fluid and the solid field as well as the respective coupling conditions are briefly given. In addition, reversible phase transitions between the fluid and the solid field, e.g., temperature-induced melting and solidification, may occur. For this reason, the temperature field is modeled solving the heat equation.

Fluid field

The fluid field is governed by the instationary Navier–Stokes equations in the domain Ω^f , which consist in convective form of the mass continuity equation and the momentum equation

$$\frac{d\rho^f}{dt} = -\rho^f \nabla \cdot \mathbf{u}^f \quad \text{in } \Omega^f, \tag{1}$$

$$\frac{d\mathbf{u}^f}{dt} = -\frac{1}{\rho^f} \nabla_p^f + \mathbf{f}_v + \mathbf{b}^f \quad \text{in } \Omega^f, \tag{2}$$

with viscous force \mathbf{f}_v and body force \mathbf{b}^f each per unit mass. For a Newtonian fluid the viscous force is $\mathbf{f}_v = \nu^f \nabla^2 \mathbf{u}^f$ with kinematic viscosity ν^f . The mass continuity equation (1) and the momentum equation (2) represent a system of $d + 1$ equations with the $d + 2$ unknowns, velocity \mathbf{u}^f , density ρ^f , and pressure p^f , in d -dimensional space. The system of equations is closed with an equation of state $p^f = p^f(\rho^f)$ relating fluid density ρ^f and pressure p^f . The Navier–Stokes equations (1) and (2) are subject to the following initial conditions

$$\rho^f = \rho_0^f \quad \text{and} \quad \mathbf{u}^f = \mathbf{u}_0^f \quad \text{in} \quad \Omega^f \quad \text{at} \quad t = 0 \tag{3}$$

with initial density ρ_0^f and initial velocity \mathbf{u}_0^f . In addition, Dirichlet and Neumann boundary conditions are applied on the fluid boundary $\Gamma^f = \partial\Omega^f \setminus \Gamma^{fs}$

$$\mathbf{u}^f = \hat{\mathbf{u}}^f \quad \text{on} \quad \Gamma_D^f \quad \text{and} \quad \mathbf{t}^f = \hat{\mathbf{t}}^f \quad \text{on} \quad \Gamma_N^f, \tag{4}$$

with prescribed boundary velocity $\hat{\mathbf{u}}^f$ and boundary traction $\hat{\mathbf{t}}^f$, where $\Gamma^f = \Gamma_D^f \cup \Gamma_N^f$ and $\Gamma_D^f \cap \Gamma_N^f = \emptyset$. Furthermore, on the fluid–solid interface $\Gamma^{fs} = \bigcup_k \Gamma_k^{fs}$ the so-called kinematic and dynamic coupling conditions are

$$\mathbf{u}^f = \mathbf{u}_k^{fs} \quad \text{and} \quad \mathbf{t}^f = \mathbf{t}_k^{fs} \quad \text{on} \quad \Gamma_k^{fs} \quad \forall k, \tag{5}$$

resembling a no-slip boundary condition and ensuring equilibrium of fluid and solid traction across the interface Γ^{fs} . Herein, \mathbf{u}_k^{fs} and \mathbf{t}_k^{fs} denote the velocity respectively traction of a rigid body k on the fluid–solid interface Γ_k^{fs} .

Remark 1 In Eqs. (1)–(2) governing the fluid field, all time derivatives follow the motion of material points, i.e., are material derivatives $\frac{d(\cdot)}{dt} = \frac{\partial(\cdot)}{\partial t} + \mathbf{u} \cdot \nabla(\cdot)$. Besides, $\nabla(\cdot)$ denotes derivatives with respect to spatial coordinates.

Solid field

The solid field is assumed to consist of several mobile rigid bodies k each represented by a sub-domain Ω_k^s embedded in the fluid domain Ω^f . Thus, the interface of a rigid body k is $\Gamma_k^s = \Gamma_k^{fs} \cup \left(\bigcup_{\hat{k}} \Gamma_{k,\hat{k}}^{ss} \right)$ with contacting rigid bodies \hat{k} , cf. Fig. 1. The kinematics of each rigid body k are uniquely defined by three respectively six degrees of freedom in two- and three-dimensional space, i.e., the position of the center of mass \mathbf{r}_k^s and the orientation $\boldsymbol{\psi}_k^s$. As a result, the equations of motion of an individual rigid body k are described by the balance of linear and angular momentum

$$m_k^s \frac{d^2 \mathbf{r}_k^s}{dt^2} = \mathbf{f}_k^{fs} + \sum_{\hat{k}} \mathbf{f}_{k,\hat{k}}^{ss} + m_k^s \mathbf{b}_k^s \quad \text{in} \quad \Omega_k^s, \tag{6}$$

$$\mathbf{I}_k^s \frac{d\boldsymbol{\omega}_k^s}{dt} = \mathbf{m}_k^{fs} + \sum_{\hat{k}} \mathbf{m}_{k,\hat{k}}^{ss} \quad \text{in} \quad \Omega_k^s, \tag{7}$$

with mass m_k^s and mass moment of inertia \mathbf{I}_k^s with respect to the center of mass position \mathbf{r}_k^s . Herein, $\boldsymbol{\omega}_k^s$ denotes the angular velocity of a rigid body k , cf. Remark 2. Furthermore, \mathbf{f}_k^{fs} and \mathbf{m}_k^{fs} describe the resultant coupling force respectively torque acting on the fluid–solid interface Γ_k^{fs} of rigid body k . Contacting rigid bodies k and \hat{k} exchange the resultant

contact force $\mathbf{f}_{k,k}^{ss}$ respectively torque $\mathbf{m}_{k,k}^{ss}$ at the solid-solid interface $\Gamma_{k,k}^{ss}$. Finally, the body force \mathbf{b}_k^s given per unit mass is contributing to the balance of linear momentum.

Remark 2 The orientation $\boldsymbol{\psi}_k^s$ is expressed by a (pseudo-)vector whose direction and magnitude represent the axis and angle of rotation. Note that in general, the angular velocity $\boldsymbol{\omega}_k^s$ of a rigid body k is different from the time derivative of the orientation $\boldsymbol{\psi}_k^s$, i.e., $\boldsymbol{\omega}_k^s \neq d\boldsymbol{\psi}_k^s/dt$, due to the non-additivity of large rotations [29–32]. Direct evolution of the orientation $\boldsymbol{\psi}_k^s$ of a rigid body k requires a special class of time integration schemes, so-called Lie group time integrators [33,34].

Thermal conduction

Thermal conduction in the combined fluid and solid domain $\Omega = \Omega^f \cup \Omega^s$ in the absence of heat sources or heat sinks (which are neglected herein for simplicity) is governed by the heat equation

$$c_p^\phi \frac{dT}{dt} = \frac{1}{\rho^\phi} \nabla(\kappa^\phi \nabla T) \quad \text{in } \Omega, \tag{8}$$

with temperature T and heat flux $\mathbf{q} = -\kappa^\phi \nabla T$. The material parameters heat capacity c_p^ϕ and thermal conductivity κ^ϕ are in general different for fluid and solid field, and hence for clarity are denoted by the index $(\cdot)^\phi$ with $\phi \in \{f, s\}$. The heat equation (8) is subject to the following initial condition

$$T = T_0 \quad \text{in } \Omega \quad \text{at } t = 0 \tag{9}$$

with initial temperature T_0 . In addition, Dirichlet and Neumann boundary conditions are required on the domain boundary $\Gamma = \partial\Omega$

$$T = \hat{T} \quad \text{on } \Gamma_D \quad \text{and} \quad \mathbf{q} = \hat{\mathbf{q}} \quad \text{on } \Gamma_N, \tag{10}$$

with prescribed boundary temperature \hat{T} and boundary heat flux $\hat{\mathbf{q}}$, where $\Gamma = \Gamma_D \cup \Gamma_N$ and $\Gamma_D \cap \Gamma_N = \emptyset$.

Reversible phase transition

Reversible phase transitions, i.e., melting and solidification, are considered between the solid and the fluid field. Within this publication, solid material points that exceed a transition temperature T_t undergo a phase transition to a fluid material point and vice versa, cf. Remark 3. Consequently, the shape of a rigid body k , i.e., its sub-domain Ω_k^s , is changing due to a loss or gain of material points resulting in a varying mass m_k , center of mass position \mathbf{r}_k , and mass moment of inertia \mathbf{I}_k .

Remark 3 For the sake of simplicity, only temperature-independent parameters are considered herein, and latent heat is neglected. Latent heat could be included by an apparent capacity scheme relying on an increased heat capacity c_p within a finite temperature interval [35] in a straightforward manner.

Remark 4 The proposed framework is general enough to model also chemically-induced phase transitions based on a concentration field. For this purpose, the diffusion equation

$dC/dt = 1/\rho^\phi \nabla(D^\phi \nabla C)$ with diffusivity D^ϕ modeling the transport of a concentration C is solved. Considering the similarity between the heat equation (8) and the diffusion equation, the latter can be discretized following a similar SPH discretization [36,37] as applied for the heat equation. Similarly, modeling phase transitions a transition concentration C_t is defined.

Numerical methods and parallel computational framework

This section presents the methods applied for discretization and numerical solution of fluid–solid and contact interaction problems including thermo-mechanical coupling and reversible phase transitions. The presented parallel computational framework is implemented in the in-house parallel multiphysics research code BACI (Bavarian Advanced Computational Initiative) [38] using the Message Passing Interface (MPI) for distributed-memory parallel programming.

Spatial discretization via smoothed particle hydrodynamics

For the spatial discretization smoothed particle hydrodynamics (SPH) is used, allowing for a straightforward particle-based evaluation of fluid–solid coupling conditions. In the following, the basics of this method are recapitulated briefly.

Approximation of field quantities applying a smoothing kernel

The fundamental concept of SPH is based on the approximation of a field quantity f via a smoothing operation and on the discretization of the domain Ω with discretization points, so-called particles j , each occupying a volume V_j . Introducing a smoothing kernel $W(r, h)$ that fulfills certain consistency properties [36,39], cf. Remark 5, leads to an approximation of the field quantity f based on summation of contributions from all particles j in the domain Ω

$$f(\mathbf{r}) \approx \int_{\Omega} f(\mathbf{r}') W(|\mathbf{r} - \mathbf{r}'|, h) d\mathbf{r}' \approx \sum_j V_j f(\mathbf{r}_j) W(|\mathbf{r} - \mathbf{r}_j|, h) \quad (11)$$

which includes a smoothing error and a discretization error [40].

Remark 5 The smoothing kernel $W(r, h)$ is a monotonically decreasing, smooth function that depends on a distance r and a smoothing length h . The smoothing length h together with a scaling factor κ define the support radius $r_c = \kappa h$ of the smoothing kernel. Compact support, i.e., $W(r, h) = 0$ for $r > r_c$, as well as positivity, i.e., $W(r, h) \geq 0$ for $r \leq r_c$, are typical properties of standard smoothing kernels $W(r, h)$. In addition, the normalization property requires that $\int_{\Omega} W(|\mathbf{r} - \mathbf{r}'|, h) d\mathbf{r}' = 1$. The Dirac delta function property $\lim_{h \rightarrow 0} W(r, h) = \delta(r)$ ensures an exact representation of a field quantity f in the limit $h \rightarrow 0$.

A straightforward approach in SPH to determine the gradient of a quantity f follows directly by differentiation of (11) resulting in

$$\nabla f(\mathbf{r}) \approx \int_{\Omega} f(\mathbf{r}') \nabla W(|\mathbf{r} - \mathbf{r}'|, h) d\mathbf{r}' \approx \sum_j V_j f(\mathbf{r}_j) \nabla W(|\mathbf{r} - \mathbf{r}_j|, h). \quad (12)$$

Note that this (simple) gradient approximation shows some particular disadvantages. Hence, more advanced approximations for gradients are given in the literature [36] and will also be applied in the following. In sum, the concept of SPH allows to reduce partial differential equations to a system of coupled ordinary differential equations (with as many equations as particles) that is solved in the domain Ω . Thereby, all field quantities are evaluated at and associated with particle positions, meaning each particle carries its corresponding field quantities. Finally, in a post-processing step a continuous field quantity f is recovered from the discrete quantities $f(\mathbf{r}_j)$ of particles j in the domain Ω using the approximation (11) and the commonly known Shepard filter

$$\hat{f}(\mathbf{r}) \approx \frac{\sum_j V_j f(\mathbf{r}_j) W(|\mathbf{r} - \mathbf{r}_j|, h)}{\sum_j V_j W(|\mathbf{r} - \mathbf{r}_j|, h)}. \quad (13)$$

Note that the denominator typically takes on values close to one inside the fluid domain and is mainly relevant for boundary regions with reduced support due to a lack of neighboring particles.

Remark 6 In the following, a quantity f evaluated for particle i at position \mathbf{r}_i is written as $f_i = f(\mathbf{r}_i)$. The short notation $W_{ij} = W(r_{ij}, h)$ denotes the smoothing kernel W evaluated for particle i at position \mathbf{r}_i with neighboring particle j at position \mathbf{r}_j , where $r_{ij} = |\mathbf{r}_{ij}| = |\mathbf{r}_i - \mathbf{r}_j|$ is the absolute distance between particles i and j . The derivative of the smoothing kernel W with respect to the absolute distance r_{ij} is denoted by $\partial W / \partial r_{ij} = \partial W(r_{ij}, h) / \partial r_{ij}$.

Remark 7 Herein, a quintic spline smoothing kernel $W(r, h)$ as defined in [21] with smoothing length h and compact support of the smoothing kernel with support radius $r_c = \kappa h$ and scaling factor $\kappa = 3$ is used.

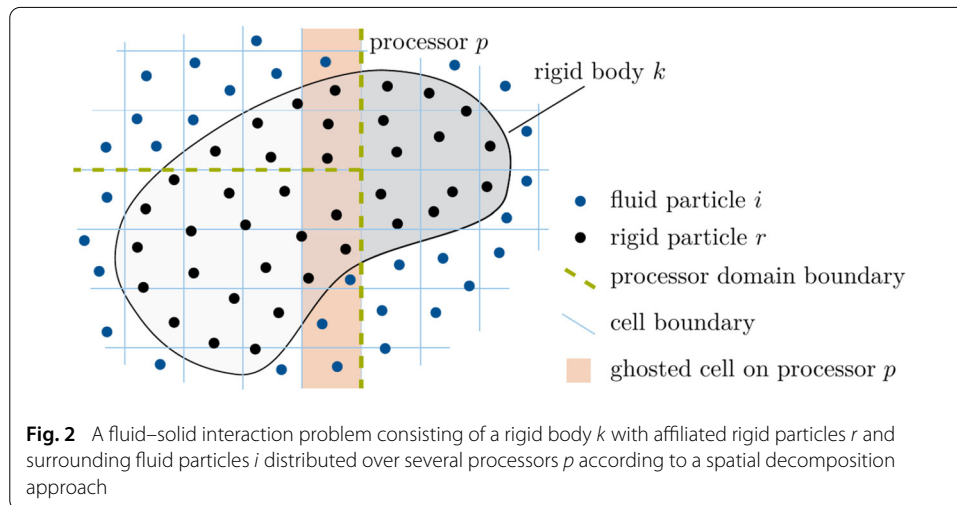
Initial particle spacing

Within this contribution, the domain Ω is initially filled with particles located on a regular grid with particle spacing Δx , thus in the d -dimensional space each particle initially occupies an effective volume $V_{eff} = (\Delta x)^d$. A particle in the fluid domain Ω^f is called a fluid particle i , whereas a particle in the solid domain Ω_k^s of a rigid body k is called a rigid particle r . It follows, that each rigid body is fully resolved being spatially discretized as clusters of particles. Naturally, the choice of the particle spacing Δx influences the accuracy of the interface representation between fluid and solid domain. The mass of a particle is initially assigned using the reference density of the respective phase, i.e., ρ_0^f for the fluid phase and ρ_0^s for the solid phase, and the effective volume V_{eff} .

Remark 8 Within this work, the smoothing length h of the smoothing kernel $W(r, h)$, cf. Remark 7, is set equal to the initial particle spacing Δx . Consequently, in a convergence analysis with decreasing particle spacing Δx the ratio $\Delta x/h$ remains constant [40].

Parallelization via spatial decomposition of the domain

For the problems studied herein, an efficient parallel computational framework capable of handling systems constituted of a large number of particles is required. This requires addressing in particular two aspects, namely, an efficient particle neighbor pair detection,



and a parallel load distribution strategy while keeping the communication overhead at an acceptable level. In the literature, several approaches for parallel computational frameworks utilizing particle-based methods have been proposed, e.g., [41–47]. In the present work, a spatial decomposition approach with neighbor pair detection utilizing a combination of cell-linked lists and Verlet-lists based on [42] is applied. The general idea of the spatial decomposition approach is briefly explained in the following, however, for detailed information, the interested reader is referred to the original publication [42]. In addition, the concept is extended herein to consider the motion of rigid bodies spatially discretized as clusters of particles.

The evaluation of particle interactions in SPH requires knowledge of neighboring particles within a geometrically limited interaction distance, i.e., within the support radius r_c of the smoothing kernel. Thus, the computational domain is divided into several cubic cells forming a uniform lattice, while each particle is uniquely assigned to one of those cells according to its current spatial position, cf. Fig. 2. The size of the cells is chosen such that neighboring particles are either located in the same cell or in adjacent cells, i.e., the size of the cells is at least equal to the support radius r_c of the smoothing kernel.

Following a spatial decomposition approach, the cells together with assigned particles are distributed over all involved processors, i.e., forming so-called processor domains. To keep the computational load balanced between all processors and to minimize the communication overhead, cubic processor domains are defined such that each contains (nearly) the same number of particles. The cells occupied by each processor are called owned cells. On each processor the position of particles located in its processor domain, i.e., the position of so-called owned particles, is evolved. This requires the evaluation of interactions of owned particles with their neighboring particles. However, the correct evaluation of particle interactions close to processor domain boundaries requires that each processor has information not only about its owned particles but also about particles in cells adjacent to its processor domain. To this end, each processor is provided full information not only about its own domain but additionally about a layer of ghosted cells (with ghosted particles) around its own domain. Keeping the information about ghosted cells and particles continuously updated requires communication between processors.

Remark 9 To exemplify the cost of communication overhead, consider a perfectly cubic processor domain occupying n_o owned cells. Consequently, assuming one layer of ghosted cells surrounding the processor domain, a total of $n_g = (\sqrt[3]{n_o} + 2)^3 - n_o$ cells are ghosted. That is, the communication overhead scales with the ratio n_g/n_o of ghosted cells n_g to owned cells n_o . Furthermore, the (average) number of particles per cell, and, consequently, also the communication overhead, scale with the ratio $r_c/\Delta x$ of the support radius r_c and the initial particle spacing Δx .

As a consequence of the spatial decomposition approach, the affiliated rigid particles r of a rigid body k might be distributed over several processors, cf. Fig. 2. However, note that the balance of linear and angular momentum, cf. Eqs. (6)–(7), describing the motion of a rigid body k are given with respect to the center of mass position \mathbf{r}_k^s . Thus, the evaluation of mass quantities, i.e., mass m_k , center of mass position \mathbf{r}_k^s , and mass moment of inertia \mathbf{I}_k , as well as the evaluation of resultant force \mathbf{f}_k and torque \mathbf{m}_k acting on a rigid body k , requires special communication between all processors hosting rigid particles r belonging to rigid body k and the single processor owning rigid body k .

Modeling fluid flow using weakly compressible SPH

For modeling fluid flow using SPH, several different formulations each with its own characteristics and benefits can be derived. Here, the instationary Navier–Stokes equations (1) and (2) are discretized by a weakly compressible approach [36,39,48]. This section gives a brief overview of this formulation applied already in [18,49]. For ease of notation, in the following the index $(\cdot)^f$ denoting fluid quantities is dropped.

Density summation

The density of a particle i is determined via summation of the respective smoothing kernel contributions of all neighboring particles j within the support radius r_c

$$\rho_i = m_i \sum_j W_{ij} \quad (14)$$

with mass m_i of particle i . This approach is typically denoted as density summation and results in an exact conservation of mass in the fluid domain, which can be shown in a straightforward manner considering the commonly applied normalization of the smoothing kernel to unity. It shall be noted that the density field may alternatively be obtained by discretization and integration of the mass continuity equation (1) [39].

Momentum equation

The momentum equation (2) is discretized following [23,50] including a transport velocity formulation to suppress the problem of tensile instability. It will be briefly recapitulated in the following. The transport velocity formulation relies on a constant background pressure p_b that is applied to all particles and results in a contribution to the particle accelerations for in general disordered particle distributions. However, these additional acceleration contributions vanish for particle distributions fulfilling the partition of unity of the smoothing kernel, thus fostering these desirable configurations. For the sake of brevity, the definition of the modified advection velocity and the additional terms in the momentum equation from the aforementioned transport velocity formulation are not

discussed in the following and the reader is referred to the original publication [50]. Altogether, the acceleration $\mathbf{a}_i = d\mathbf{u}_i/dt$ of a particle i results from summation of all acceleration contributions due to interaction with neighboring particles j and a body force as

$$\mathbf{a}_i = \frac{1}{m_i} \sum_j (V_i^2 + V_j^2) \left[-\tilde{p}_{ij} \frac{\partial W}{\partial r_{ij}} \mathbf{e}_{ij} + \tilde{\eta}_{ij} \frac{\mathbf{u}_{ij}}{r_{ij}} \frac{\partial W}{\partial r_{ij}} \right] + \mathbf{b}_i, \quad (15)$$

with volume $V_i = m_i/\rho_i$ of particle i , unit vector $\mathbf{e}_{ij} = \mathbf{r}_i - \mathbf{r}_j/|\mathbf{r}_i - \mathbf{r}_j| = \mathbf{r}_{ij}/r_{ij}$, relative velocity $\mathbf{u}_{ij} = \mathbf{u}_i - \mathbf{u}_j$, and density-weighted inter-particle averaged pressure and inter-particle averaged viscosity

$$\tilde{p}_{ij} = \frac{\rho_j p_i + \rho_i p_j}{\rho_i + \rho_j} \quad \text{and} \quad \tilde{\eta}_{ij} = \frac{2\eta_i \eta_j}{\eta_i + \eta_j}. \quad (16)$$

In the following, the acceleration contribution of a neighboring particle j to particle i is, for ease of notation, denoted as \mathbf{a}_{ij} , where $\mathbf{a}_i = \sum_j \mathbf{a}_{ij} + \mathbf{b}_i$. The above given momentum equation (15) exactly conserves linear momentum due to pairwise anti-symmetric particle forces

$$m_i \mathbf{a}_{ij} = -m_j \mathbf{a}_{ji}, \quad (17)$$

which follows from the property $\partial W/\partial r_{ij} = \partial W/\partial r_{ji}$ of the smoothing kernel.

Equation of state

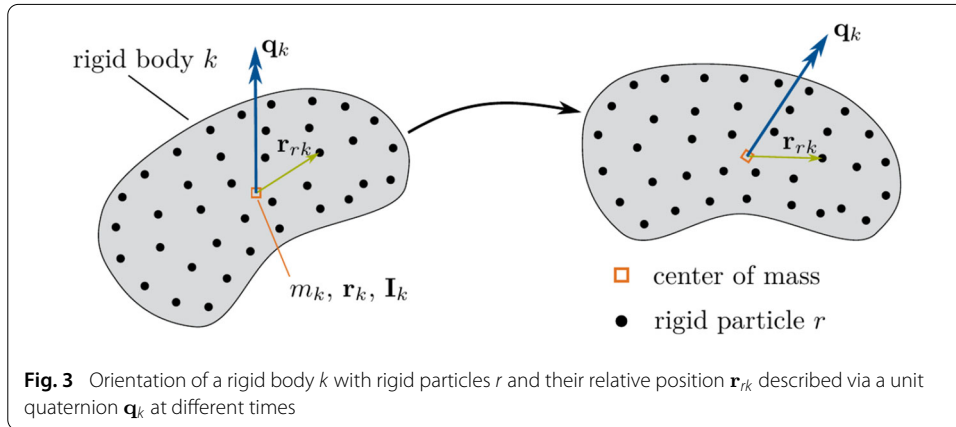
Following a weakly compressible approach, the density ρ_i and pressure p_i of a particle i are linked via the equation of state

$$p_i(\rho_i) = c^2(\rho_i - \rho_0) = p_0 \left(\frac{\rho_i}{\rho_0} - 1 \right) \quad (18)$$

with reference density ρ_0 , reference pressure $p_0 = \rho_0 c^2$ and artificial speed of sound c . Note that this commonly applied approach can only capture deviations from the reference pressure, i.e., $p_i(\rho_0) = 0$, and not the total pressure. To limit density fluctuations to an acceptable level, while still avoiding too severe time step restrictions, cf. Eq. (41), strategies are discussed in [21] how to choose a reasonable value for the artificial speed of sound c . Accordingly, in this work the artificial speed of sound c is set allowing an average density variation of approximately 1%.

Boundary and coupling conditions

Herein, both rigid wall boundary conditions as well as rigid body coupling conditions, are modeled following [23]. In the former case, at least $q = \text{floor}(r_c/\Delta x)$ layers of boundary particles b are placed parallel to the fluid boundary Γ_D^f with a distance of $\Delta x/2$ outside of the fluid domain Ω^f in order to maintain full support of the smoothing kernel. In the latter case, rigid particles r of rigid bodies k are considered, while naturally describing the fluid–solid interface Γ^{fs} . In both cases, a boundary particle b or a rigid particle r contribute to the density summation (14) and to the momentum equation (15) evaluated for a fluid particle i considered as neighboring particle j . The respective quantities of boundary



particles b respectively rigid particles r are extrapolated from the fluid field based on a local force balance as described in [23]. Consequently, striving for conservation of linear momentum, cf. Eq. (17), the force acting on a rigid particle r stemming from interaction with fluid particle i , cf. Eq. (15), is given as

$$\mathbf{f}_{ri} = -m_i \mathbf{a}_{ir}. \tag{19}$$

Remark 10 The floor operator is defined by $\text{floor}(x) := \max \{k \in \mathbb{Z} \mid k \leq x\}$ and returns the largest integer that is less than or equal to its argument x .

Modeling the motion of rigid bodies discretized by particles

Within this formulation, each rigid body k is composed of several rigid particles r that are fixed relative to a rigid body frame, i.e., there is no relative motion among rigid particles of a rigid body. Thus, the rigid particles of a rigid body are not evolved in time individually, but follow the motion of the rigid body described by the balance of linear and angular momentum, cf. Eqs. (6)–(7). As a consequence of the spatial decomposition approach, special communication between all processors hosting rigid particles r of a rigid body k in terms of the evaluation of mass quantities, or resultant forces and torques, is required. For ease of notation, in the following the index $(\cdot)^s$ denoting solid quantities is dropped.

Orientation of rigid bodies

The orientation ψ_k of a rigid body k , described by one respectively three degrees of freedom in two- and three-dimensional space, is previously introduced without explicitly defining a specific parameterization of the underlying rotation, e.g., via Euler angles or Rodriguez parameters. Moreover, as stated in Remark 2, explicit evolution of the orientation ψ_k requires special Lie group time integrators. A straightforward approach to overcome aforementioned issues is to describe the orientation of a rigid body via quaternion algebra, cf. Remark 12. Consequently, in the following it is assumed that at all times the orientation ψ_k of a rigid body k can be uniquely described by a unit quaternion \mathbf{q}_k , cf. Fig. 3. Once a local rigid body frame is defined, this allows to transform the relative position of rigid particles \mathbf{r}_{rk} , cf. Remark 11, from that rigid body frame to the reference frame, e.g., a global cartesian system.

Remark 11 Note that the relative position of rigid particles \mathbf{r}_{rk} expressed in the rigid body frame is, in general, a known (and constant) quantity, that only needs to be updated in case the center of mass position \mathbf{r}_k changes, i.e., due to phase transitions.

Remark 12 For the sake of brevity, the principals of quaternion algebra are not delineated herein. It remains the definition of operator \circ denoting quaternion multiplication as used in the following.

Parallel evaluation of mass-related quantities

In a first step, on each processor p the processor-wise mass ${}_p m_k$ and center of mass position ${}_p \mathbf{r}_k$ of a rigid body k are computed as

$${}_p m_k = \sum_r m_r \quad \text{and} \quad {}_p \mathbf{r}_k = \frac{\sum_r m_r \mathbf{r}_r}{\sum_r m_r} \quad (20)$$

considering the mass m_r and position \mathbf{r}_r of all affiliated rigid particles r being located in the computational domain of processor p , cf. Fig. 4 for an illustration. Accordingly, the processor-wise mass moment of inertia ${}_p \mathbf{I}_k$ of a rigid body k follows componentwise (in index notation) as

$${}_p I_{k,ij} = \sum_r \left[I_r \delta_{ij} + \left[\sum_q ({}_p r_{k,q} - r_{r,q})^2 \delta_{ij} - ({}_p r_{k,i} - r_{r,i})({}_p r_{k,j} - r_{r,j}) \right] m_r \right] \quad (21)$$

with mass m_r and mass moment of inertia I_r of a rigid particle r , cf. Remark 13, and Kronecker delta δ_{ij} , cf. Remark 14. The computed processor-wise quantities, i.e., mass ${}_p m_k$, center of mass position ${}_p \mathbf{r}_k$, and mass moment of inertia ${}_p \mathbf{I}_k$, are communicated to the owning processor of rigid body k . In a second step, on the owning processor the total mass m_k and center of mass position \mathbf{r}_k of rigid body k are computed over all processors p as

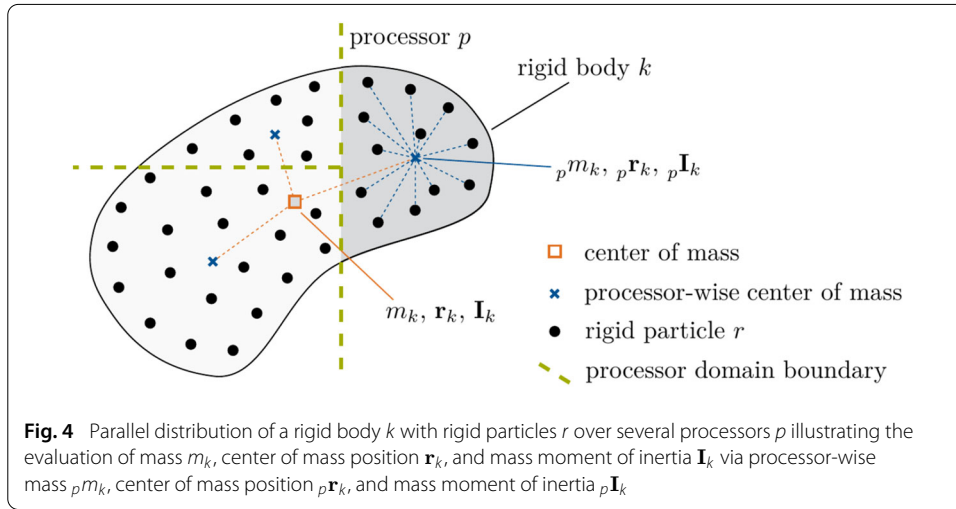
$$m_k = \sum_p {}_p m_k \quad \text{and} \quad \mathbf{r}_k = \frac{\sum_p {}_p m_k {}_p \mathbf{r}_k}{\sum_p {}_p m_k} \quad (22)$$

making use of the received processor-wise quantities. Similar to (21) the mass moment of inertia \mathbf{I}_k of rigid body k follows componentwise (in index notation) as

$$I_{k,ij} = \sum_p \left[{}_p I_{k,ij} + \left[\sum_q (r_{k,q} - {}_p r_{k,q})^2 \delta_{ij} - (r_{k,i} - {}_p r_{k,i})(r_{k,j} - {}_p r_{k,j}) \right] {}_p m_k \right] \quad (23)$$

again considering the received processor-wise quantities. Finally, the determined global quantities, i.e., mass m_k , center of mass position \mathbf{r}_k , and mass moment of inertia \mathbf{I}_k , are communicated from the owning processor to all hosting processors of rigid body k .

Remark 13 The mass moment of inertia I_r of a rigid particle r with mass m_r is computed based on the effective volume $V_{\text{eff}} = (\Delta x)^d$ with initial particle spacing Δx . In two-dimensional space ($d = 2$) assuming circular disk-shaped particles results in $I_r = 0.5 m_r r_{\text{eff}}^2$ with effective radius $r_{\text{eff}} = \Delta x / \sqrt{\pi}$. Accordingly, in three-dimensional space ($d = 3$) assuming spherical-shaped particles results in $I_r = 0.4 m_r r_{\text{eff}}^2$ with effective radius $r_{\text{eff}} = \sqrt[3]{0.75/\pi} \Delta x$.



Remark 14 The Kronecker delta δ_{ij} used in Eqs. (21) and (23) to compute the mass moments of inertia is defined by $\delta_{ij} = \begin{cases} 1 & \text{if } i = j, \\ 0 & \text{otherwise.} \end{cases}$

Remark 15 The computation of the mass moment of inertia, cf. Eqs. (21) respectively (23), is based on the Huygens-Steiner theorem, also called parallel axis theorem.

Parallel evaluation of resultant force and torque

To begin with, the resultant coupling and contact force acting on a rigid particle r of rigid body k is given as

$$\mathbf{f}_r = \sum_i \mathbf{f}_{ri} + \sum_{\hat{k}} \sum_{\hat{r}} \mathbf{f}_{r\hat{r}} \tag{24}$$

with coupling forces \mathbf{f}_{ri} stemming from interaction with neighboring fluid particles i , cf. Eq. (19), and contact forces $\mathbf{f}_{r\hat{r}}$ stemming from interaction with rigid particles \hat{r} of contacting rigid bodies \hat{k} , cf. Eq. (27). Similar to the computation of mass-related quantities as described previously, the resultant force \mathbf{f}_k and torque \mathbf{m}_k acting on a rigid body k are determined considering the parallel distribution of the affiliated rigid particles r on hosting processors p , cf. Fig. 4. Thus, in a first step the processor-wise resultant force ${}_p \mathbf{f}_k$ and torque ${}_p \mathbf{m}_k$ acting on rigid body k are computed as

$${}_p \mathbf{f}_k = \sum_r \mathbf{f}_r \quad \text{and} \quad {}_p \mathbf{m}_k = \sum_r \mathbf{r}_{rk} \times \mathbf{f}_r \tag{25}$$

with $\mathbf{r}_{rk} = \mathbf{r}_r - \mathbf{r}_k$ while considering the resultant forces \mathbf{f}_r acting on all rigid particles r being located in the computational domain of processor p . For correct computation of the processor-wise resultant torque ${}_p \mathbf{m}_k$ the knowledge of the global center of mass position \mathbf{r}_k is required on all processors. Finally, the computed processor-wise forces ${}_p \mathbf{f}_k$ and torques ${}_p \mathbf{m}_k$ are communicated to the owning processor of rigid body k and summed up to the global resultant force and torque acting on rigid body k

$$\mathbf{f}_k = \sum_p {}_p \mathbf{f}_k \quad \text{and} \quad \mathbf{m}_k = \sum_p {}_p \mathbf{m}_k. \tag{26}$$

Remark 16 In the case of a computation on a single processor, the evaluation of mass m_k , center of mass position \mathbf{r}_k , and mass moment of inertia \mathbf{I}_k of a rigid body k follow directly from Eqs. (20) and (21), while the resultant force \mathbf{f}_k and torque \mathbf{m}_k directly follow from Eq. (25), in each case without the need for special communication.

Contact evaluation between neighboring rigid bodies

For the modeling of frictionless contact between neighboring rigid bodies k and \hat{k} , a contact normal force law based on a spring-dashpot model, similar to [29], is employed. The contact force is acting between pairs of neighboring rigid particles r and \hat{r} of contacting rigid bodies, i.e., for distances $r_{r\hat{r}} < \Delta x$ with $r_{r\hat{r}} = |\mathbf{r}_{r\hat{r}}| = |\mathbf{r}_r - \mathbf{r}_{\hat{r}}|$. Accordingly, the contact force acting on a particle r of rigid body k due to contact with a particle \hat{r} of neighboring rigid body \hat{k} is given as

$$\mathbf{f}_{r\hat{r}} = \begin{cases} -\left[\min\left(0, k_c(r_{r\hat{r}} - \Delta x) + d_c(\mathbf{e}_{r\hat{r}} \cdot \mathbf{u}_{r\hat{r}})\right) \right] \mathbf{e}_{r\hat{r}} & \text{if } r_{r\hat{r}} < \Delta x, \\ 0 & \text{otherwise,} \end{cases} \quad (27)$$

with unit vector $\mathbf{e}_{r\hat{r}} = \mathbf{r}_{r\hat{r}}/r_{r\hat{r}}$, stiffness constant k_c , and damping constant d_c . The min operator in Eq. (27) ensures that only repulsive forces between the rigid particles are considered, also known as tension cut-off.

Remark 17 Contact between a rigid body k and a rigid wall is modeled similar to Eq. (27) considering rigid particles r of a rigid body k and boundary particles b of a discretized rigid wall.

Remark 18 The applied contact evaluation between rigid bodies is for simplicity based on a contact normal force law evaluated between rigid particles while neglecting frictional effects. Generally, following a macroscopic approach of contact mechanics with non-penetration constraint, the normal distance between the contacting bodies, typically determined via closest point projections, is the contact-relevant kinematic quantity. Accordingly, the concept applied in this work, can be interpreted as a microscale approach based on a repulsive/steric interaction potential [51] defined between pairs of rigid particles of contacting rigid bodies. In the current work, this approach has been chosen for reasons of simplicity and numerical robustness. An extension to a macroscale approach, i.e., a normal distance-based contact interaction [12, 52, 53], is possible in a straightforward manner. In addition, also a momentum-based energy tracking method [54] was recently applied for collision modeling of fully resolved rigid bodies [55, 56].

Discretization of the heat equation using SPH

Thermal conduction in the combined fluid and solid domain governed by the heat equation (8) is discretized using smoothed particle hydrodynamics following a formulation proposed by Cleary and Monaghan [57]

$$c_{p,a} \frac{dT_a}{dt} = \frac{1}{\rho_a} \sum_b V_b \frac{4\kappa_a\kappa_b}{\kappa_a + \kappa_b} \frac{T_{ab}}{r_{ab}} \frac{\partial W}{\partial r_{ab}} \quad (28)$$

with volume $V_b = m_b/\rho_b$ of particle b and temperature difference $T_{ab} = T_a - T_b$ between particle a and particle b . The discretization of the conductive term is especially suited for

problems involving a different thermal conductivity among the fields [57]. In the equation above, the index $(\cdot)^\phi$ with $\phi \in \{f, s\}$ for fluid and solid field is dropped for ease of notation. Accordingly, the particles a and b may denote fluid particles i as well as rigid particles r , respectively.

Modeling thermally driven reversible phase transitions

Due to the Lagrangian nature of SPH, each (material) particle carries its phase information. This allows for direct evaluation of the discretized heat equation (28) for fluid and rigid particles with corresponding phase-specific parameters of the particle a itself and of neighboring particles b . Phase transitions in the form of melting of a rigid body occurs, in case the temperature T_r of a rigid particle r exceeds the transition temperature T_t . The former rigid particle r changes phase to become a fluid particle i . Conversely, phase transitions in form of solidification occurs, in case the temperature T_i of a fluid particle i falls below the transition temperature T_t and the former fluid particle i becomes a rigid particle r .

Consequently, each time a rigid body k is subject to phase transition, its mass m_k , center of mass position \mathbf{r}_k , and mass moment of inertia \mathbf{I}_k are updated. In addition, the velocity \mathbf{u}_k after phase transition is determined based on quantities prior to phase transition indicated by index $(\cdot)'$ as

$$\mathbf{u}_k = \mathbf{u}'_k + \boldsymbol{\omega}_k \times (\mathbf{r}_{rk} - \mathbf{r}'_{rk}) \quad (29)$$

following rigid body motion with (unchanged) angular velocity $\boldsymbol{\omega}_k$.

Time integration following a velocity-Verlet scheme

The discretized fluid and solid field are both integrated in time applying an explicit velocity-Verlet time integration scheme in kick-drift-kick form, also denoted as leapfrog scheme, that is of second order accuracy and reversible in time when dissipative effects are absent [36]. Again, for ease of notation, in the following the indices $(\cdot)^f$ and $(\cdot)^s$ denoting fluid respectively solid quantities are dropped. Altogether, for the fluid field the positions \mathbf{r}_i of fluid particles i are evolved in time, while for the solid field the center of mass positions \mathbf{r}_k and the orientations $\boldsymbol{\psi}_k$ of all rigid bodies k are evolved in time. However, the positions \mathbf{r}_r of rigid particles r are not evolved in time but directly follow the motion of corresponding affiliated rigid bodies k .

In a first kick-step, the accelerations $\mathbf{a}_i^n = (d\mathbf{u}_i/dt)^n$, as determined in the previous time step n , are used to compute the intermediate velocities

$$\mathbf{u}_i^{n+1/2} = \mathbf{u}_i^n + \frac{\Delta t}{2} \mathbf{a}_i^n \quad (30)$$

of fluid particles i , where Δt is the time step size. Similar, for rigid bodies k the linear and angular accelerations $\mathbf{a}_k^n = (d^2\mathbf{r}_k/dt^2)^n$ respectively $\boldsymbol{\alpha}_k^n = (d\boldsymbol{\omega}_k/dt)^n$ are used to compute the intermediate linear and angular velocities

$$\mathbf{u}_k^{n+1/2} = \mathbf{u}_k^n + \frac{\Delta t}{2} \mathbf{a}_k^n \quad \text{and} \quad \boldsymbol{\omega}_k^{n+1/2} = \boldsymbol{\omega}_k^n + \frac{\Delta t}{2} \boldsymbol{\alpha}_k^n. \quad (31)$$

In a drift-step, the positions (and orientations) of fluid particles i and rigid bodies k are updated to time step $n + 1$ using the intermediate velocities. Accordingly, the positions

of fluid particles i follow as

$$\mathbf{r}_i^{n+1} = \mathbf{r}_i^n + \Delta t \mathbf{u}_i^{n+1/2} \quad (32)$$

and the center of mass positions of rigid bodies k as

$$\mathbf{r}_k^{n+1} = \mathbf{r}_k^n + \Delta t \mathbf{u}_k^{n+1/2}. \quad (33)$$

The orientations of rigid bodies k are updated making use of quaternion algebra. First, the angular orientation increments from time step n to time step $n + 1$ are determined using the intermediate angular velocities of rigid bodies k following

$$\phi_k^{n,n+1} = \Delta t \omega_k^{n+1/2}. \quad (34)$$

Next, the angular orientation increments are described by so-called transition quaternions $\mathbf{q}_k^{n,n+1}$. Finally, quaternion multiplication, cf. Remark 12, gives the updated orientations of rigid bodies k at time step $n + 1$

$$\mathbf{q}_k^{n+1} = \mathbf{q}_k^{n,n+1} \circ \mathbf{q}_k^n. \quad (35)$$

Once the updated orientations (and thus also the updated rigid body frames) are known, the relative positions of rigid particles \mathbf{r}_{rk}^{n+1} can be transformed from the rigid body frame to the reference frame. The velocities and the positions of rigid particles r are updated, considering the underlying rigid body motion of the corresponding rigid bodies k , in consistency with the applied time integration scheme following

$$\mathbf{u}_r^{n+1/2} = \mathbf{u}_k^{n+1/2} + \omega_k^{n+1/2} \times \mathbf{r}_{rk}^{n+1} \quad \text{and} \quad \mathbf{r}_r^{n+1} = \mathbf{r}_k^{n+1} + \mathbf{r}_{rk}^{n+1}. \quad (36)$$

Using the positions \mathbf{r}_a^{n+1} and the intermediate velocities $\mathbf{u}_a^{n+1/2}$ of fluid and rigid particles $a \in \{i, r\}$, the densities ρ_i^{n+1} of fluid particles i are computed via Eq. (14). The densities ρ_r of rigid particles r are not evolved and remain constant. The temperature rates $(dT_a/dt)^{n+1}$ of fluid and rigid particles a are then updated on the basis of Eq. (28) with the temperatures T_a^n as well as the positions \mathbf{r}_a^{n+1} and densities ρ_a^{n+1} . Finally, the temperatures of fluid and rigid particles a are computed as

$$T_a^{n+1} = T_a^n + \Delta t \left(\frac{dT_a}{dt} \right)^{n+1}. \quad (37)$$

The accelerations \mathbf{a}_i^{n+1} of fluid particles i , cf. Eq. (15), and the forces \mathbf{f}_r^{n+1} acting on rigid particles r , cf. Eq. (24), are concurrently computed using the positions \mathbf{r}_a^{n+1} , the intermediate velocities $\mathbf{u}_a^{n+1/2}$, and the densities ρ_a^{n+1} of fluid and rigid particles a . Consequently, the resultant forces \mathbf{f}_k^{n+1} and torques \mathbf{m}_k^{n+1} acting on rigid bodies k together with mass-related quantities give the linear and angular accelerations \mathbf{a}_k^{n+1} respectively $\boldsymbol{\alpha}_k^{n+1}$, cf. Eqs. (6) and (7). In a final kick-step, the velocities of fluid particles i at time step $n + 1$ are computed as

$$\mathbf{u}_i^{n+1} = \mathbf{u}_i^{n+1/2} + \frac{\Delta t}{2} \mathbf{a}_i^{n+1}, \quad (38)$$

while the linear and angular velocities of rigid bodies k are

$$\mathbf{u}_k^{n+1} = \mathbf{u}_k^{n+1/2} + \frac{\Delta t}{2} \mathbf{a}_k^{n+1} \quad \text{and} \quad \boldsymbol{\omega}_k^{n+1} = \boldsymbol{\omega}_k^{n+1/2} + \frac{\Delta t}{2} \boldsymbol{\alpha}_k^{n+1}. \quad (39)$$

Accordingly, the velocities of rigid particles r are determined following the motion of the corresponding rigid bodies k to

$$\mathbf{u}_r^{n+1} = \mathbf{u}_k^{n+1} + \boldsymbol{\omega}_k^{n+1} \times \mathbf{r}_{rk}^{n+1}. \quad (40)$$

To maintain stability of the time integration scheme, the time step size Δt is restricted by the Courant–Friedrichs–Lewy (CFL) condition, the viscous condition, the body force condition, the contact condition, and the conductivity condition, refer to [21,50,58,59] for more details,

$$\Delta t \leq \min \left\{ 0.25 \frac{h}{c + |\mathbf{u}_{max}|}, 0.125 \frac{h^2}{\nu}, 0.25 \sqrt{\frac{h}{|\mathbf{b}_{max}|}}, 0.22 \sqrt{\frac{m_r}{k_c}}, 0.1 \frac{\rho c_p h^2}{\kappa} \right\}, \quad (41)$$

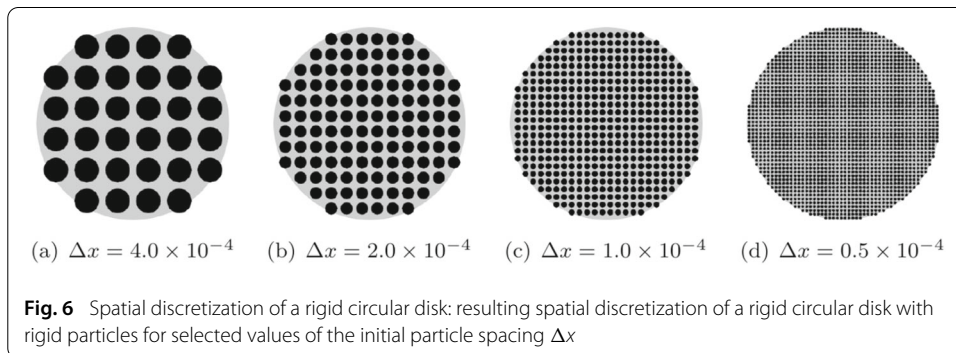
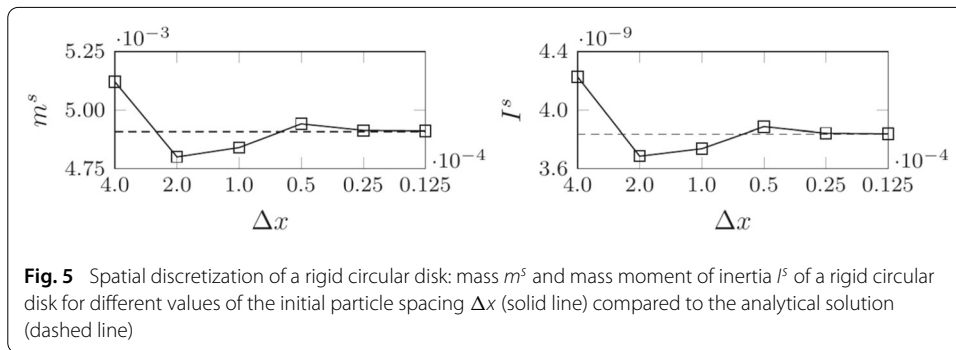
with maximum fluid velocity \mathbf{u}_{max} and maximum body force \mathbf{b}_{max} .

Numerical examples

The purpose of this section is to investigate the proposed numerical formulation for solving fluid–solid and contact interaction problems examining several numerical examples in two and three dimensions involving multiple mobile rigid bodies, two-phase flow, and reversible phase transitions. To begin with, several numerical examples of a single rigid body in a fluid flow, considering different spatial discretizations, are studied and compared to reference solutions. In a next step, two examples close to potential application scenarios of the proposed formulation in the fields of engineering and biomechanics are investigated. Finally, the capabilities of the proposed parallel computational framework are demonstrated performing a strong scaling analysis. The parameter values in the numerical examples, unless indicated otherwise, are given in a consistent set of units and presented in non-dimensional form.

Spatial discretization of a rigid circular disk

In the following, a rigid circular disk of diameter $D = 2.5 \times 10^{-3}$ with density $\rho^s = 1.0 \times 10^3$, motivated by two subsequent examples, is discretized with different values of the initial particle spacing Δx . The mass m^s and the mass moment of inertia I^s (with respect to the axis of symmetry) of the circular disk are computed with the proposed formulation and shown in Fig. 5. With decreasing initial particle spacing Δx the values for mass m^s and mass moment of inertia I^s converge to the analytical solution confirming the proposed formulation. To illustrate, the resulting spatial discretizations of the circular disk with rigid particles are shown in Fig. 6. Clearly, the approximation of the circular shape of the disk is of better accuracy for decreasing initial particle spacing Δx . To keep the computational effort at a feasible level, in the two subsequent examples the domain is discretized with an initial particle spacing of $\Delta x = 2.0 \times 10^{-4}$ and $\Delta x = 1.0 \times 10^{-4}$.



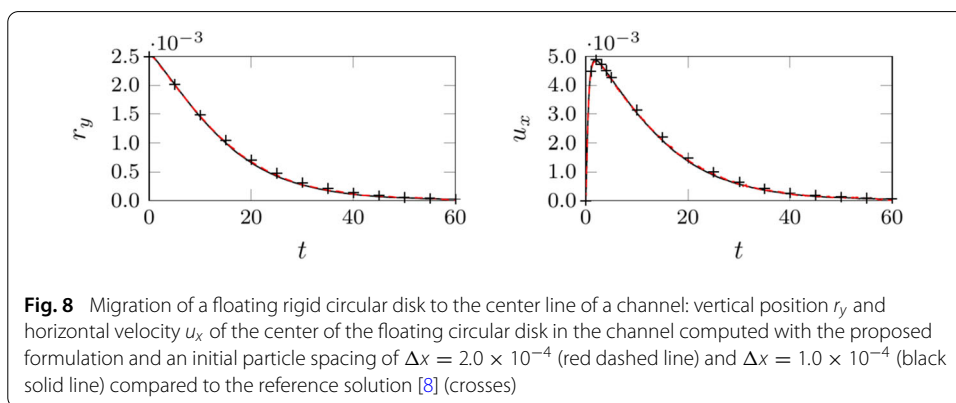
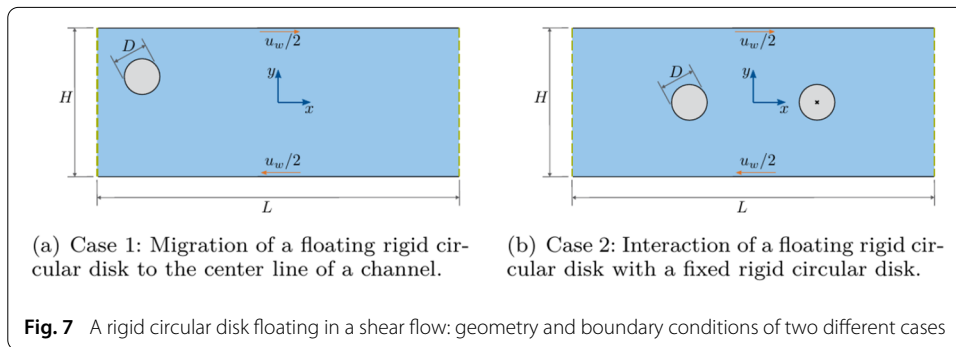
A rigid circular disk floating in a shear flow

The following numerical examples are concerned with the motion of a rigid circular disk floating in a shear flow. First, the principal setup of the problem along with numerical parameters is described, thereafter, two distinct cases are considered in detail. For validation, the results obtained with the proposed formulation are compared to [8] also applying SPH to discretize the fluid and the solid field.

A rigid circular disk of diameter $D = 2.5 \times 10^{-3}$ with density $\rho^s = 1.0 \times 10^3$ is allowed to move freely in a rectangular channel of length $L = 5.0 \times 10^{-2}$ and height $H = 1.0 \times 10^{-2}$, cf. Fig. 7. The remainder of the channel is occupied by a Newtonian fluid with density $\rho^f = 1.0 \times 10^3$ and kinematic viscosity $\nu^f = 5.0 \times 10^{-6}$. The bottom and top channel walls move with velocity $u_w/2$ in opposite direction inducing a shear flow in the channel. The Reynolds number of the problem is given as $Re = u_w D^2 / 4\nu^f H$ [8,60] taking into account the diameter of the circular disk D and the channel height H . At the left and right end of the channel, periodic boundary conditions are applied, cf. Remark 19.

For the fluid phase, an artificial speed of sound $c = 0.25$ is chosen, resulting in a reference pressure $p_0 = 62.5$ of the weakly compressible model. The background pressure p_b of the transport velocity formulation is set equal to the reference pressure p_0 . The motion of the bottom and top channel walls is modeled using moving boundary particles. The problem is solved for different values of the initial particle spacing Δx for times $t \in [0, 60.0]$ with time step size Δt obeying respective conditions (41).

Remark 19 Imposing a periodic boundary condition in a specific spatial direction allows for particle interaction evaluation across opposite domain borders. Moreover, particles leaving the domain on one side are re-entering on the opposite side.



Case 1: Migration of a floating rigid circular disk to the center line of a channel

This case is based on studies [60,61] stating that a rigid circular disk floating in a shear flow in a channel migrates to the center line of the channel independent of its initial position and initial velocity. Herein, the rigid circular disk is initially at rest placed at vertical position $r_y = 2.5 \times 10^{-3}$ in the channel, cf. Fig. 7. The channel walls move in opposite direction with a velocity magnitude of $u_w/2 = 0.01$ resulting in the Reynolds number $Re = 0.625$ of the problem.

The obtained vertical position r_y and the horizontal velocity u_x of the center of the circular disk in the channel over time t are displayed in Fig. 8 for two different values of the initial particle spacing Δx . The circular disk migrates to the center line of the channel as expected, showing no significant difference between the results obtained with different initial particle spacings Δx . In addition, a comparison to the results of [8] shows very good agreement for the dynamics of the solution.

Case 2: Interaction of a floating rigid circular disk with a fixed rigid circular disk

In the presence of a rigid circular disk that is fixed at the center line of the channel, a rigid circular disk floating in a shear flow migrates to a specific position of equilibrium independent of its initial position and velocity as stated in [62]. Herein, the fixed and the floating rigid circular disks are initially placed on the center line of the channel at horizontal position $r_x = \pm 3.75 \times 10^{-3}$, cf. Fig. 7. The channel walls move in opposite direction with a velocity magnitude of $u_w/2 = 0.012$ resulting in the Reynolds number $Re = 0.75$ of the problem.

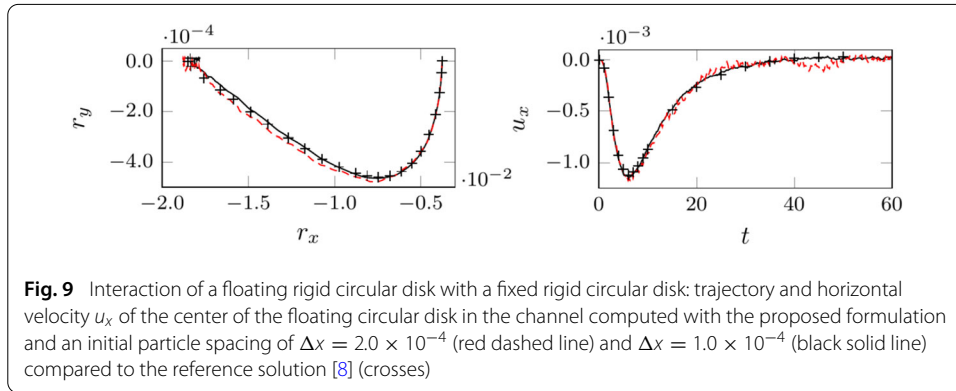


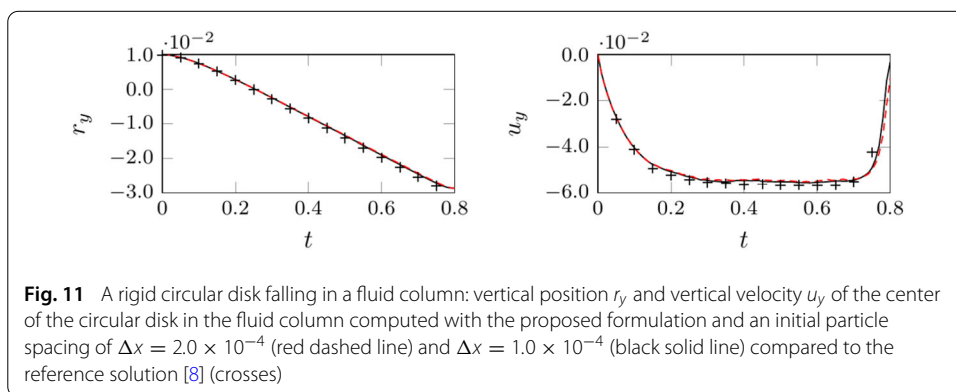
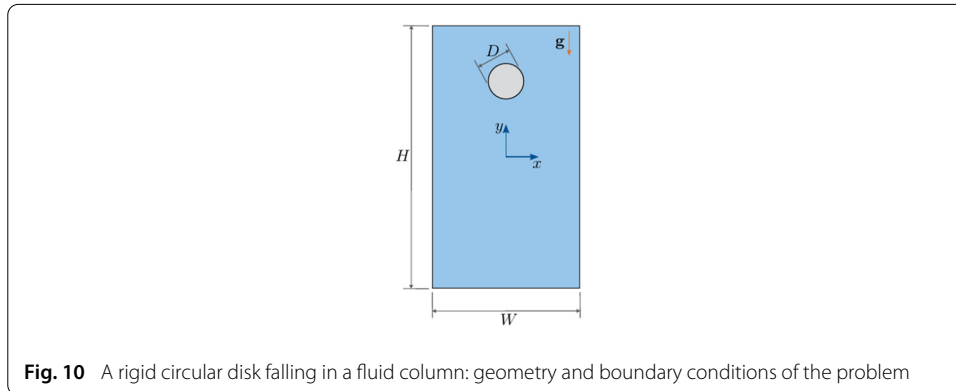
Figure 9 shows the obtained trajectory, i.e., vertical position r_y over horizontal position r_x , and horizontal velocity u_x of the center of the floating circular disk in the channel for two different values of the initial particle spacing Δx . The results obtained with initial particle spacing $\Delta x = 1.0 \times 10^{-4}$ are in good agreement to the reference solution [8]. However, the results obtained with initial particle spacing $\Delta x = 2.0 \times 10^{-4}$ show fluctuations of the horizontal velocity u_x , which is why also the trajectory deviates from the reference solution [8]. This can be explained with disturbances of the density field due to relative particle movement [21], that are more pronounced with a coarser spatial discretization, i.e., with larger initial particle spacing Δx .

A rigid circular disk falling in a fluid column

A rigid circular disk of diameter $D = 2.5 \times 10^{-3}$ with density $\rho^s = 1.25 \times 10^3$ is initially at rest placed on the y -axis at vertical position $r_y = 1.0 \times 10^{-2}$ in a closed rectangular box of height $H = 6.0 \times 10^{-2}$ and width $W = 2.0 \times 10^{-2}$, cf. Fig. 10. The remainder of the box is occupied by a Newtonian fluid with density $\rho^f = 1.0 \times 10^3$ and kinematic viscosity $\nu^f = 1.0 \times 10^{-5}$. A gravitational acceleration of magnitude $|\mathbf{g}| = 9.81$ shall act on both the fluid and solid field in negative y -direction. Following [8] this is modeled considering the buoyancy effect, i.e., body force $\mathbf{b}^s = (\rho^s - \rho^f)/\rho^s \mathbf{g}$ is acting on the solid field while no body force $\mathbf{b}^f = 0.0$ is applied on the fluid field (each per unit mass). It is worth noting that, naturally, it would also be possible to directly set the gravitational acceleration for the fluid and solid field. For validation, the results obtained with the proposed formulation are compared to [8] also applying SPH to discretize the fluid and the solid field.

For the fluid phase, an artificial speed of sound $c = 0.5$ is chosen, resulting in a reference pressure $p_0 = 250.0$ of the weakly compressible model. The background pressure p_b of the transport velocity formulation is set equal to the reference pressure p_0 . The stiffness and damping constant applied for contact evaluation are set to $k_c = 1.0 \times 10^8$ and $d_c = 1.0 \times 10^2$. The walls of the box are modeled using boundary particles. The problem is solved for different values of the initial particle spacing Δx for times $t \in [0, 0.8]$ with time step size Δt obeying respective conditions (41).

The obtained vertical velocity and horizontal position of the center of the circular disk in the box over time t are displayed in Fig. 11 for two different values of the initial particle spacing Δx compared to the reference solution [8]. The results obtained with different initial particle spacing Δx show only minor differences. The terminal velocity of the rigid



circular disk is slightly smaller than given in the reference solution [8]. It shall be noted that, in contrast to [8], contact of the rigid circular disk and the wall of the box is explicitly considered. Consequently, the rigid circular disk comes at rest when approaching the bottom wall of the box.

Melting and solidification of powder grains in a melt pool

In metal powder bed fusion additive manufacturing (PBFAM), structural components are created utilizing a laser or electron beam to melt and fuse metal powder, layer per layer, to form the final part. PBFAM has the potential to enable new paradigms of product design, manufacturing and supply chains. However, due to the complexity of PBFAM processes, the interplay of process parameters is not completely understood, creating the need for further research, amongst others in the field of computational melt pool modeling [15,16]. For this purpose, an SPH formulation for thermo-capillary phase transition problems with a focus on metal PBFAM melt pool modeling has recently been proposed [18]. For simplicity, this and other state-of-the-art approaches [18–20] in the field consider powder grains that are spatially fixed. In the real physical process, however, it is observed that, depending on the processing conditions, melt evaporation and thereby induced vapor and gas flows in the build chamber may result in powder grains entrainment and ejection, i.e., a considerable degree of material re-distribution during the melting process. On the one hand, this effect considerably affects process stability and mechanisms of defect creation, on the other hand, it can not be represented by state-of-the-art approaches restricted to immobile powder grains [18–20]. In the following, a two- and a three-dimensional example each with different geometry, boundary conditions, and material parameters

are considered. The purpose of these examples is not to study PBFAM in detail but to showcase the general applicability of the proposed formulation to capture the dynamics of mobile powder grains undergoing temperature-induced phase transitions, i.e., melting and solidification, while being exposed to gravitational acceleration and gas flow. To this end, surface tension and wetting effects as well as the influence of evaporation-induced recoil pressure, as discussed in [18], are neglected. The focus is set on the investigation of highly dynamic motion and interaction of powder grains with each other, the liquid melt phase and a surrounding gas phase, undergoing reversible phase transitions, i.e., melting and solidification.

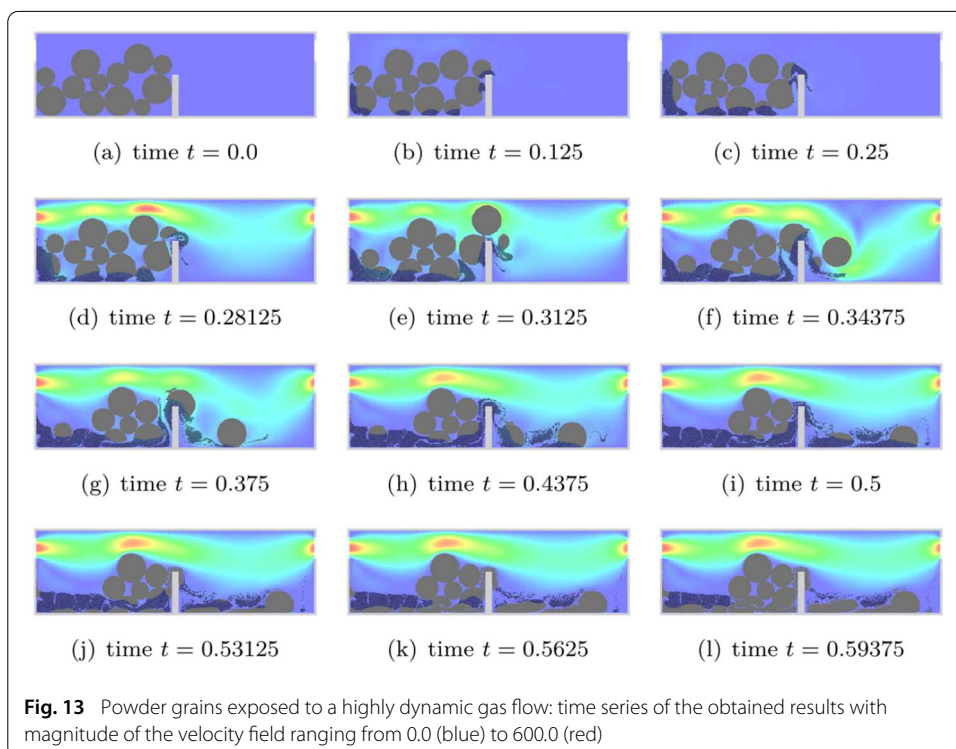
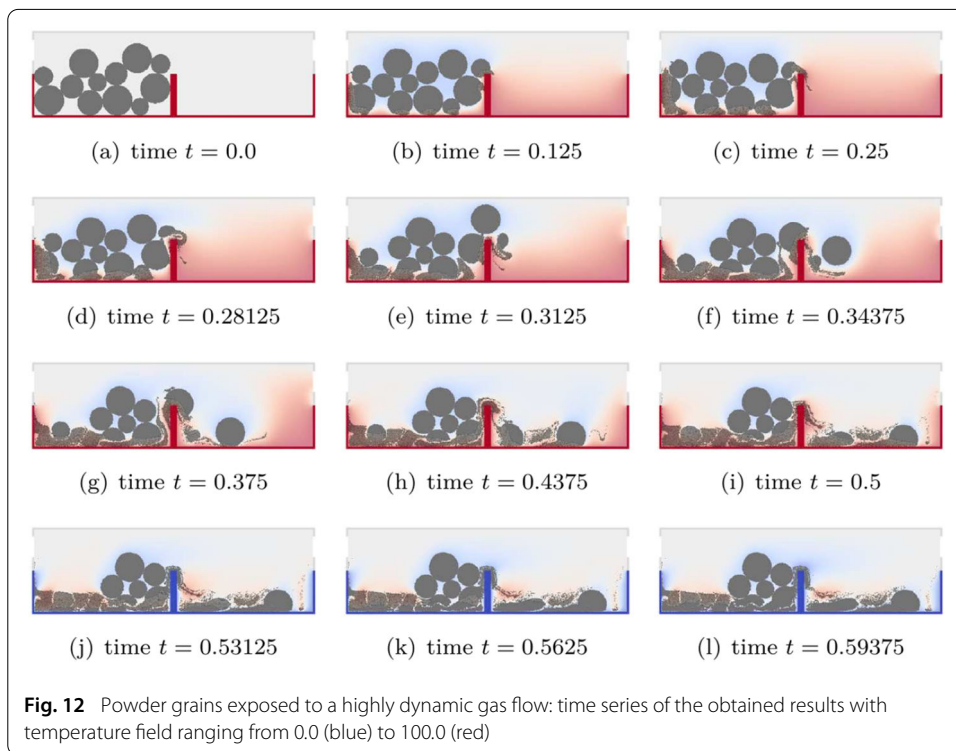
Powder grains exposed to a highly dynamic gas flow

This two-dimensional example is solely intended to demonstrate the model capabilities for this type of application, while keeping the overall example simple in this method-focused contribution. For this reason, non-physical parameter values and boundary conditions are chosen in the following.

A rectangular box is composed of two chambers, each with width 20.0 and height 12.0, that are connected by an opening spanning the upper half of the box. An inlet and outlet of width 3.0 are located at the top left and top right end of the box. Powder grains of a solid metal phase (density $\rho^s = 1.0$, heat capacity $c_p^s = 1.0$, thermal conductivity $\kappa^s = 10.0$) with diameters between 2.5 and 4.4 are placed initially at rest inside the left chamber of the box. The initial positions of the powder grains can, e.g., be obtained in a pre-processing step based on the discrete element method (DEM) and a cohesive powder model [29,63]. The remainder of the box is initially filled with a gas phase (Newtonian fluid, density $\rho^g = 0.1$, kinematic viscosity $\nu^g = 100.0$, heat capacity $c_p^g = 0.01$, thermal conductivity $\kappa^g = 0.1$). The temperature is initialized to $T_0^s = 25.0$ within the solid metal phase and to $T_0^g = 50.0$ within the gas phase. In the upper half of the box walls the temperature is fixed to $\hat{T} = 50.0$ at all times. In the lower half of the box walls the temperature is set to $\hat{T} = 100.0$ until time $t \leq 0.5$, and to $\hat{T} = 0.0$ for time $t > 0.5$. Refer to Figs. 12 and 13 containing an illustration of the initial configuration. Reversible phase transitions between solid metal phase and liquid metal phase (Newtonian fluid, density $\rho^l = 1.0$, kinematic viscosity $\nu^l = 100.0$, heat capacity $c_p^l = 1.0$, thermal conductivity $\kappa^l = 10.0$) is assumed to occur at a transition temperature of $T_t = 50.0$. With the goal to evoke drag forces acting on the powder grains, for times $t > 0.25$ a parabolic inflow respectively outflow of the gas phase with mean velocity 420.0 is prescribed at the inlet and outlet of the box. A gravitational acceleration of magnitude $|\mathbf{g}| = 1.0 \times 10^4$ is acting downwards, set as body force (per unit mass) of all involved phases.

For both fluid phases (liquid metal and gas), the reference pressure of the weakly compressible model is set to $p_0 = 16.0 \times 10^6$, and the background pressure p_b of the transport velocity formulation is set equal to the reference pressure p_0 . The stiffness and damping constant applied for contact evaluation are set to $k_c = 1.0 \times 10^8$ and $d_c = 1.0 \times 10^2$. The wall of the box is modeled using boundary particles. The inflow and outflow conditions are modeled similar as described in [49]. The problem is solved with initial particle spacing $\Delta x = 0.1$ for times $t \in [0, 0.75]$ with a time step size of $\Delta t = 0.625 \times 10^{-5}$.

A time series of illustrations of the obtained results is given in Figs. 12 and 13. The solid metal phase is visualized in gray color. The particles discretizing the liquid metal phase



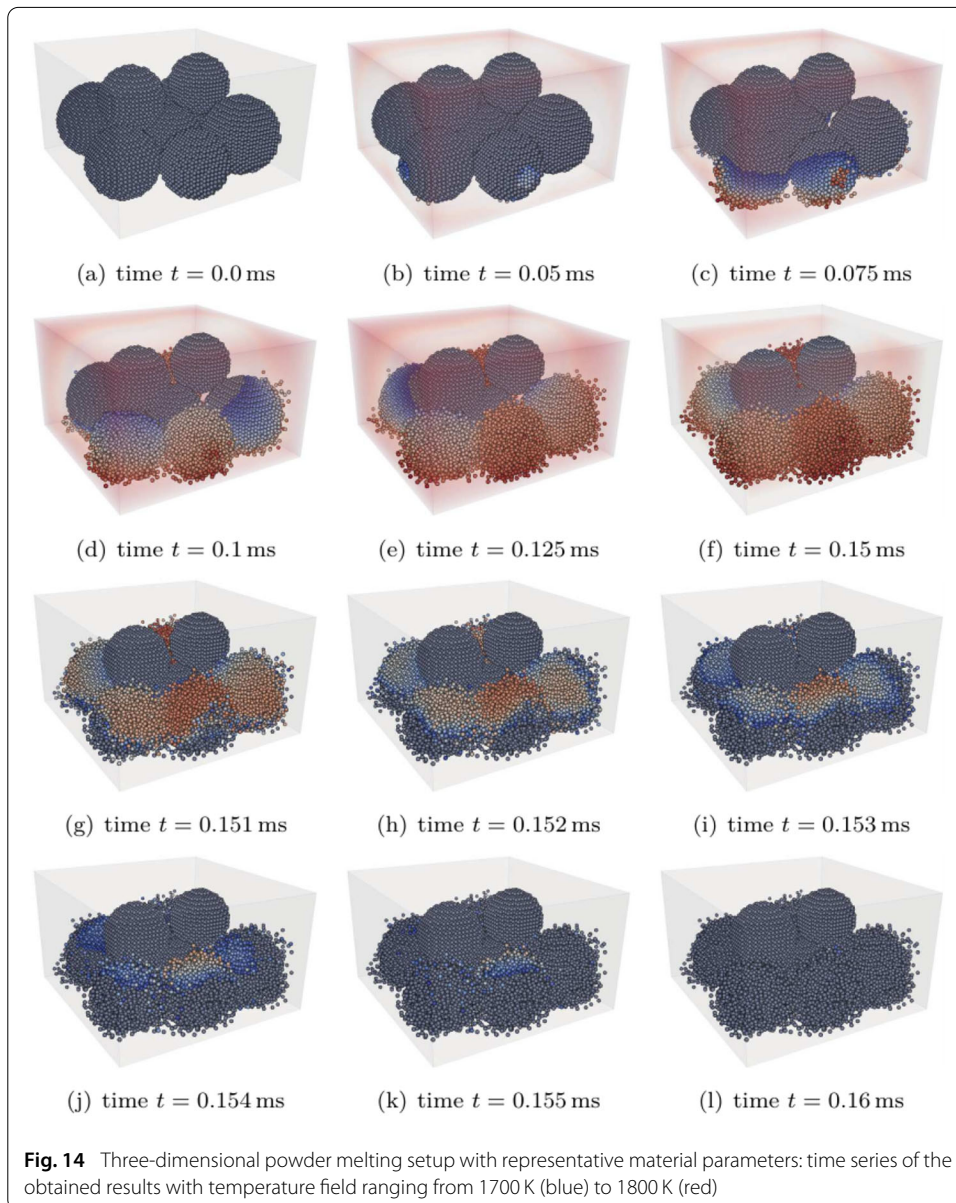
are displayed in black color. In the background, the temperature respectively velocity field of the combined liquid metal and gas phase are displayed. Thereto, both fields were post-processed applying SPH approximation (13) and visualized by a color code. In Fig. 12 additionally the temperature of the walls is shown. First, the powder grains are heated and gradually start melting into liquid metal where in close contact to the hot wall. Eventually, after time $t = 0.25$, powder grains are subjected to the gas flow through the box. Some (partially melted) powder grains are swept into the right chamber of the box, where melting after contact with the hot wall continues. A non-smooth and strongly distorted interface topology between liquid metal and gas phase develops, especially in the right chamber of the box, because surface tension and wetting effects are neglected. Finally, with the temperature in the lower half of the box set to $\hat{T} = 0.0$ after time $t = 0.5$, the liquid metal phase is cooled down drastically and eventually resolidifies.

Three-dimensional powder melting setup with representative material parameters

In this example, the focus is set on a three-dimensional setup while considering representative material parameters for stainless steel and the surrounding gas phase taken from [18] with the purpose to demonstrate the general applicability of the proposed formulation for metal PBFAM melt pool modeling. However, note that some characteristic phenomena relevant for the latter, e.g., surface tension and wetting effects, are still neglected.

Powder grains of a solid metal phase (density $\rho^s = 7430 \text{ kg m}^{-3}$, heat capacity $c_p^s = 965 \text{ J kg}^{-1} \text{ K}^{-1}$, thermal conductivity $\kappa^s = 35.95 \text{ W m}^{-1} \text{ K}^{-1}$) with diameters between $16 \mu\text{m}$ and $20 \mu\text{m}$ are placed initially at rest inside a cuboid box with dimensions of $50 \mu\text{m} \times 50 \mu\text{m} \times 30 \mu\text{m}$. The initial positions of the powder grains can, e.g., be obtained in a pre-processing step based on the discrete element method (DEM) and a cohesive powder model [29, 63]. The remainder of the box is initially filled with a gas phase (Newtonian fluid, density $\rho^g = 74.3 \text{ kg m}^{-3}$, dynamic viscosity $\eta^g = 6.0e - 4 \text{ kg m}^{-1} \text{ s}^{-1}$, heat capacity $c_p^g = 10 \text{ J kg}^{-1} \text{ K}^{-1}$, thermal conductivity $\kappa^g = 2.6 \times 10^{-2} \text{ W m}^{-1} \text{ K}^{-1}$). The temperature is initialized to $T_0^s = 500 \text{ K}$ and $T_0^g = 500 \text{ K}$ within the solid metal phase and the gas phase. In all box walls the temperature is set to $\hat{T} = 1800 \text{ K}$ until time $t \leq 0.15 \text{ ms}$, and to $\hat{T} = 500 \text{ K}$ for time $t > 0.15 \text{ ms}$. Refer to Fig. 14 containing an illustration of the initial configuration. Reversible phase transitions between solid metal phase and liquid metal phase (Newtonian fluid, density $\rho^l = 7430 \text{ kg m}^{-3}$, dynamic viscosity $\eta^l = 6.0 \times 10^{-3} \text{ kg m}^{-1} \text{ s}^{-1}$, heat capacity $c_p^l = 965 \text{ J kg}^{-1} \text{ K}^{-1}$, thermal conductivity $\kappa^l = 35.95 \text{ W m}^{-1} \text{ K}^{-1}$) is assumed to occur at a transition temperature of $T_t = 1700 \text{ K}$. A gravitational acceleration of magnitude $|\mathbf{g}| = 9.81 \text{ ms}^{-2}$ is acting downwards, set as body force (per unit mass) of all involved phases.

For both fluid phases (liquid metal and gas), the reference pressure of the weakly compressible model is set to $p_0 = 1.0 \times 10^7 \text{ N m}^{-2}$ and the background pressure of the transport velocity formulation to $p_b = 5p_0$. The stiffness and damping constant applied for contact evaluation are set to $k_c = 1.0 \text{ kg s}^{-2}$ and $d_c = 1.0 \times \text{kg s}^{-1}$. The wall of the box is modeled using boundary particles. The complete domain is discretized by particles with initial particle spacing $\Delta x = 1.0 \mu\text{m}$ resulting in a total of approximately 1.13×10^5 particles. The problem is solved for times $t \in [0, 0.175] \text{ ms}$ with a time step size of $\Delta t = 5.0 \times 10^{-7} \text{ ms}$.



A time series of illustrations of the obtained results is given in Fig. 14. The particles discretizing the solid metal phase are displayed in gray color. The particles discretizing the liquid metal phase are colored based on the temperature field with transition temperature $T_t = 1700$ K as lower value and temperature of the hot box walls $\hat{T} = 1800$ K as upper value. In the background, the temperature field of the combined liquid metal and gas phase is post-processed applying SPH approximation (13) and visualized by a color code until time $t \leq 0.15$ ms. The powder grains in close contact to the hot box walls are heated and gradually start melting into liquid metal. Under the influence of gravity the (partially melted) powder grains are gradually displacing the liquid metal. A non-smooth and strongly distorted interface topology between the liquid metal and gas phase develops. This can be explained by the fact that surface tension and wetting effects are neglected in this specific example. After time $t = 0.15$ ms the temperature of the box walls is suddenly

set to $\hat{T} = 500$ K. As a consequence, the liquid metal close to the cool box walls rapidly resolidifies.

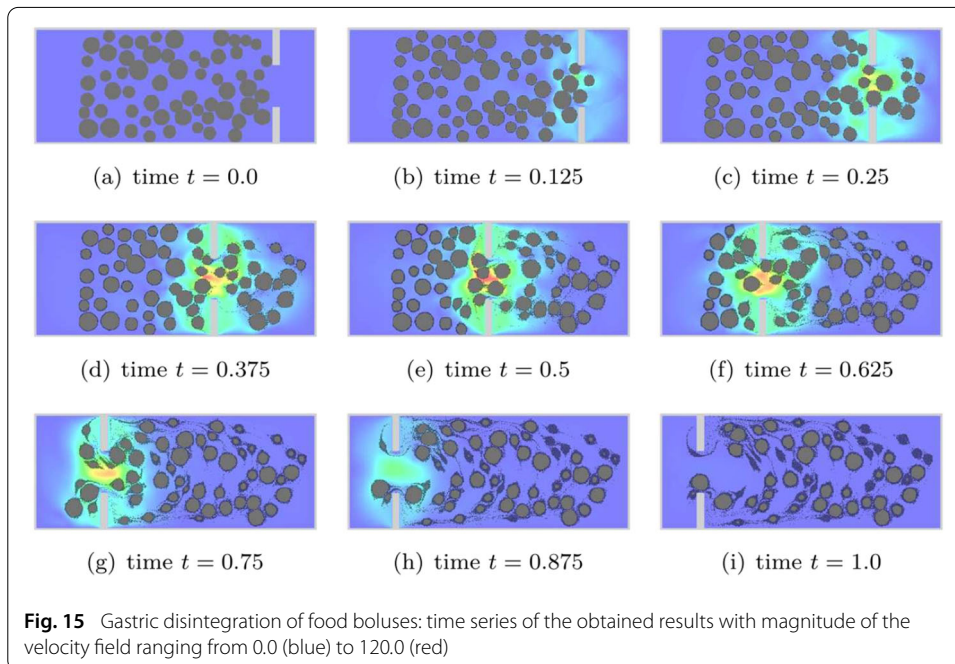
In sum, both examples demonstrates that highly dynamic motion of arbitrarily-shaped powder grains as relevant, e.g., for metal PBFAM melt pool modeling, can be captured along with melting and solidification by the proposed formulation in a robust manner. Consequently, the proposed formulation can be recommended as a useful extension of the SPH formulation for mesoscale melt pool modeling [18], or other current state-of-the-art approaches, e.g., [19,20], allowing for more detailed studies of PBFAM processes.

Gastric disintegration of food boluses

Examination of gastric fluid mechanics plays an important role for modeling digestion of food in the human stomach. The digesta are characterized by a multiphasic nature consisting of fluid (gastric juice and chyme) and solid (food boluses) phases [17]. Intra-gastric fluid motion is driven by the propagation of so-called antral contraction waves (ACWs), i.e., circular constrictions of the gastric wall due to smooth muscle contractions [64]. The ACWs are initiated at the pacemaker region of the stomach and travel along the greater curvature towards the pylorus both mixing and grinding the digesta. Concurrently, absorption of gastric juice fosters chemical and mechanical breakdown of food boluses into chyme [65]. At low viscosity, i.e., following intragastric dilution of the digesta with gastric juice, repulsive jet-like fluid motion between the ACWs can be observed [66–68].

This example aims to demonstrate the capability of the proposed formulation to replicate typical gastric flow patterns including phase transitions. As compared to this complex application scenario, the configuration of the example is kept simple to focus on the principal effects. Consequently, non-physiological parameter values and boundary conditions are applied. Consider a rectangular box of width 40.0 and height 16.0 (coordinate system in the center) with a mobile constriction. A total of 60 food boluses (density $\rho^s = 1.0$, diffusivity $D^s = 0.25$), represented by mobile rigid bodies with diameters between 1.6 and 2.8, are placed at random positions inside the box. The remainder of the box is initially filled with gastric juice (Newtonian fluid, density $\rho^g = 1.0$, kinematic viscosity $\nu^g = 100.0$, diffusivity $D^g = 1.0$). Both the food boluses and the gastric juice are initially at rest. The initial configuration of the example is contained in Fig. 15. Over time, food boluses disintegrate into chyme (Newtonian fluid, density $\rho^c = 1.0$, kinematic viscosity $\nu^c = 200.0$, diffusivity $D^c = 0.25$). Herein, this is modeled considering the transport of a concentration C within the food boluses and chyme, resembling some kind of moisture penetration, by solving a diffusion equation, cf. Remark 4. Accordingly, the concentration within the food boluses is initialized with $C_0 = 0.0$, while the concentration within the gastric juice is fixed to $\hat{C} = 1.0$ at all times. Phase transitions from food boluses to chyme is assumed to occur at a transition concentration of $C_t = 0.8$. The propagation of an ACW is modeled by the movement of the mobile constriction in the box with a time dependent horizontal velocity of $-14.5\pi \sin(\pi t)$ from horizontal position 14.5 to -14.5 , cf. Fig. 15.

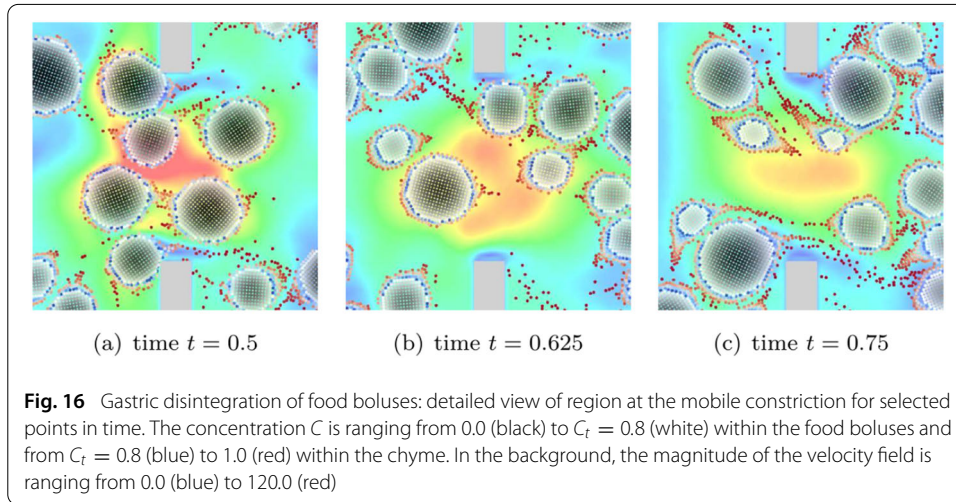
For both fluid phases (gastric juice and chyme), an artificial speed of sound $c = 1.0 \times 10^3$ is chosen, resulting in a reference pressure $p_0 = 1.0 \times 10^6$ of the weakly compressible model, with background pressure of the transport velocity formulation set to $p_b = 5p_0$. The stiffness and damping constant applied for contact evaluation are set to $k_c = 1.0 \times 10^8$



and $d_c = 1.0 \times 10^2$. The wall of the box and the mobile constriction are modeled using (moving) boundary particles. The problem is solved with initial particle spacing $\Delta x = 0.1$ for times $t \in [0, 1.0]$ with a time step size of $\Delta t = 1.25 \times 10^{-5}$.

Figure 15 shows a time series of illustrations of the obtained results. The food boluses are visualized in gray color. The particles discretizing the chyme are displayed in black color. In the background, the velocity field of both gastric juice and chyme is post-processed applying SPH approximation (13) and visualized by a color code. Clearly, the typical repulsive jet-like fluid motion induced by the moving constriction can be observed. As a consequence, the food boluses are entrained with the fluid flow through the opening while coming into contact with each other. At the same time, disintegration of food boluses into chyme gradually takes place. After time $t = 0.875$ some food boluses are completely dissolved. A detailed view of the region at the mobile constriction is given in Fig. 16 for selected points in time. Here, the particles discretizing the food boluses and the chyme are colored based on the concentration field, for distinction, utilizing two different color maps with transition concentration C_t as upper respectively lower value. A progressive mixing of gastric juice and chyme can be observed primarily driven by the fluid motion.

Note that the main purpose of this example is to show the robustness of the proposed formulation in the context of highly dynamic fluid flow and phase transitions, e.g., as occurring in the form of repulsive jet-like fluid motion during digestion of food in the human stomach. For the sake of simplicity, non-physiological parameter values are applied. Amongst others, the time scales of ACW propagation and disintegration of food boluses are in a mismatch. In addition, the employed phenomenological digestion model does not explicitly resolve the influence of chemical and mechanical breakdown taking place in reality. In conclusion, this example demonstrates that typical gastric flow patterns including phase transitions are fully captured in a stable and robust manner.



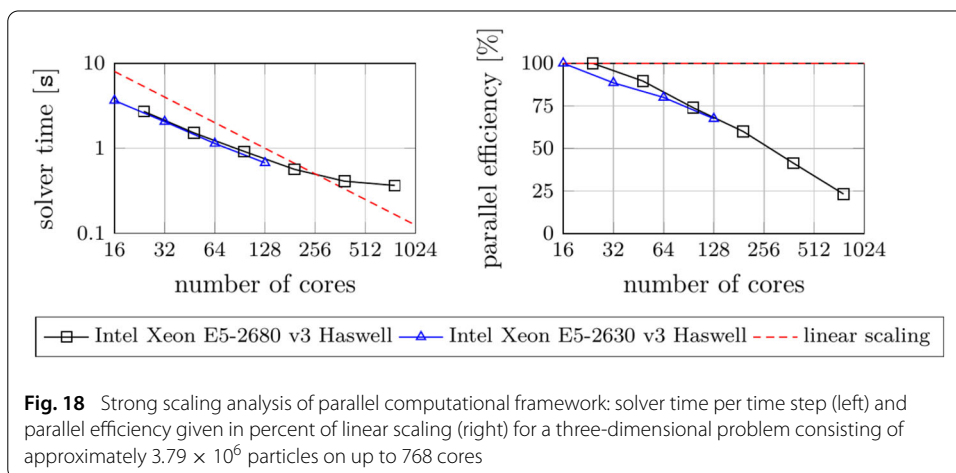
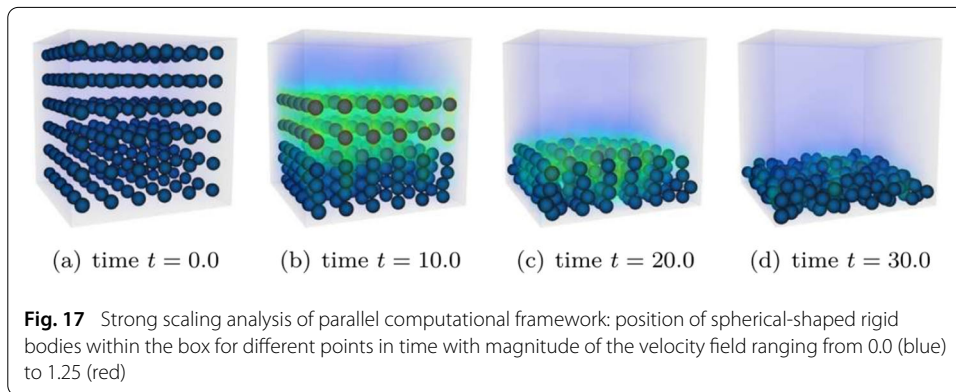
Strong scaling analysis of parallel computational framework

The purpose of this example is to demonstrate the capability and efficiency of the proposed parallel computational framework in handling systems constituted of a large number of particles. To this end, a three-dimensional example consisting of a total of approximately 3.79×10^6 particles is examined on two different parallel systems. Conclusions are drawn concerning the parallel behavior of the parallel computational framework in three dimensions.

A total of 216 spherical-shaped mobile rigid bodies with diameter $D = 2.5$ and density $\rho^s = 10.0$ are placed on a regular grid in a cubic box of edge length $L = 30.0$. The rigid bodies are initially at rest and not in contact with each other or the walls of the box. The remainder of the box is occupied by a Newtonian fluid initially at rest with density $\rho^f = 1.0$ and kinematic viscosity $\nu^f = 1.0$. A gravitational acceleration of magnitude $|\mathbf{g}| = 1.0$ is acting in downward direction, i.e., the body forces (per unit mass) of fluid and solid field are given to $\mathbf{b}^f = \mathbf{g}$ and $\mathbf{b}^s = \mathbf{g}$.

For the fluid phase, an artificial speed of sound $c = 50.0$ is chosen, resulting in a reference pressure $p_0 = 2.5 \times 10^3$ of the weakly compressible model, with background pressure p_b of the transport velocity formulation set equal to the reference pressure p_0 . The stiffness and damping constant applied for contact evaluation are set to $k_c = 1.0 \times 10^3$ and $d_c = 1.0 \times 10^2$. The wall of the box is modeled using boundary particles. The complete domain is discretized by particles with initial particle spacing $\Delta x = 0.2$ resulting in a total of approximately 3.79×10^6 particles, thereof 3.15×10^6 fluid particles, 2.20×10^5 rigid particles, and 4.21×10^5 boundary particles. Following a spatial decomposition approach, the computational domain is divided into $48 \times 48 \times 48$ cubic cells of edge length 0.65 resulting in approximately 34 particles per cell. The problem is solved for times $t \in [0, 30.0]$ with a time step size of $\Delta t = 1.0 \times 10^{-3}$.

For the purposes of illustration, the spherical-shaped rigid bodies within the box are shown in Fig. 17 for the initial setup at $t = 0.0$ and later points in time. In addition, the velocity field of the surrounding fluid is post-processed applying SPH approximation (13) and visualized by a color code with opacity. The rigid bodies are falling freely in the viscous fluid under gravity due to density ratio $\rho^s / \rho^f = 10.0$ until contact with the bottom wall of the box occurs, as first observed after $t \approx 2.5$, or with neighboring rigid bodies, as first



observed after $t \approx 5.0$. The rigid bodies begin piling up at the bottom wall of the box and are nearly at rest at $t = 30.0$.

To showcase the capability and efficiency of the parallel computational framework, a strong scaling analysis is performed utilizing two different parallel systems: The first one consisting of 32 nodes with 2×12 cores (Intel Xeon E5-2680 v3 Haswell, 2.5 GHz) and the second one consisting of 8 nodes with 2×8 cores (Intel Xeon E5-2630 v3 Haswell, 2.4 GHz). The parallel behavior of the proposed computational framework is given in Fig. 18, illustrating the obtained solver time per time step and the parallel efficiency given in percent of linear scaling. The parallel efficiency is computed as $t_1 / (n \cdot t_n) \cdot 100\%$, where t_1 and t_n are the times to solve the problem on one node respectively n nodes.

The parallel computational framework scales almost linearly on both parallel systems for up to 128 cores respectively 192 cores. In this regime a parallel efficiency of more than 60% can be observed. For larger numbers of cores, the scalability deteriorates and the parallel efficiency drops to under 50%. This can be explained with an increasing communication overhead, cf. Remark 9. Comparable results of a strong scaling analysis for an SPH implementation are given, e.g., in [45] ($r_c / \Delta x = 2.5$) and [69] ($r_c / \Delta x = 2.4$), however, in contrast to this example ($r_c / \Delta x = 3.0$) with a smaller ratio of the support radius r_c and the initial particle spacing Δx , resulting in a lower influence on the communication overhead, cf. Remark 9. As a conclusion one can state that the parallel computational framework is capable of efficiently solving systems constituted of a large number of parti-

cles in three dimensions on multiple cores. Looking at the parallel behavior, the obtained results confirm that the proposed framework meets all requirements necessary for detailed and accordingly computationally expensive studies.

Conclusion

In this work, an approach for fluid–solid and contact interaction problems including thermo-mechanical coupling and reversible phase transitions is presented. All fields are spatially discretized using smoothed particle hydrodynamics (SPH). Being a mesh-free discretization scheme, SPH is, compared to mesh-based methods, especially suitable in the context of continually changing interface topologies and dynamic phase transitions by avoiding additional methodological and computational effort to capture such phenomena. A detailed concept for the parallelization of the computational framework, especially for an efficient evaluation of rigid body motion, is an essential part of this work.

The accuracy and robustness of the proposed formulation are demonstrated by several numerical examples studying a single rigid body in fluid flow. The obtained numerical results are in very good agreement with the literature. Also two complex examples close to potential applications scenarios in the fields of engineering and biomechanics were studied. First, motivated by metal PBFAM melt pool modeling, melting and solidification of powder grains subject to highly dynamic fluid motion was simulated. Second, inspired by multiphysics modeling of the human stomach, gastric disintegration of food boluses is considered. Both examples confirm that highly dynamic motion of arbitrarily-shaped rigid bodies embedded in a complex fluid flow and including reversible phase transitions can be captured by the proposed framework in a stable and robust manner. Finally, the parallel computing abilities of the proposed computational framework were demonstrated by a strong scaling analysis of a three-dimensional example with 3.79×10^6 particles revealing a parallel efficiency of more than 60% on up to 192 cores.

To the best of the authors' knowledge, the proposed parallel computational framework is the first of its kind modeling rigid body motion while simultaneously considering thermal conduction, reversible phase transitions, and multiple (liquid and gas) phases. For the sake of simplicity, some characteristic phenomena for thermo-capillary flow and, especially, for metal PBFAM melt pool modeling are not yet addressed in this work, however, straightforward to include considering the authors' previous work. Besides, the applied contact evaluation between rigid bodies is based on a contact normal force law evaluated between rigid particles while neglecting frictional and adhesive effects. An extension to a more sophisticated contact evaluation is part of ongoing research. In summary, the proposed formulation has the ability to accurately model a host of complex multiphysics problems, and it can thus be expected to become a valuable tool for detailed studies in engineering, e.g., metal additive manufacturing, and biomechanics, e.g., digestion of food in the human stomach.

Acknowledgements

The authors thank Bugrahan Z. Temür for preliminary work on a serial rigid body implementation.

Authors' contributions

SLF and CM contributed to the derivation of model equations and worked out the general concept of the proposed modeling approach. SLF conducted the specific code implementation and the shown numerical simulations. All authors contributed to the discussion of results and prepared the manuscript. All authors read and approved the final manuscript.

Funding

Open Access funding enabled and organized by Projekt DEAL. Funded by the Deutsche Forschungsgemeinschaft (DFG, German Research Foundation) - 350481011, 437616465, and 414180263.

Data Availability Statement

The research code is hosted in a private GitLab repository on servers managed by the Leibniz Rechenzentrum (LRZ) in Garching. The obtained numerical results and digital data are stored on private servers and backed up on servers managed by the Leibniz Rechenzentrum (LRZ) in Garching. The datasets generated and/or analyzed during the current study are available from the corresponding author on reasonable request.

Declarations**Competing interests**

The authors declare that they have no competing interests.

Author details

¹Institute for Computational Mechanics, Technical University of Munich, Boltzmannstraße 15, 85748 Garching, Germany,

²Institute for Continuum and Material Mechanics, Hamburg University of Technology, Eißendorfer Straße 42, 21073

Hamburg, Germany, ³Institute of Material Systems Modeling, Helmholtz-Zentrum Hereon, Max-Planck-Straße 1, 21502 Geesthacht, Germany.

Received: 15 March 2021 Accepted: 2 June 2021

Published online: 28 June 2021

References

1. Idelsohn SR, Oñate E, Del Pin F. A Lagrangian meshless finite element method applied to fluid-structure interaction problems. *Computers & Structures*. 2003;81(8–11):655–71.
2. Idelsohn SR, Oñate E, Del Pin F, Calvo N. Fluid-structure interaction using the particle finite element method. *Computer Methods in Applied Mechanics and Engineering*. 2006;195(17–18):2100–23.
3. Oñate E, Idelsohn SR, Celigueta MA, Rossi R. Advances in the particle finite element method for the analysis of fluid-multibody interaction and bed erosion in free surface flows. *Computer Methods in Applied Mechanics and Engineering*. 2008;197(19–20):1777–800.
4. Qiu Lc Wu, Cy. A hybrid DEM/CFD approach for solid-liquid flows. *Journal of Hydrodynamics, Ser B*. 2014;26(1):19–25.
5. Sun X, Sakai M. Three-dimensional simulation of gas-solid-liquid flows using the DEM-VOF method. *Chemical Engineering Science*. 2015;134:531–48.
6. Vångö M, Pirker S, Lichtenegger T. Unresolved CFD-DEM modeling of multiphase flow in densely packed particle beds. *Applied Mathematical Modelling*. 2018;56:501–16.
7. Peng C, Zhan L, Wu W, Zhang B. A fully resolved SPH-DEM method for heterogeneous suspensions with arbitrary particle shape. *Powder Technology*. 2021.
8. Hashemi M, Fatehi R, Manzari M. A modified SPH method for simulating motion of rigid bodies in Newtonian fluid flows. *International Journal of Non-Linear Mechanics*. 2012;47(6):626–38.
9. Bouscasse B, Colagrossi A, Marrone S, Antuono M. Nonlinear water wave interaction with floating bodies in SPH. *Journal of Fluids and Structures*. 2013;42:112–29.
10. Bian X, Litvinov S, Ellero M, Wagner NJ. Hydrodynamic shear thickening of particulate suspension under confinement. *Journal of Non-Newtonian Fluid Mechanics*. 2014;213:39–49.
11. Polfer P, Kraft T, Bierwisch C. Suspension modeling using smoothed particle hydrodynamics: Accuracy of the viscosity formulation and the suspended body dynamics. *Applied Mathematical Modelling*. 2016;40(4):2606–18.
12. Dong X, Li Z, Jiang C, Liu Y. Smoothed particle hydrodynamics (SPH) simulation of impinging jet flows containing abrasive rigid bodies. *Computational Particle Mechanics*. 2019;6(3):479–501.
13. Dietemann B, Kraft T, Kruggel-Emden H, Bierwisch C. A smoothed particle hydrodynamics scheme for arbitrarily shaped rigid bodies within highly viscous fluids. *Journal of Computational Physics: X*. 2020;8:100068.
14. Kijanski N, Krach D, Steeb H. An SPH Approach for Non-Spherical Particles Immersed in Newtonian Fluids. *Materials*. 2020;13(10):2324.
15. Meier C, Penny RW, Zou Y, Gibbs JS, Hart AJ. Thermophysical phenomena in metal additive manufacturing by selective laser melting: fundamentals, modeling, simulation, and experimentation. *Annual Review of Heat Transfer*. 2017;20.
16. Meier C, Fuchs SL, Much N, Nitzler J, Penny RW, Praegla PM, et al. Physics-based modeling and predictive simulation of powder bed fusion additive manufacturing across length scales. submitted for publication. 2021; [arXiv: 2103.16982](https://arxiv.org/abs/2103.16982).
17. Brandstaeter S, Fuchs SL, Aydin RC, Cyron CJ. Mechanics of the stomach: A review of an emerging field of biomechanics. *GAMM-Mitteilungen*. 2019;42(3):e201900001.

18. Meier C, Fuchs SL, Hart AJ, Wall WA. A novel smoothed particle hydrodynamics formulation for thermo-capillary phase change problems with focus on metal additive manufacturing melt pool modeling. *Computer Methods in Applied Mechanics and Engineering*. 2021;381:113812.
19. Weirather J, Rozov V, Wille M, Schuler P, Seidel C, Adams NA, et al. A smoothed particle hydrodynamics model for laser beam melting of Ni-based alloy 718. *Computers & Mathematics with Applications*. 2019;78(7):2377–94.
20. Fürstenau JP, Wessels H, Weißenfels C, Wriggers P. Generating virtual process maps of SLM using powder-scale SPH simulations. *Computational Particle Mechanics*. 2020;7(4):655–77.
21. Morris JP, Fox PJ, Zhu Y. Modeling low Reynolds number incompressible flows using SPH. *Journal of Computational Physics*. 1997;136(1):214–26.
22. Basa M, Quinlan NJ, Lastiwka M. Robustness and accuracy of SPH formulations for viscous flow. *International Journal for Numerical Methods in Fluids*. 2009;60(10):1127–48.
23. Adami S, Hu XY, Adams NA. A generalized wall boundary condition for smoothed particle hydrodynamics. *Journal of Computational Physics*. 2012;231(21):7057–75.
24. Tong M, Browne DJ. An incompressible multi-phase smoothed particle hydrodynamics (SPH) method for modelling thermocapillary flow. *International Journal of Heat and Mass Transfer*. 2014;73:284–92.
25. Hopp-Hirschler M, Shadloo MS, Nieken U. A smoothed particle hydrodynamics approach for thermo-capillary flows. *Computers & Fluids*. 2018;176:1–19.
26. Russell M, Souto-Iglesias A, Zohdi T. Numerical simulation of Laser Fusion Additive Manufacturing processes using the SPH method. *Computer Methods in Applied Mechanics and Engineering*. 2018;341:163–87.
27. Wessels H, Weißenfels C, Wriggers P. Metal particle fusion analysis for additive manufacturing using the stabilized optimal transportation meshfree method. *Computer Methods in Applied Mechanics and Engineering*. 2018;339:91–114.
28. Trautmann M, Hertel M, Füssel U. Numerical simulation of weld pool dynamics using a SPH approach. *Welding in the World*. 2018;62(5):1013–20.
29. Meier C, Weissbach R, Weinberg J, Wall WA, Hart AJ. Modeling and characterization of cohesion in fine metal powders with a focus on additive manufacturing process simulations. *Powder Technology*. 2019;343:855–66.
30. Meier C, Popp A, Wall WA. Geometrically exact finite element formulations for slender beams: Kirchhoff-Love theory versus Simo-Reissner theory. *Archives of Computational Methods in Engineering*. 2019;26(1):163–243.
31. Cardona A, Geradin M. A beam finite element non-linear theory with finite rotations. *International Journal for Numerical Methods in Engineering*. 1988;26(11):2403–38.
32. Simo JC, Vu-Quoc L. A three-dimensional finite-strain rod model. Part II: Computational aspects. *Computer Methods in Applied Mechanics and Engineering*. 1986;58(1):79–116.
33. Bruls O, Cardona A. On the use of Lie group time integrators in multibody dynamics. *Journal of Computational and Nonlinear Dynamics*. 2010;5(3).
34. Romero I. Formulation and performance of variational integrators for rotating bodies. *Computational Mechanics*. 2008;42(6):825–36.
35. Proell SD, Wall WA, Meier C. On phase change and latent heat models in metal additive manufacturing process simulation. *Advanced Modeling and Simulation in Engineering Sciences*. 2020;7:1–32.
36. Monaghan JJ. Smoothed particle hydrodynamics. *Reports on Progress in Physics*. 2005;68(8):1703.
37. Monaghan JJ, Huppert HE, Worster MG. Solidification using smoothed particle hydrodynamics. *Journal of Computational Physics*. 2005;206(2):684–705.
38. BACI: A Comprehensive Multi-Physics Simulation Framework; accessed February 25, 2021. Available from: <https://baci.pages.gitlab.lrz.de/website>.
39. Liu M, Liu G. Smoothed particle hydrodynamics (SPH): an overview and recent developments. *Archives of Computational Methods in Engineering*. 2010;17(1):25–76.
40. Quinlan NJ, Basa M, Lastiwka M. Truncation error in mesh-free particle methods. *International Journal for Numerical Methods in Engineering*. 2006;66(13):2064–85.
41. Clark TW, Von Hanxleden R, McCammon JA, Scott LR. Parallelizing molecular dynamics using spatial decomposition. In: *Proceedings of IEEE Scalable High Performance Computing Conference*. IEEE; 1994. p. 95–102.
42. Plimpton S. Fast parallel algorithms for short-range molecular dynamics. *Journal of Computational Physics*. 1995;117(1):1–19.
43. Verlet L. Computer “experiments” on classical fluids. I. Thermodynamical properties of Lennard-Jones molecules. *Physical Review*. 1967;159(1):98–103.
44. Allen MP, Tildesley DJ. *Computer Simulation of Liquids*. : Oxford University Press; 2017.
45. Oger G, Le Touzé D, Guibert D, De Lefle M, Biddiscombe J, Soumagne J, et al. On distributed memory MPI-based parallelization of SPH codes in massive HPC context. *Computer Physics Communications*. 2016;200:1–14.
46. Domínguez J, Crespo A, Gómez-Gesteira M, Marongiu J. Neighbour lists in smoothed particle hydrodynamics. *International Journal for Numerical Methods in Fluids*. 2011;67(12):2026–42.
47. Furuichi M, Nishiura D. Iterative load-balancing method with multigrid level relaxation for particle simulation with short-range interactions. *Computer Physics Communications*. 2017;219:135–48.
48. Price DJ. Smoothed particle hydrodynamics and magnetohydrodynamics. *Journal of Computational Physics*. 2012;231(3):759–94.
49. Fuchs SL, Meier C, Wall WA, Cyron CJ. A novel smoothed particle hydrodynamics and finite element coupling scheme for fluid-structure interaction: the sliding boundary particle approach. *Comput Methods Appl Mech Eng*. 2021;383:113922.
50. Adami S, Hu XY, Adams NA. A transport-velocity formulation for smoothed particle hydrodynamics. *Journal of Computational Physics*. 2013;241:292–307.
51. Grill MJ, Wall WA, Meier C. A computational model for molecular interactions between curved slender fibers undergoing large 3D deformations with a focus on electrostatic, van der Waals, and repulsive steric forces. *International Journal for Numerical Methods in Engineering*. 2020;121(10):2285–330.

52. Junior RAA, Cheng LY, Osello PHS. An improvement of rigid bodies contact for particle-based non-smooth walls modeling. *Computational Particle Mechanics*. 2019;6(4):561–80.
53. Zhan L, Peng C, Zhang B, Wu W. A SPH framework for dynamic interaction between soil and rigid body system with hybrid contact method. *International Journal for Numerical and Analytical Methods in Geomechanics*. 2020;44(10):1446–71.
54. Tang X, Paluszny A, Zimmerman RW. An impulse-based energy tracking method for collision resolution. *Computer Methods in Applied Mechanics and Engineering*. 2014;278:160–85.
55. Li Y, Asai M, Chandra B, Isshiki M. Energy-tracking impulse method for particle-discretized rigid-body simulations with frictional contact. *Computational Particle Mechanics*. 2020;p. 1–22.
56. Asai M, Li Y, Chandra B, Takase S. Fluid-rigid-body interaction simulations and validations using a coupled stabilized ISPH-DEM incorporated with the energy-tracking impulse method for multiple-body contacts. *Computer Methods in Applied Mechanics and Engineering*. 2021;377:113681.
57. Cleary PW, Monaghan JJ. Conduction modelling using smoothed particle hydrodynamics. *Journal of Computational Physics*. 1999;148(1):227–64.
58. O'Sullivan C, Bray JD. Selecting a suitable time step for discrete element simulations that use the central difference time integration scheme. *Engineering Computations*. 2004;21(2–4):278–303.
59. Cleary PW. Modelling confined multi-material heat and mass flows using SPH. *Applied Mathematical Modelling*. 1998;22(12):981–93.
60. Feng ZG, Michaelides EE. Interparticle forces and lift on a particle attached to a solid boundary in suspension flow. *Physics of Fluids*. 2002;14(1):49–60.
61. Feng J, Hu HH, Joseph DD. Direct Simulation of Initial Value Problems for the Motion of Solid Bodies in a Newtonian Fluid. Part 2. Couette and Poiseuille Flows. *Journal of Fluid Mechanics*. 1994;277:271–301.
62. Yan Y, Morris JF, Koplik J. Hydrodynamic interaction of two particles in confined linear shear flow at finite Reynolds number. *Physics of Fluids*. 2007;19(11):113305.
63. Meier C, Weissbach R, Weinberg J, Wall WA, Hart AJ. Critical influences of particle size and adhesion on the powder layer uniformity in metal additive manufacturing. *Journal of Materials Processing Technology*. 2019;266:484–501.
64. Brandstaeter S, Gizzi A, Fuchs SL, Gebauer AM, Aydin RC, Cyron CJ. Computational model of gastric motility with active-strain electromechanics. *ZAMM-Journal of Applied Mathematics and Mechanics/Zeitschrift für Angewandte Mathematik und Mechanik*. 2018;98(12):2177–97.
65. Ferrua MJ, Kong F, Singh RP. Computational modeling of gastric digestion and the role of food material properties. *Trends in Food Science & Technology*. 2011;22(9):480–91.
66. Pal A, Indireskumar K, Schwizer W, Abrahamsson B, Fried M, Brasseur JG. Gastric flow and mixing studied using computer simulation. *Proceedings of the Royal Society of London Series B: Biological Sciences*. 2004;271(1557):2587–94.
67. Kong F, Singh R. Disintegration of solid foods in human stomach. *Journal of Food Science*. 2008;73(5):R67–80.
68. Ferrua MJ, Xue Z, Singh RP. On the kinematics and efficiency of advective mixing during gastric digestion—A numerical analysis. *Journal of Biomechanics*. 2014;47(15):3664–73.
69. Yang E, Bui HH, De Sterck H, Nguyen GD, Bouazza A. A scalable parallel computing SPH framework for predictions of geophysical granular flows. *Computers and Geotechnics*. 2020;121:103474.

Publisher's Note

Springer Nature remains neutral with regard to jurisdictional claims in published maps and institutional affiliations.

Submit your manuscript to a SpringerOpen[®] journal and benefit from:

- Convenient online submission
- Rigorous peer review
- Open access: articles freely available online
- High visibility within the field
- Retaining the copyright to your article

Submit your next manuscript at ► [springeropen.com](https://www.springeropen.com)

